Spring 4-23-2014

Design and Implementation of Position-Encoded Microfluidic Microsphere-Trap Arrays

Xiaoxiao Xu
Washington University in St. Louis

Washington University in St. Louis

School of Engineering and Applied Science

Department of Electrical & Systems Engineering

Dissertation Examination Committee:
Arye Nehorai, Chair
Samuel Achilefu
R. Martin Arthur
D. Joseph Dougherty
I. Norman Katz
Zhenyu Li
Heinz Schaettler

Design and Implementation of Position-Encoded Microfluidic Microsphere-Trap Arrays

by

Xiaoxiao Xu

A dissertation presented to the Graduate School of Arts and Sciences
of Washington University in partial fulfillment of the
requirements for the degree of

Doctor of Philosophy

May 2014
Saint Louis, Missouri

Contents

List of Figures

List of Tables

Acknowledgments

First and foremost, I am sincerely grateful to my advisor, Dr. Arye Nehorai, for his wonderful guidance and continuous support in both my doctoral research and life. He has always provided me with a stimulating environment and great freedom to pursue research topics. I also thank him for introducing me to the interesting multidisciplinary project; working with him has been very instructive and enjoyable.

I would like to acknowledge my dissertation committee members, Dr. R. Martin Arthur, Dr. Heinz Schaettler, Dr. I. Norman Katz, Dr. Samuel Achilefu, Dr. D. Joseph Dougherty, and Dr. Zhenyu Li, for their constructive suggestions and valuable inputs along the course of research.

I am truly thankful to all my teachers and professors so far, including Dr. A. Joseph O'Sullivan, Dr. Jr-Shin Li, Dr. Paul Min, Dr. Weixiong Zhang, and Dr. Michael Brent, for helping me build a strong background for my research.

I also want to acknowledge the collaborators on my thesis project, Dr. Pinaki Sarder and Dr. Nalini Kotagiri, whom I enjoy talking with from time to time. Presenting research progress and collecting feedback has proven to be very helpful. Sincere thanks are also due to Dr. Gang Shi on the meta-analysis project, Dr. Viktor Gruev, Shengkui Gao, and Meenal Kulkarni on the polarization image sensor project, and Alan Wells, David O'Brien, and Nathan Kopp on the computational biology project. Working with these great colleagues made our collaboration productive and pleasant.

The research laboratory of Dr. Nehorai has always been a home to me, where I received countless help and support. I would like to convey my heartiest thanks to all my labmates, Gongguo, Tao, Patricio, Satya, Murat, Vanessa, Sandeep, Phani, Weifeng, Peng, Elad, Zhao, Keyong, Jichuan, Mengxue, and Alex, for their friendship and thoughtful discussions.

A special thank goes to Mr. James Ballard at the Engineering Communication Center, who spent hours patiently polishing my papers and dissertation. Special thanks also go to Ms. Sandra Devereaux, Ms. Shauna Dollison, Ms. Elaine Murray, and Ms. Theresa at the department office, who helped me prepare various documents along the Ph.D. program. I

also thank for Mr. Tim McHugh, Mr. Allen Rueter, and Mr. Robert Altman; they have been always patient and helpful when I run into any problems in using the computation facilities.

My long-distance and deepest gratitude to my parents, Suxun Xu and Shaohong Geng, for their endless care and love. Lastly, I thank my husband, Dr. Zimeng Wang, for his support, encouragement, and persistent confidence in me through these years.

Xiaoxiao Xu

Washington University in Saint Louis
May 2014

to my parents

ABSTRACT OF THE DISSERTATION

Design and Implementation of Position-Encoded Microfluidic Microsphere-Trap Arrays

by

Xiaoxiao Xu

Doctor of Philosophy in Electrical Engineering

Washington University in St. Louis, May 2014

Professor Arye Nehorai, Chair

Microarray devices are useful for detecting and analyzing biological targets, such as DNAs, mRNAs, proteins, etc. Applications of microarrays range from fundamental research to clinical diagnostics and drug discovery. In this dissertation, we consider a microsphere array device with predetermined positions of the microspheres. The microspheres are conjugate on their surfaces with molecular probes to capture the targets, and the targets are identified by the microspheres' positions. We implement the microsphere arrays by employing microfluidic technology and a hydrodynamic trapping mechanism. We call our device microfluidic microsphere-trap arrays. To fully realize the potential of the device in biomedical applications, we utilize statistical performance analysis, mathematical optimization, and finite element fluid dynamics simulations to optimize device design, fabrication, and implementation. Our device is promising as a cost-effective and point-of-care lab-on-a-chip system.

We first analyze the statistical performance of position-encoded microsphere arrays in imaging biological targets at different signal-to-noise ratio (SNR) levels. We compute the Ziv-Zakai bound (ZZB) on the errors in estimating the unknown parameters, including the

target concentrations. Through numerical examples, we find the SNR level below which the ZZB provides a more accurate prediction of the error than the posterior Cramér-Rao bound (PCRB) does. We further apply the ZZB to select the optimal design parameters, such as the distance between the microspheres, and to investigate the effects of the experimental variables such as the microscope point-spread function.

We implement the arrays by using microfluidic technology and hydrodynamic trapping. We design a novel geometric structure for the device, and develop a comprehensive and robust framework to optimize its geometric parameters that maximize the microsphere arrays' packing density. We also simultaneously optimize multiple criteria, such as high microsphere trapping efficiency and low fluidic and imaging errors. Microsphere-trapping experiments performed using the optimized device and an un-optimized device demonstrate easy control of the microspheres' transportation and manipulation in the optimized device. They also show that the optimized device greatly outperforms the un-optimized one.

We extend our optimization framework to build a device that enables simultaneous, efficient, and accurate screening of multiple targets in a single microfluidic channel, by immobilizing different-sized microspheres at different regions. Different biomolecules captured on the surfaces of the different-sized microspheres can thus be detected simultaneously by the microspheres' positions.

We employ finite element fluid dynamics simulations to investigate hydrodynamic trapping of microspheres, and to study the effects of the geometric parameters and critical fluid velocity. The accuracy of the time-dependent simulations is validated by experimental results. The simulations guide the device design and experimental operation. The guidelines on the simulation set-up and the openly available model will help researchers apply the simulation to similar microfluidic systems that may accommodate a variety of structured particles.

Chapter 1

Introduction

With the heightened interest in developing lab-on-a-chip biomedical systems [1], [2], [3], there has been a growing need to bridge multiple disciplines in implementing such technologies. Microarray devices can detect and quantify different biological targets, such as DNAs, mRNAs, and proteins [4]. Their applications range from fundamental biological research (e.g., gene expression profiling and genotyping [5]) to rapid infectious disease detection, cancer diagnosis and prognosis [6], [7], and drug discovery [8]. Not surprisingly, microarrays have recently been proven to be a great platform for building lab-on-a-chip systems [9].

Conventional microarrays are two dimensional (2D). They employ spots of specific shapes on a solid substrate (usually a glass slide or silicon thin-film cell) and conjugate the spots' surfaces with molecular probes to capture targets of interest. Recently, a three dimensional (3D) microsphere array technology has been developed [10], [11]. Compared with 2D microarrays, the main advantages of 3D microsphere arrays are the directional binding capability of the microspheres, higher sensitivity, and higher surface-to-volume ratio for faster reaction.

Figure 1.1 provides a schematic diagram of target detection and quantification mechanism in 3D microsphere arrays [12], [13]. Here, the polystyrene microspheres (3~50 μm in diameter) are conjugated on their surfaces with molecular probes to capture targets. The targets are tagged with labels (e.g., quantum dots (QDs), fluorescent dyes, etc.) with conjugated receptors (Fig. 1.1(a)). These labels radiate upon excitation in fluorescence optical imaging, and the radiation is in the form of a spherical shell around each microsphere. The shell fluorescence intensities are considered to be linearly proportional to the target concentrations on the microspheres. To perform optical imaging of the target-captured microspheres, either a epifluorescence microscope (Fig. 1.1(b)) or a confocal microscope (Fig. 1.1(c)) is used. In

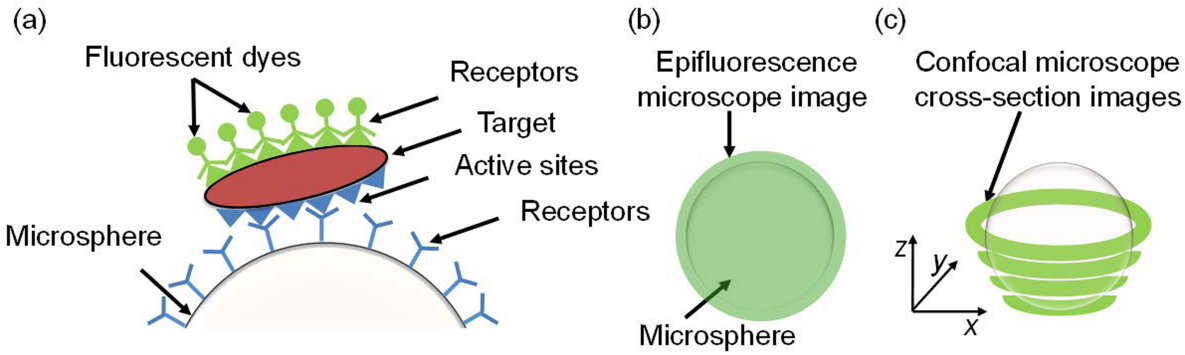

Figure 1.1: Schematic diagram of target detection and quantification mechanism of microsphere arrays. (a) The microspheres are encoded with specific molecular probes to capture one side of the targets of interest. To detect and quantify the targets, labels (e.g., quantum dots (QDs), fluorescent dyes, etc.) with conjugated receptors tag the other side of the targets. These labels radiate upon excitation under fluorescence optical microscopy. (b) Epifluorescence microscope image of a microsphere. (c) Cross-section confocal fluorescence microscope images of a microsphere.

the epifluorescence microscope, all parts of the microspheres are excited at the same time and the radiation is detected by an image sensor, including a large unfocused background. In contrast, the confocal microscope is focused at various depths of the microspheres, parallel to the focal plane (xy plane in Fig. 1.1(c)). It collects a series of 2D cross-section images along the optical axis (z axis) of the fluorescence, called z-stack images. Each cross-section of the shell fluorescence around a microsphere forms a ring [14], [15].

In this chapter, we first describe the motivation of designing position-encoded microsphere arrays and implementing the arrays with microfluidic technology, along with the challenges and limitations of existing microfluidic microsphere array systems. Then, we present our contributions in detail.

1.1 Position-Encoded Microsphere Arrays

In conventional microsphere arrays, the microspheres are placed randomly on a substrate (Fig. 1.2(a)) [11], [16]. The random placement leads to inefficient packing of the microspheres (either widely separated or tightly clustered). It also hampers the imaging quality in the

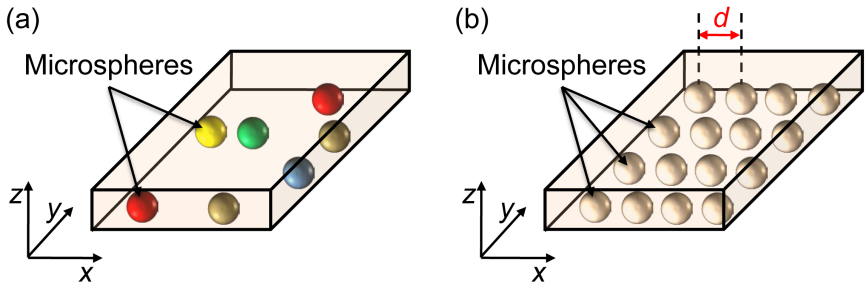

Figure 1.2: Schematic diagram of the 2D grid layout of microsphere arrays. (a) Conventional arrays with random placement of microspheres. (b) Position-encoded microsphere arrays.

microsphere-clustered areas, and necessitates complex image processing [17]. In addition, in these arrays, the microspheres rely on embedded fluorescent dyes or quantum-dot (QD) barcodes to identify the targets on their surfaces. Thus target detection requires complex encoding or post-assay decoding techniques, and the noise in the encoding-decoding process further causes errors in the identification [18].

To address the drawbacks of the conventional arrays, we design a novel device with predetermined positions of the microspheres (Fig. 1.2(b)), a feature we term position-encoding [12], [19]. The predetermined positions help identify the captured targets, without relying on embedded dyes/QDs or complex assay encoding-decoding techniques. The target identification is error-free, and it also simplifies the image analysis; especially significant, it simplifies simultaneous screening of multiple targets. As our first task, we develop a statistical approach to select the minimal distance between the microspheres to ensure efficient packing and a desired error level for target concentration estimation. We also investigate the effects of the experimental variables on the performance of the microsphere arrays.

1.2 Microfluidic Microsphere-Trap Arrays

To fabricate the microarray or microsphere array device, the industrial standard methods are robotic printing [20], photolithography patterned *in-situ* synthesis (such as Affymetrix) [21], and self-assembly of microbeads (such as Illumina) [16], [22]. However, due to the limited size of their printing spots, robotic-printed microarrays suffer from inhomogeneous distribution [20] and inefficient packing. Photolithographic patterned microarrays are costly and

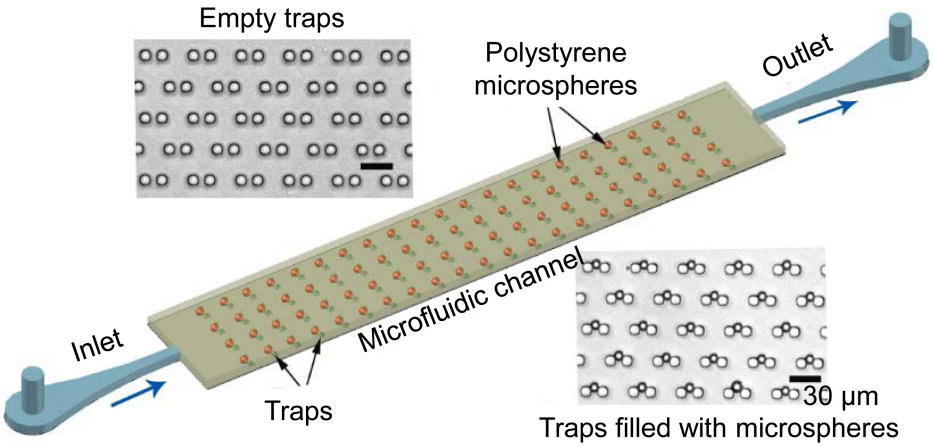

Figure 1.3: Schematic diagram of microfluidic microsphere-trap arrays. The microfluidic channel contains hydrodynamic trap arrays. The channel is connected by an inlet and an outlet. A liquid solution carrying microspheres flows from the inlet and through the channel. The microspheres fill the traps and get immobilized during the loading process.

complicated to implement [21]. Self-assembled microarrays need specially fabricated substrates such as etched fiber optic bundles or silicon wafers, and thus they are also relatively expensive. To eliminate these drawbacks of the existing methods, researchers recently have integrated microfluidic technology with microsphere arrays [23], [24], [25]. Microfluidic technology deals with the behavior, precise control, and manipulation of fluids that are geometrically constrained to a small, typically micrometer, scale. The resulting microfluidics microsphere array systems have many advantages, such as offering a controlled liquid environment, reducing reagent cost and hybridization assay time, and providing the potential for mass production of devices at low cost [23], [26].

We implement our position-encoded microsphere arrays by employing microfluidic technology and a hydrodynamic trapping mechanism, and we call them microfluidic microsphere-trap arrays. Figure 1.3 presents a schematic diagram of the arrays. The microfluidic channel contains periodic rows of hydrodynamic traps, which are made of polydimethylsiloxane (PDMS). The channel is connected by an inlet and an outlet. A liquid, such as phosphate buffered saline (PBS), carries the microspheres through the channel, where the traps immobilize the microspheres during the process. In one scenario, the microspheres have already captured targets in solution before the loading operation. In the other scenario, we can perform on-chip reaction by passing a microfluid stream containing targets through the channel, where

the targets are captured by the immobilized microspheres. When re-using the device, to avoid cross contamination, before new microspheres are loaded, the residual microspheres are washed out using buffer solution.

As an independent and dedicated platform, the performance of the microfluidic microsphere-trap arrays depends on careful optimization of the device architecture. Several criteria should be taken into account, including maximizing the microspheres' packing density to make the device compact, efficiently immobilizing microspheres, effectively eliminating fluidic errors, minimizing errors introduced during the device's fabrication, and minimizing aberrations induced during the subsequent fluorescence imaging [12]. However, to date (to our knowledge) no studies have been reported on simultaneous optimization of these multiple criteria. Therefore, as our second task, we design for the device a novel trap array geometry, and develop a comprehensive and robust framework to optimize its geometric parameters to satisfy all the criteria mentioned above.

To further optimize the functionalities of the microfluidic system, one needs to understand the hydrodynamic behavior of the microspheres (biological particles in more general applications) so as to manipulate them in a controlled manner. In [27], Karimi *et al.* briefly reviewed the hydrodynamic mechanisms of cell and particle trapping. However, microfluidic devices are not simply scaled-down versions of conventional macro-scale systems. Because the dimensions of a microfluidic structure are small, particles suspended in a fluid become comparable in size to the structure itself, which dramatically alters the device's behaviors. As a result, the fluid dynamics are rather complicated and are affected by many parameters, e.g., the fluid's viscosity, velocity, and pressure; the device geometry; the particle number, shape, and elastic flexibility (specially for blood cells or emulsions); and fluid-particle interactions.

To study a microfluidic system, computational fluid dynamic (CFD) simulations coupled with solid mechanics have become an increasingly important tool. By incorporating the complexities of the system's parameters, the microfluidic system's hydrodynamic behavior can be predicted and visualized, even though the system's minute dimensions make that behavior difficult (but not impossible) to prove via explicit mathematical methods or experiments. Therefore, the simulations help researchers assess design alternatives at reduced

cost and guide experimental operation [28], [29]. For our device, the importance of hydrodynamic properties in the successful trapping of the microspheres highlights the value of CFD simulations in predicting and investigating the movement of microspheres. However, to our knowledge, there are no easily accessible simulation models for similar microfluidic systems, which are customizable and ready-to-use for device fabricators and users. Thus as our third task, we create a finite element (FEM) simulation model to study the hydrodynamic behaviors of the microspheres in our device.

Using microspheres functionalized with different probes, microsphere arrays have great potential for quantitative and simultaneous assay of multiple types of targets in small volumes of material, and collection of statistically rigorous data from numerous microspheres for each target type. In our position-encoded microsphere arrays, simultaneous detection of multiple targets can be achieved according to the precise positioning of the microspheres. To direct the microspheres to their predetermined positions, one possibility is to implement multiple channels connected with individual chambers on a microfluidic chip, and use on-chip valves to open or lock the channels to direct the microspheres for a specific type of targets to flow into a specific chamber [30], [31], [32], [33], [34], [35]. While this approach can achieve multiplexing, a disadvantage is that the valves occupy considerable space on the chip and they need sophisticated external control and actuation [36]. Moreover, for effective collection of information, such as profiling multiple proteins or simultaneous mRNA and protein profiling, and for precise control of flow condition and local environment, there is a need for multi-analyte detection in a single microfluidic channel. Therefore, as our fourth task, we aim to develop a simple and easy-to-control one-channel platform for simultaneous and efficient detection and quantification of multiple targets.

1.3 Our Contributions

In this dissertation, after addressing the challenges and limitations in existing microfluidic microsphere array systems, we design and implement our novel position-encoded microfluidic microsphere-trap arrays. Below, we briefly summarize our contributions.

Statistical Design and Performance Analysis using the Ziv-Zakai Bound: We provide a statistical design for the position-encoded microsphere arrays and analyze their

statistical performance in imaging targets at different signal-to-noise ratio (SNR) levels, especially at low SNR. We compute the Ziv-Zakai bound (ZZB) on the errors in estimating the unknown parameters, including the target concentrations. Through numerical examples, we find the SNR level below which the ZZB provides a more accurate estimation of the error than the posterior Cramér-Rao bound (PCRB) does. We further apply the ZZB to select the optimal design parameters of the device, such as the distance between the microspheres, and to investigate the effects of the experimental variables, such as the microscope point-spread function. An imaging experiment on microspheres with protein targets verifies the optimal design parameters using the ZZB.

Optimization of Microfluidic Microsphere-Trap Arrays: We implement the position-encoded microsphere arrays by employing microfluidic technology and a hydrodynamic trapping mechanism. We design a novel geometric structure of the device, and develop a comprehensive and robust framework to optimize the values of its geometric parameters to maximize the microsphere arrays' packing density. We also simultaneously optimize multiple criteria, such as efficiently immobilizing a single microsphere in each trap, effectively eliminating fluidic errors such as channel clogging and multiple microspheres in a trap, minimizing errors in subsequent imaging experiments, and easily recovering targets. We use finite element fluid dynamics simulations to validate the trapping mechanism and to study the effects of the optimization geometric parameters on the packing density. We further perform microsphere-trapping experiments using the optimized device and a device with randomly selected geometric parameters, which we denote as the un-optimized device. These experiments demonstrate easy control of the microspheres' transportation and manipulation in the optimized device. They also show that the optimized device greatly outperforms the un-optimized device by increasing the packing density by a factor of two, improving the microsphere trapping efficiency from 58% to 99%, and reducing fluidic errors from 48% to a negligible level (less than 1%).

Finite Element Simulations of Hydrodynamic Trapping: We investigate hydrodynamic trapping of microspheres in our device by using finite element simulations. The accuracy of the time-dependent simulation of a microsphere's motion towards the traps is validated by our experimental results. Based on the simulations, we study the fluid velocity field, pressure field, and force and stress on the microsphere in the device. We further

explore the trap array's geometric parameters and critical fluid velocity, which affect the microsphere's hydrodynamic trapping. The information is valuable for designing microfluidic devices and guiding experimental operation. Additionally, we provide guidelines on the simulation set-up, and we release an openly available implementation of our simulation in one of the popular FEM softwares, COMSOL Multiphysics. Researchers may tailor the model to simulate similar microfluidic systems to accommodate a variety of structured particles. Therefore, the simulation will be of particular interest to biomedical research involving cell or bead transport and migration, blood flow within microvessels, and drug delivery.

Simultaneous Detection of Multiple Biological Targets: We extend our analytical optimization framework to build a microfluidic microsphere-trap array device that enables simultaneous, efficient, and accurate screening of multiple biological targets in a single microfluidic channel. The traps in the channel of the device can immobilize different-sized microspheres at different regions, obeying hydrodynamically engineered trapping mechanisms. Different biomolecules can be captured by the receptors on the surfaces of microspheres of different sizes. They are thus detected according to the microspheres' positions, simplifying screening and avoiding target identification errors. To demonstrate the proposition, we build a device for simultaneous detection of two target types, by trapping microspheres of two sizes. We evaluate the device's performance using finite element fluid dynamics simulations and microsphere-trapping experiments. These results validate that the device efficiently achieves position-encoding of the two-sized microspheres with few fluidic errors, providing the promise of utilizing our framework to build devices for simultaneous detection of more targets. We also envision utilizing the device to separate, sort, or enumerate cells, such as circulating tumor cells and blood cells, based on cell size and deformability. Therefore, the device is promising as a cost-effective and point-of-care miniaturized disease diagnostic tool.

1.4 Outline of the Dissertation

The rest of the dissertation is organized as follows. In **Chapter 2**, we provide the statistical design and performance analysis of the position-encoded microsphere arrays. In **Chapter 3**, we develop the optimization framework for the microfluidic microsphere-trap arrays. In **Chapter 4**, we build the finite element fluid dynamics simulation model for the arrays. In

Chapter 5, we design the arrays for simultaneous detection for multiple biological targets. **Chapter 6** summarizes the conclusions reached in this dissertation and points out potential future work.

Chapter 2

Statistical Design and Performance Analysis of Position-Encoded Microsphere Arrays Using the Ziv-Zakai Bound[1]

In this chapter, we provide the statistical design of the position-encoded microsphere arrays, and use the Ziv-Zakai bound to investigate their performance.

2.1 Introduction

Microsphere arrays effectively capture biological targets, such as DNAs, mRNAs, and proteins, on the surfaces of the microspheres. These arrays are used to detect and identify targets and analyze their concentrations [10], [11]. Applications of microsphere arrays range from fundamental biological research (e.g., gene expression profiling and genotyping [5]) to clinical diagnostics [7], and drug discovery [8]. In conventional microsphere arrays, the microspheres are placed randomly on a substrate [11]. The random placement leads to inefficient packing (either widely separated or tightly clustered), and also necessitates complex image processing [17]. In addition, in these arrays, the microspheres rely on embedded fluorescent

[1]Based on X. Xu, P. Sarder, N. Kotagiri, S. Achilefu, and A. Nehorai, "Performance analysis and design of position-encoded microsphere arrays using the Ziv-Zakai bound", *IEEE Trans. NanoBioscience*, vol. 12, pp. 29-40, Mar. 2013.

dyes or quantum-dot (QD) barcodes to identify the targets on their surfaces, thus the noise in the measured light spectra of the dyes or QDs causes errors in the identification [18].

In our previous work [12], we addressed the drawbacks of the conventional microsphere arrays by proposing a novel microsphere array device with predetermined positions of the microspheres, a feature we term position-encoding. The predetermined positions help identify the captured targets, without relying on embedded dyes or QDs in the microspheres. The target identification method is error-free, and it also simplifies the image analysis. Furthermore, by coding microspheres with different receptors, the microsphere arrays can simultaneously capture, identify, and quantify multiple types of targets [11]. For the design of the proposed device [12], we employed the posterior Cramér-Rao bound (PCRB) [37] on the mean-square error (MSE) of the target concentration estimation and also used the PCRB to choose the optimal design parameters. It enabled us to select the minimal distance d_{opt} between the microspheres to increase packing efficiency, and to select the optimal imaging temperature T_{opt} to reduce cost, for a desired estimation error level.

However, several critical issues were not considered in our previous work. First and most important, in most biological experiments, the measurements of the targets are at low signal-to-noise ratios (SNR) [38], but the PCRB is not tight to the true MSE in low SNR situations [39]. Therefore, the PCRB might not precisely characterize the performance for an accurate design of the device with biomedical applications. For example, the PCRB is much smaller than the true MSE, and the d_{opt} chosen from the PCRB might be too small and would induce a large error in estimation. Second, the measurements of the targets were all relative values, and thus the value of the computed MSE bound was non-specific in physical terms. Third, important experimental variables (see below) influencing the device's performance and imaging were not studied. Finally, no image experiments were performed to verify our design.

In this chapter, we aim to overcome the limitations of the analyses in [12] and extend our investigations to consider some new aspects:

1) We propose to use the Ziv-Zakai bound (ZZB) [40] as the MSE bound for the statistical design of the position-encoded microsphere arrays. The ZZB is tight to the global MSE at all SNR levels [39], and so should accurately evaluate the device's performance and provide

the levels of d_{opt} and T_{opt} in all SNR situations. We also investigate the level of the SNR below which the use of the ZZB instead of the PCRB is highly demanded.

2) We denote the estimation error-to-signal ratio (ESR): $\sqrt{\text{MSE bound}}/\text{signal}$ as our performance measure. This measure will enable an explicit evaluation of our device's performance in physical terms.

3) We provide a detailed discussion of the effects of the experimental variables on the device performance, the SNR, the microscope point-spread function (PSF), and target concentrations.

4) We perform an imaging experiment to verify our statistical design and optimal parameter selection.

This chapter is organized as follows. Section 2.2 briefly reviews the configuration of the position-encoded microsphere arrays. In Section 2.3, we present the statistical model, derive the ZZB and the performance measure ESR, and propose the design parameters and experimental variables. Section 2.4 provides a numerical example which compares the ZZB with the PCRB at different SNRs, demonstrates the selection of the optimal design parameters, and discusses the effects of the experimental variables. Section 2.5 presents the imaging experiment, and Section 2.6 summarizes the chapter.

2.2 Position-Encoded Microsphere Arrays

In this section, we briefly review the general configuration of the position-encoded microsphere arrays and the image acquisition process. Figure 2.1(a) shows a uniform two dimensional (2D) grid layout for the microsphere arrays. The polystyrene microspheres (3~50 μm in diameter) are placed in predetermined positions at a distance d from each other. These microspheres are encoded by dedicated receptors to capture specific targets of interest (Fig. 2.1(b)). For example, in the imaging experiment presented in Section 2.5, the receptors are anti-IgG antibodies for target protein IgG. To detect and quantify the targets, fluorescent dyes conjugated with receptors are used, instead of nanospheres encoded with QDs as proposed in [12].

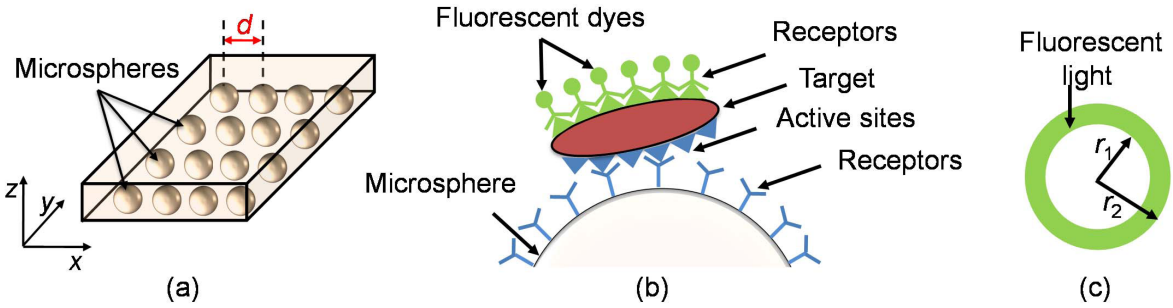

Figure 2.1: Schematic diagram of the position-encoded microsphere arrays. (a) 2D layout. (b) A target captured on a microsphere. (c) Ideal cross-section image of the shell fluorescence.

To perform the detection, we pass a microfluid stream containing targets through the microsphere arrays and periodically release a cocktail of receptors with fluorescent dyes. In this flow process, the targets are captured by the dedicated microspheres on one side and tagged by the dyes on the other side (Fig. 2.1(b)). Then, upon excitation all dyes emit fluorescence in the form of a spherical shell around each microsphere.

To image the target-captured specimen, we focus a confocal fluorescence microscope at various depths of the arrays, parallel to the focal plane (xy plane) of the device in Fig. 2.1(a). We then use a CCD/CMOS image sensor to collect a series of 2D cross-section images along the optical axis (z axis) of the emitted fluorescence. These images are called z-stack images. Thus, each cross-section of the shell fluorescence around a microsphere forms a ring (Fig. 2.1(c)) [14], [15]. The shell fluorescence intensities are considered to be linearly proportional to the target concentrations on the microspheres.

2.3 Methods

In this section, we first present the statistical measurement model of the position-encoded microsphere arrays. We use the same object model as in [12], and employ a simplified microscope PSF model that greatly reduces the analytical complexity and adequately preserves the PSF properties, as well as using a more accurate noise model that incorporates important noise terms. Then we derive the ZZB on the corresponding MSE of the target concentration

estimation, and obtain the ESR. Finally, we propose the design parameters and experimental variables to be discussed.

2.3.1 Measurement Model

The measurement of an illuminating object in fluorescence microscopy imaging is expressed by

$$g(x, y, z; \boldsymbol{\theta}) = s(x, y, z; \boldsymbol{\theta}) \otimes h(x, y, z) + w(x, y, z; \boldsymbol{\theta}), \tag{2.1}$$

where $\boldsymbol{\theta}$ represents the unknown parameters to be estimated. $x \in \{x_1, x_2, \ldots, x_K\}$, $y \in \{y_1, y_2, \ldots, y_L\}$ and $z \in \{z_1, z_2, \ldots, z_M\}$ denote the measurement positions; and K, L, and M are the numbers of measurements along the x, y, and z axes. $s(x, y, z; \boldsymbol{\theta})$ is the illuminating object, $h(x, y, z)$ is the microscope PSF [41] that distorts the object, $\otimes$ is the convolution operation, and $w(x, y, z; \boldsymbol{\theta})$ is the noise. The $s(x, y, z; \boldsymbol{\theta})$ (object model), $h(x, y, z)$ (PSF model), and $w(x, y, z; \boldsymbol{\theta})$ (noise model) are as follows.

1) *Object Model* $s(x, y, z; \boldsymbol{\theta})$: The emitted light around each microsphere is a spherical shell. We consider the illuminating object model $s(x, y, z; \boldsymbol{\theta})$ as the sum of shell lights from two neighboring microspheres separated at a distance d:

$$s(x, y, z; \boldsymbol{\theta}) = s_{\text{sh}}(x, y, z; \theta_1) + s_{\text{sh}}(x - d, y, z; \theta_2), \tag{2.2}$$

where $\boldsymbol{\theta} = [\theta_1, \theta_2]^T$, with θ_1 and θ_2 as the unknown intensities of the shells around microspheres 1 and 2, respectively. We assume that the intensity of a single shell is constant, and express the shell with inner radius r_1 and outer radius r_2 as

$$s_{\text{sh}}(x, y, z; \theta_m) = \begin{cases} \theta_m & \text{if } r_1 < \sqrt{x^2 + y^2 + z^2} < r_2, \\ 0 & \text{otherwise,} \end{cases} \tag{2.3}$$

where $m \in 1, 2$ indexes the two neighboring microspheres, and θ_1 and θ_2 are independent. In general, no additional information other than the maximum intensity levels $\theta_{\max}$ is available, so we adopt a uniform prior distribution for θ_m, i.e., $\theta_m \sim \mathcal{U}(0, \theta_{\max})$. Moreover, r_1 is the sum of the microsphere radius and its adjacent receptor's size. The shell contains the target,

the receptor on the target, and fluorescent dye. r_2, the outer shell radius, equals r_1 plus the shell size.

We suppose the unknown shell intensity to be linearly proportional to the target concentration, and we compute the MSE bound for the estimation of $\boldsymbol{\theta}$ in the statistical analysis.

2) *PSF Model* $h(x, y, z)$: Our previous work [12] employed Gibson and Lanni's classic diffraction-limited PSF model [41] to represent the microscope PSF of the image system, which has been proven to have a high consistency with experimental evaluations. However, that PSF model was very complex. For simplicity, here we use a 3D Gaussian PSF model instead of Gibson and Lanni's model [42], [43]:

$$h(x, y, z) = \exp\left(-\frac{x^2 + y^2}{2\sigma_1^2} - \frac{z^2}{2\sigma_2^2}\right), \tag{2.4}$$

where σ_1^2 and σ_2^2 determine the PSF function. This Gaussian model is simpler and more analytical tractable than Gibson and Lanni's model. Moreover, it has been shown to be an adequate PSF model, as it preserves the PSF's symmetry along the focal planes and asymmetry along the optical direction [43]. The estimation of σ_1^2 and σ_2^2 in the Gaussian model is described in Appendix A.

3) *Noise Model* $w(x, y, z; \boldsymbol{\theta})$: In [12], we attributed the noise to the photon noise w_{s} in the photon counting process, and the dark noise w_{d} due to dark current. However, we did not consider another dominant noise source, the microscope image sensor's reset and readout thermal noise w_{t} [44], [45]. We update the noise model by adding w_{rt}:

$$w(x, y, z; \boldsymbol{\theta}) = w_{\mathrm{s}}(x, y, z; \boldsymbol{\theta}) + w_{\mathrm{d}}(x, y, z; \boldsymbol{\theta}) + w_{\mathrm{t}}(x, y, z; \boldsymbol{\theta}). \tag{2.5}$$

The photon counting noise $w_{\mathrm{s}}(x, y, z; \boldsymbol{\theta})$ is approximated as an independently and identically distributed (i.i.d) zero-mean Gaussian noise, i.e.,

$$w_{\mathrm{s}}(x, y, z; \boldsymbol{\theta}) \sim \mathcal{N}(0, s(x, y, z; \boldsymbol{\theta}) \otimes h(x, y, z)/\beta), \tag{2.6}$$

with β as the photon-conversion factor of the image sensor [46]. β can be estimated by the standard photon transfer method (variance method), as shown in [12].

The dark noise $w_{\mathrm{d}}(x, y, z; \boldsymbol{\theta})$ and the thermal noise $w_{\mathrm{t}}(x, y, z; \boldsymbol{\theta})$ are regarded as the background noise. They are assumed to be zero-mean i.i.d Gaussian, with noise levels (variances) of σ_{d}^2 and σ_{t}^2, respectively. σ_{d}^2 and σ_{t}^2 are functions of the imaging temperature T [44], [47]:

$$\sigma_{\mathrm{d}}^2(T) = B_1 \exp(-\frac{E_{\mathrm{g}}}{2k_{\mathrm{B}}T}), \quad \sigma_{\mathrm{t}}^2(T) = B_2 k_{\mathrm{B}} T, \tag{2.7}$$

where k_{B} is the Boltzmann constant. The unknown parameters B_1 and B_2 are constants determined by experimental conditions, as well as the specifications of the microscope and the image sensor. B_1 and B_2 can be estimated from experimental data, and the estimation method is described in Appendix B.

The modified noise model here characterizes the effect of T on the noise levels and the device's performance more accurately than that in [12]. It should be noted that other external or intrinsic noises are not taken into account in the noise model, such as scattered excitation and background light, and flicker $(1/f)$ noise. This omission is reasonable because they either can be eliminated by standardized experimental operation, or are negligible in state-of-the-art image sensors [44], [47].

To summarize, we define

$$\tilde{s}(x, y, z; \boldsymbol{\theta}) = s(x, y, z; \boldsymbol{\theta}) \otimes h(x, y, z). \tag{2.8}$$

Combining (2.1)-(2.8), we have the measurement model as

$$g(x, y, z; \boldsymbol{\theta}) = \tilde{s}(x, y, z; \boldsymbol{\theta}) + w_{\mathrm{s}}(x, y, z; \boldsymbol{\theta}) + w_{\mathrm{d}}(x, y, z; \boldsymbol{\theta}) + w_{\mathrm{t}}(x, y, z; \boldsymbol{\theta}), \tag{2.9}$$

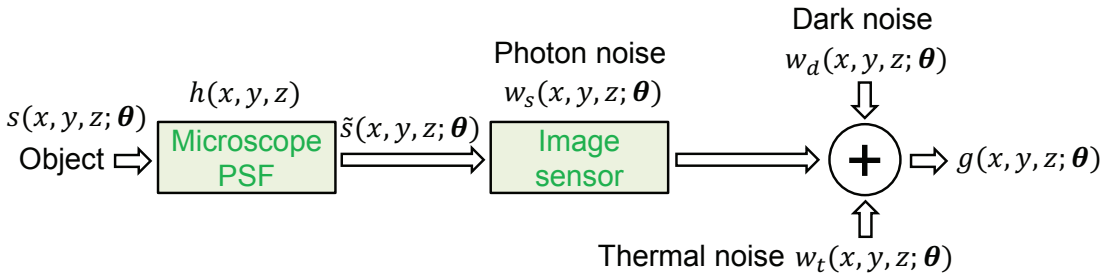

Figure 2.2: Schematic diagram of the measurement model.

and $g(x,y,z;\boldsymbol{\theta}) \sim \mathcal{N}(\tilde{s}(x,y,z;\boldsymbol{\theta}), \tilde{s}(x,y,z;\boldsymbol{\theta})/\beta + \sigma_{\mathrm{d}}^2 + \sigma_{\mathrm{t}}^2)$. The schematic diagram of the measurement model is shown in Fig. 2.2.

For convenience, we lump the measurements into a vector

$$\boldsymbol{g} = \tilde{\boldsymbol{s}} + \boldsymbol{w}_{\mathrm{s}} + \boldsymbol{w}_{\mathrm{d}} + \boldsymbol{w}_{\mathrm{t}}, \tag{2.10}$$

where $\boldsymbol{g}$ is a $(KLM \times 1)$-dimensional vector whose $(KL(m-1)+K(l-1)+k)$th component is $g(x_k, y_l, z_m; \boldsymbol{\theta})$, and similarly for $\tilde{\boldsymbol{s}}$, $\boldsymbol{w}_{\mathrm{s}}$, $\boldsymbol{w}_{\mathrm{d}}$, and $\boldsymbol{w}_{\mathrm{t}}$. Therefore, $\boldsymbol{g} \sim \mathcal{N}(\tilde{\boldsymbol{s}}, \mathrm{diag}(\tilde{\boldsymbol{s}})/\beta + (\sigma_{\mathrm{d}}^2 + \sigma_{\mathrm{t}}^2)\boldsymbol{I})$, where $\mathrm{diag}(\tilde{\boldsymbol{s}})$ is a diagonal matrix with diagonal elements $\tilde{s}(\cdot)$, and $\boldsymbol{I}$ is the identity matrix.

We define the SNR in a single microsphere area as

$$\mathrm{SNR_{dB}} = 10\log_{10}\left(\frac{1}{N}\sum_{z}\sum_{y}\sum_{x}\frac{\tilde{\mathrm{s}}(\mathrm{x},\mathrm{y},\mathrm{z};\boldsymbol{\theta})^2}{\frac{\tilde{\mathrm{s}}(\mathrm{x},\mathrm{y},\mathrm{z};\boldsymbol{\theta})}{\beta} + \sigma_{\mathrm{d}}^2 + \sigma_{\mathrm{t}}^2}\right), \tag{2.11}$$

where x, y, and z represent the area of a microsphere, and N is the number of measurements in this area.

2.3.2 The Ziv-Zakai Bound

Because we expect the ZZB to be tighter than the PCRB to the global MSE performance at all SNR levels, we propose to use the ZZB as the lower bound on the MSE in estimating unknown target concentration in the statistical design. Below, the concept of the ZZB [40] is introduced.

Let $\boldsymbol{g}$ denote the measurement vector, and $\hat{\boldsymbol{\theta}}(\boldsymbol{g})$ denote the estimator of the unknown n-dimensional random vector $\boldsymbol{\theta} = [\theta_1, \theta_2, \ldots, \theta_n]^T$. The estimation error is $\boldsymbol{\epsilon} = \hat{\boldsymbol{\theta}}(\boldsymbol{g}) - \boldsymbol{\theta}$, with error correlation matrix $\boldsymbol{R}_{\boldsymbol{\epsilon}} = \mathrm{E}[\boldsymbol{\epsilon}\boldsymbol{\epsilon}^{\mathrm{T}}]$, where the expectation $\mathrm{E}(\cdot)$ is over $\boldsymbol{g}$ and $\boldsymbol{\theta}$, and $\boldsymbol{\theta}$ has a known prior probability density function (pdf) $p_{\Theta}(\boldsymbol{\theta})$. Then, the ZZB is computed through the following inequality:

$$\boldsymbol{u}^T\boldsymbol{R}_{\boldsymbol{\epsilon}}\boldsymbol{u} \geq \frac{1}{2}\int_0^{\infty}\mathcal{V}\left\{\max_{\boldsymbol{e}:\boldsymbol{u}^T\boldsymbol{e}=b}\left[\int_{\mathbb{R}^n}(p_{\boldsymbol{\theta}}(\boldsymbol{\eta}) + p_{\boldsymbol{\theta}}(\boldsymbol{\eta}+\boldsymbol{e}))P_{\min}(\boldsymbol{\eta}, \boldsymbol{\eta}+\boldsymbol{e})\mathrm{d}\boldsymbol{\eta}\right]\right\}b\mathrm{d}b, \tag{2.12}$$

where $\boldsymbol{u}$ is any n-dimensional vector, $\mathcal{V}$ is a 'valley-filling' function, $\boldsymbol{e}$ is the offset, and $P_{\min}(\boldsymbol{\eta}, \boldsymbol{\eta}+\boldsymbol{e})$ is the minimum probability of error for the hypothesis test:

$$\begin{aligned} \mathcal{H}_0 &: \boldsymbol{\theta} = \boldsymbol{\eta} \qquad \text{with } \boldsymbol{g} \sim p_{\boldsymbol{g}|\boldsymbol{\theta}}(\boldsymbol{g}|\boldsymbol{\eta}) \\ \mathcal{H}_1 &: \boldsymbol{\theta} = \boldsymbol{\eta}+\boldsymbol{e} \qquad \text{with } \boldsymbol{g} \sim p_{\boldsymbol{g}|\boldsymbol{\theta}}(\boldsymbol{g}|\boldsymbol{\eta}+\boldsymbol{e}), \end{aligned} \tag{2.13}$$

with $\Pr(\mathcal{H}_0) = \mathrm{p}_{\boldsymbol{\theta}}(\boldsymbol{\eta})/(\mathrm{p}_{\boldsymbol{\theta}}(\boldsymbol{\eta}) + \mathrm{p}_{\boldsymbol{\theta}}(\boldsymbol{\eta}+\boldsymbol{e})) = 1 - \Pr(\mathcal{H}_1)$.

It is generally challenging to obtain a closed-form expression of the bound (2.12), because it is difficult to analytically derive $P_{\min}(\cdot)$ and $\mathcal{V}(\cdot)$ [40].

2.3.3 The Ziv-Zakai Bound in Our Design

The unknown parameters are $\boldsymbol{\theta} = [\theta_1, \theta_2]^T$, and $\mathrm{ZZB}(\boldsymbol{\theta}) = \mathrm{ZZB}(\theta_1) + \mathrm{ZZB}(\theta_2)$. $\mathrm{ZZB}(\theta_1)$ can be computed by bounding the matrix form $\boldsymbol{u}^T\boldsymbol{R}_{\boldsymbol{\epsilon}}\boldsymbol{u}$ in (2.12) for all the parameters $\boldsymbol{\theta}$ jointly, and letting $\boldsymbol{u} = [1, 0]^T$. $\mathrm{ZZB}(\theta_2)$ can be computed in a similar way by letting $\boldsymbol{u} = [0, 1]^T$ [40]. The offset is $\boldsymbol{e} = [e_1, e_2]^T$, with $e_1, e_2 \in [-\theta_{\max}\ \theta_{\max}]$.

Recall that the prior distribution for $\boldsymbol{\theta}$ is uniform, so the valley-filling function $\mathcal{V}(\cdot)$ is trivial in (2.12) [40]. Moreover, the prior probabilities of the hypothesis can be equated ($\Pr(\mathcal{H}_0) = \Pr(\mathcal{H}_1) = \frac{1}{2}$), so that $\frac{1}{2}(p_{\boldsymbol{\theta}}(\boldsymbol{\eta}) + p_{\boldsymbol{\theta}}(\boldsymbol{\eta}+\boldsymbol{e}))$ in (2.12) is replaced by $\min(p_{\boldsymbol{\theta}}(\boldsymbol{\eta}), p_{\boldsymbol{\theta}}(\boldsymbol{\eta}+\boldsymbol{e}))$ [40]. Then, the ZZB becomes

$$\boldsymbol{u}^T\boldsymbol{R}_{\boldsymbol{\epsilon}}\boldsymbol{u} \geq \int_0^{\theta_{\max}} \max_{\boldsymbol{e}:\boldsymbol{u}^T\boldsymbol{e}=b} \left\{ \int_{\mathbb{R}^2} \min(p_{\boldsymbol{\theta}}(\boldsymbol{\eta}), p_{\boldsymbol{\theta}}(\boldsymbol{\eta}+\boldsymbol{e})) P_{\min}(\boldsymbol{\eta}, \boldsymbol{\eta}+\boldsymbol{e}) \mathrm{d}\boldsymbol{\eta} \right\} b \mathrm{d}b, \tag{2.14}$$

$$\text{where } \min(p_{\boldsymbol{\theta}}(\boldsymbol{\eta}), p_{\boldsymbol{\theta}}(\boldsymbol{\eta}+\boldsymbol{e})) = \begin{cases} \frac{1}{\theta_{\max}^2} & \text{if } \boldsymbol{\eta}, \boldsymbol{\eta}+\boldsymbol{e} \in [0, \theta_{\max}] \cup [0, \theta_{\max}], \\ 0 & \text{otherwise,} \end{cases} \tag{2.15}$$

and the minimum probability of error $P_{\min}(\boldsymbol{\eta}, \boldsymbol{\eta}+\boldsymbol{e})$ is obtained from the log-likelihood ratio test [37]

$$P_{\min}(\boldsymbol{\eta}, \boldsymbol{\eta}+\boldsymbol{e}) = \frac{1}{2}\big[\Pr(\Lambda(\boldsymbol{g}, \boldsymbol{\theta}) < 0 | \mathcal{H}_0) + \Pr(\Lambda(\boldsymbol{g}, \boldsymbol{\theta}) > 0 | \mathcal{H}_1)\big], \tag{2.16}$$

with $\Lambda(\boldsymbol{g}, \boldsymbol{\theta}) = \log(\mathrm{p}_{\boldsymbol{g}|\boldsymbol{\theta}}(\boldsymbol{g}|\mathcal{H}_1)/\mathrm{p}_{\boldsymbol{g}|\boldsymbol{\theta}}(\boldsymbol{g}|\mathcal{H}_0))$.

There is no closed-form expression of the ZZB, so we employ a numerical computation to obtain its value. Particularly, we convert the integration over b in (2.14) to Riemann sums over N discrete points $b(i)$, $i = 1, \cdots, N$. At each $b(i)$, we again convert the integration over $\boldsymbol{\eta} = [\eta_1, \eta_2]^T$ to sums over M_1 and M_2 points. Then we generate discrete points of $\boldsymbol{e}$ that satisfy $\boldsymbol{u}^T\boldsymbol{e} = b$. Thus, for each fixed $b(i)$, fixed $\boldsymbol{\eta}$, and fixed $\boldsymbol{e}$, $P_{\min}(\boldsymbol{\eta}, \boldsymbol{\eta}+\boldsymbol{e})$ is computed by the method described in Appendix C. The $\max_{\boldsymbol{e}:\boldsymbol{u}^T\boldsymbol{e}=b}\{\cdot\}$ in (2.14) is subsequently obtained, and the numerical value of the ZZB bound is computed.

2.3.4 Performance Measure

As we mentioned in the Introduction, the values of signal and noise measured from the microscope imaging system are relative, so that the MSE bound (ZZB or PCRB) is also relative. The relative values are non-specific measures of the device's performance. For an explicit performance evaluation, we define a new performance measure, instead of using the MSE bound directly. In particular, we define the performance measure as the estimation error-to-signal ratio (ESR), by normalizing the MSE bounds of each microsphere over its shell intensity signal (θ_1 or θ_2). Note that because of the symmetry, the MSEs on estimates of θ_1 and θ_2 are equal. Because θ_1 and θ_2 are unknown, we use the *a priori* mean $0.5\theta_{\max}$ to represent them. Thus the ESRs for θ_1 and θ_2 are equal. We define the ESR for θ_1 or θ_2, whether computed by the ZZB or the PCRB, as

$$\mathrm{ESR}_{\mathrm{ZZB}} = \frac{\sqrt{0.5\mathrm{ZZB}(\boldsymbol{\theta})}}{0.5\theta_{\max}}, \quad \mathrm{ESR}_{\mathrm{PCRB}} = \frac{\sqrt{0.5\mathrm{PCRB}(\boldsymbol{\theta})}}{0.5\theta_{\max}}. \tag{2.17}$$

To evaluate the performances of the ZZB and the PCRB, we also compute the ESR for the simulated global maximum likelihood estimator (MLE) $\hat{\theta}_1$ or $\hat{\theta}_2$ in the Numerical Example (Section 2.4.1), and compare $\mathrm{ESR}_{\mathrm{ZZB}}$ and $\mathrm{ESR}_{\mathrm{PCRB}}$ against it.

2.3.5 Design Parameters and Experimental Variables

Now we state the motivation to select the optimal design parameters (distance d and imaging temperature T) and to investigate the effects of the experimental variables (the SNR, microscope PSF, and target concentration) on the position-encoded microsphere arrays' performance.

1) *Distance d between the microspheres*: Intuitively, a smaller d leads to a higher microsphere packing density (Fig. 2.1(a)). However, if d is too small, there will be optical cross-talk (interference) between the fluorescent shells of neighboring microspheres. This interference causes large errors in estimating the shell intensities. Therefore, it is desirable to select the optimal distance d_{opt} that achieves the highest packing density while ensuring negligible interference between the microspheres. Note that d relates to the ESR through the object model (2.2).

2) *Imaging temperature T*: T affects the dark and thermal noises of image sensors in imaging acquisition. Generally, CCD image sensors have little background noise [48], but they are less sensitive and more expensive than CMOS image sensors. CMOS sensors [47], though cheaper and more sensitive, produce more noise than CCD sensors, especially when T is high, so that external cooling is required to reduce the noise. This high noise drawback of the CMOS sensors in turn reduces estimation accuracy and adds additional cost for cooling. Therefore, in order to use CMOS sensors, we need to select the optimal T_{opt} in a trade-off between acceptable accuracy and minimal cooling. T is related to the noise levels in (2.7), and thus it is a parameter of the ESR.

3) *SNR*: Because the PCRB is not accurate at low SNR, while the ZZB is accurate in such cases, the SNR could be used to evaluate the accuracy of the two bounds for the design of the device. Moreover, studying the effect of the SNR (2.11) on the ESR tells us the required SNR to achieve a certain level of estimation accuracy in an experiment.

4) *Microscope PSF*: In fluorescence microscopy images, the microscope's PSF often causes severe distortion [49]. Therefore, it is of great importance to understand the effect of the microscope PSF on our device's performance. The variances σ_1^2 and σ_2^2 determine the Gaussian PSF model (2.4) and thus influence the ESR.

5) *Target concentration*: The unknown target concentration itself can be regarded as an experimental variable. Recall that the shell intensity θ is assumed to be linearly proportional to the target concentration (Section 2.3.1). Therefore, the value of $\theta_{\max}$ in $\theta \sim \mathcal{U}(0, \theta_{\max})$ provides an inference of the target concentration and is used to evaluate the ESR.

In summary, the design parameters d and T, and experimental variables such as SNR (w.r.t. noise levels), microscope PSF variances σ_1^2 and σ_2^2, and target concentrations (w.r.t. $\boldsymbol{\theta}$), all affect the device's performance ESR. Therefore, we can use the ESR to select the optimal design parameters and investigate the effects of the experimental variables for a desired performance (for example, an ESR below 10%).

2.4 Numerical Example

Here we use a numerical example to illustrate the statistical design, compare the ZZB with the PCRB at different SNRs, and demonstrate strategies to obtain d_{opt} and T_{opt}. We also use this example for a detailed discussion on the effects of the SNR, microscope PSF, and target concentration on the device's performance, which is an important extension of our previous work.

We define the diameter of the microsphere as 5.6 μm, and the shell radii $r_1 = 2.816$ μm and $r_2 = 2.847$ μm, which are consistent with the actual values in the imaging experiment in Section 2.5. We also use proper values for the experimental variables, namely, the prior maximum intensity $\theta_{\max}$, the noise levels σ_{d}^2 and σ_{t}^2, the imaging temperature T (°C), the photon conversion factor β, the microscope PSF variances σ_1^2 (μm^2) and σ_2^2 (μm^2), and the image sampling resolution $\Delta x, \Delta y$ (μm/pixel), and Δz (μm). Moreover, we set the desired performance as ESR$\leq$ 10% to assess the specific requirements for the design parameters.

2.4.1 Effect of SNR and Comparison between the Ziv-Zakai Bound and the Posterior Cramér-Rao Bound

To begin, we investigate the effect of the SNR and compare the performances of the ZZB and the PCRB. Explicitly, we compute the performance measures $\mathrm{ESR}_{\mathrm{ZZB}}$ and $\mathrm{ESR}_{\mathrm{PCRB}}$ at different SNRs. As a evaluation, we also compute $\mathrm{ESR}_{\mathrm{MLE}}$. The other variables are fixed, i.e., $\theta_{\max} = 5$, $d = 8.58$ μm, $\beta = 24$, $\sigma_1^2 = 0.75$ μm^2 and $\sigma_2^2 = 4$ μm^2, $\Delta x = \Delta y = 0.165$ μm/pixel, and $\Delta z = 0.2$ μm.

The ZZB was derived in Section 2.3.3, and the PCRB is [12]:

$$\mathrm{PCRB} = \mathrm{PCRB}(\theta_1) + \mathrm{PCRB}(\theta_2) = \mathrm{trace}(J^{-1}), \tag{2.18}$$

where J is the 2×2 symmetric Fisher information matrix with

$$\begin{aligned} J_{mn} = \mathrm{E}_{\boldsymbol{\theta}}\Bigg[\sum_z \sum_y \sum_x \Bigg(& \frac{s'_m(x,y,z) s'_n(x,y,z)}{\tilde{\boldsymbol{s}}(x,y,z;\boldsymbol{\theta})/\beta + \sigma_{\mathrm{d}}^2 + \sigma_{\mathrm{t}}^2} \\ & + \frac{(s'_m(x,y,z)/\beta)(s'_n(x,y,z)/\beta)}{2\big(\tilde{\boldsymbol{s}}(x,y,z;\boldsymbol{\theta})/\beta + \sigma_{\mathrm{d}}^2 + \sigma_{\mathrm{t}}^2\big)^2} \Bigg) \Bigg], m,n = 1,2, \end{aligned} \tag{2.19}$$

where $\mathrm{E}_{\boldsymbol{\theta}}[\cdot]$ is the expectation, $\tilde{\boldsymbol{s}}(\cdot)$ is expressed in (2.8), $s'_1(\cdot) = \partial \tilde{\boldsymbol{s}}(\cdot)/\partial\theta_1$, and $s'_2(\cdot) = \partial \tilde{\boldsymbol{s}}(\cdot)/\partial\theta_2$. The corresponding ESRs are then obtained by (2.17).

Figure 2.3 presents the ESRs versus the SNR. The ESRs are computed by the ZZB, the PCRB, and the MSE of the simulated MLE. It is obvious that the ZZB is tight to the simulated MLE across all SNRs, which means that it precisely bounds the MSE. In contrast, the PCRB fails to provide a tight bound, though it is close to the simulated MLE when the SNR is high. This figure confirms our expectation that the ZZB is a better lower bound than the PCRB, especially at low SNR values [40]. In addition, this figure gives the level of the SNR below which we should use the ZZB instead of the PCRB, in order to accurately choose the design parameters and investigate the effects of the experimental variables. In the current setup, this level of the SNR is 4 dB.

Figure 2.3 also demonstrates the effect of SNR on the ESR in the current setup, which guides us in determining the required value of SNR for a desired estimation accuracy. For example,

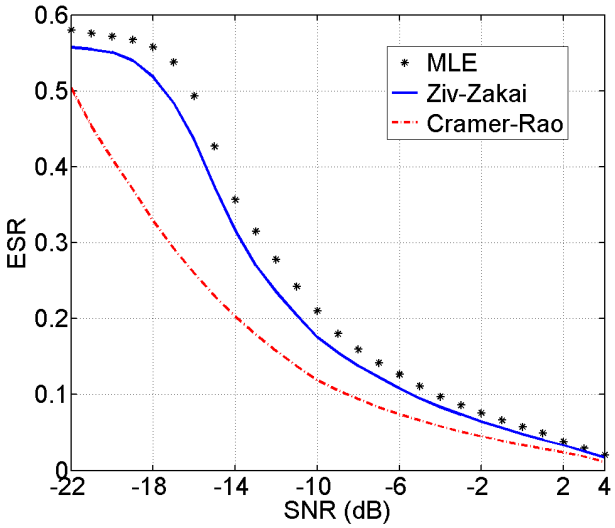

Figure 2.3: Comparison between the estimation error-to-signal ratio (ESR) computed by the Ziv-Zakai bound, the posterior Cramér-Rao bound, and the MLE, versus SNR.

to achieve an ESR below 10%, the SNR should be above -5 dB. Note that when the SNR is very low (< -20 dB), the ESR tends to plateau; this behavior is obtained by ignoring the measurements and estimating $\boldsymbol{\theta}$ by its *a priori* mean [40].

2.4.2 Selection of Optimal Distance between the Microspheres

Because the distance d influences the device's performance by determining the microsphere packing density and the microsphere interference, we now illustrate the selection of d_{opt}. In Fig. 2.4 we plot the ESR_{ZZB} as a function of distance d, at SNR $= -5$ dB. As a further comparison of the performances of the ZZB and the PCRB, we also plot the ESR_{PCRB}. Note that we use SNR $= -5$ dB for illustration because the ESR is around 10% and the difference between the ZZB and the PCRB is large (Fig. 2.3). The other variables have the same values as those in Section 2.4.1.

Figure 2.4 depicts that as d increases, ESR_{ZZB} and ESR_{PCRB} first decrease and then gradually flatten. The increased distance between the microspheres reduces the interference between their shell lights, and thus reduces the estimation error. When the interference is reduced to

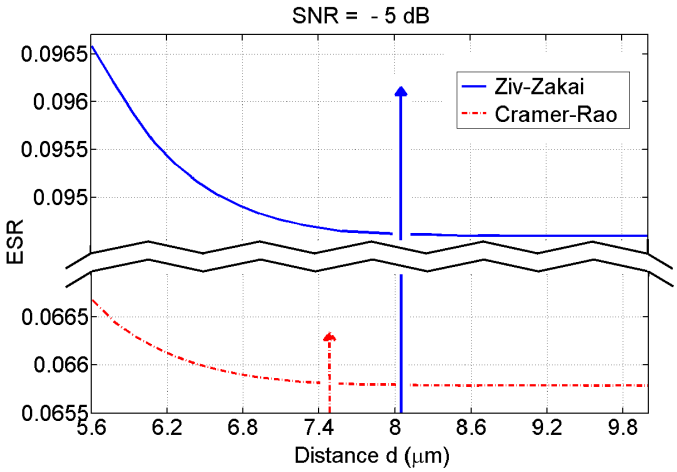

Figure 2.4: The effect and selection of optimal distance d_{opt}. We show the estimation error-to-signal ratio (ESR) computed by the Ziv-Zakai bound and the posterior Cramér-Rao bound, versus the distance d between two microspheres of diameter 5.6 μm, at SNR $= -5$ dB. The arrows indicate the optimal distances d_{opt}, and the zig-zag break along the y-axis is for better visualization.

a negligible level, the ESR is close to flat, as the estimation error at that point is essentially due to the background noise, which is independent of d.

To define the optimal distance d_{opt} (indicated by the arrows in Fig. 2.4), we choose the point where the slope of the ESR curves reduces to -10^{-4}, as after this point the change is negligible. Consequently, we obtain $d_{\text{opt}} = 8.075$ μm from the slope of ESR_{ZZB}. The d_{opt} determination method based on the ESR curve slope ensures consistency in our design under different conditions.

Figure 2.4 also confirms that the ZZB is tighter and more robust than the PCRB. The PCRB is too optimistic about the ESR.

2.4.3 Selection of Optimal Imaging Temperature

As we mentioned, the imaging temperature T affects both the dark and thermal noises of image sensors, and thus influences the device's performance. Now we demonstrate the

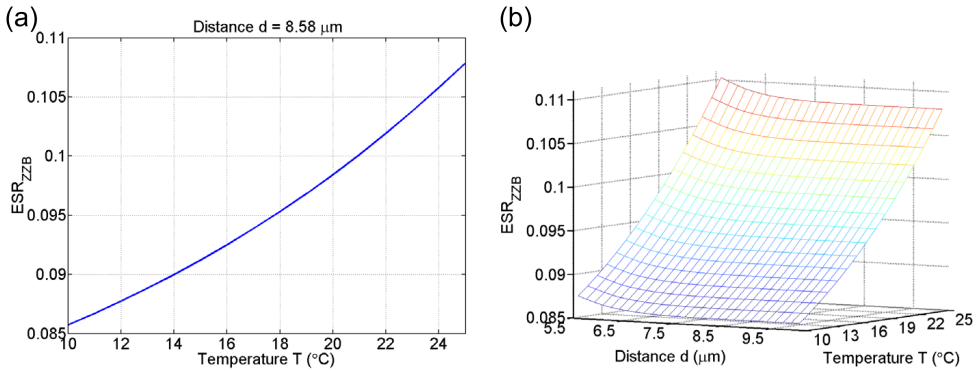

Figure 2.5: The effect and selection of temperature T. (a) The estimation error-to-signal ratio computed by the Ziv-Zakai bound ($\mathrm{ESR_{ZZB}}$) as a function of T at a distance $d = 8.58$ μm between two microspheres of diameter 5.6 μm. (b) The $\mathrm{ESR_{ZZB}}$ as a function of T and d.

selection of the optimal T_{opt} to yield acceptable estimation accuracy and minimal cooling, using the $\mathrm{ESR_{ZZB}}$.

In Fig. 2.5(a), we present the effect of T on the $\mathrm{ESR_{ZZB}}$, assuming we use a CMOS sensor that produces high noise at a high temperature T. Particularly, we assign relatively high noise levels as $\sigma_{\mathrm{d}}^2 = \sigma_{\mathrm{t}}^2 = 0.02075$ at $T = 25°\mathrm{C}$, and keep the other variables at the same values as in Section 2.4.1. We observe that the $\mathrm{ESR_{ZZB}}$ increases with increased T, which enables us to select the T_{opt} for a desired performance. For example, T_{opt} should be below 21°C to achieve an $\mathrm{ESR_{ZZB}}$ less than 10%.

Figure 2.5(b) presents a 3D plot of the effects of d and T on $\mathrm{ESR_{ZZB}}$. When using an image sensor with high noise, T appears to affect the performance more than d does.

2.4.4 Effect of the Microscope Point-Spread Function

From the microscope Gaussian PSF model in Eq. (2.4), the variances σ_1^2 and σ_2^2 determine the properties of the PSF. In Fig. 2.6(a), we plot $\mathrm{ESR_{ZZB}}$ as a function of distance d for different PSF variances in the xy focal plane: $\sigma_1^2 = 0.25$ μm^2, 0.75 μm^2, and 1.75 μm^2. We keep $\sigma_2^2 = 4$ μm^2 fixed along the z-axis. Recall that the optimal distance d_{opt} is chosen when the slope of the $\mathrm{ESR_{ZZB}}$ curve reduces to -10^{-4}. The corresponding d_{opt} are 7.095 μm, 8.075 μm, and 9.405 μm, respectively. Figure 2.6 shows that $\mathrm{ESR_{ZZB}}$ and d_{opt} increase with

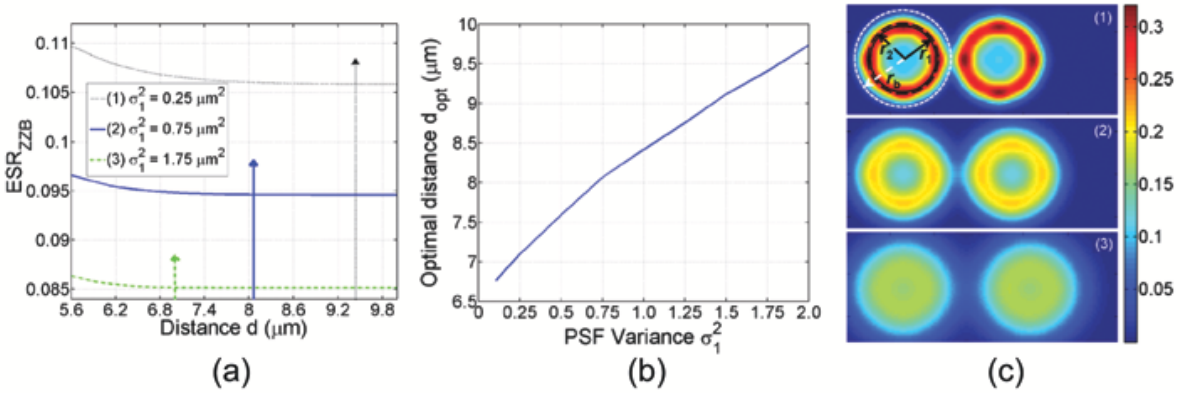

Figure 2.6: The effect of microscope point-spread function. (a) Performance measure computed by the Ziv-Zakai bound ($\mathrm{ESR}_{\mathrm{ZZB}}$) under different microscope PSF variances σ_1^2 (1)-(3), as a function of distance d between microspheres of diameter 5.6 μm. The arrows indicate the optimal distances d_{opt}: 7.095 μm, 8.075 μm, 9.405 μm, respectively. (b) The d_{opt} for different PSF variances σ_1^2. (c) Simulated xy focal plane ($z = 0$ μm) fluorescence intensity images of neighboring microspheres corresponding to (a)(1)-(3); the microspheres are separated at d_{opt}.

σ_1^2 because a larger PSF variance induces more blurring (distortion) around the illuminating objects, d has to be larger to reduce the interference between the microspheres to a negligible level. Therefore, the microscope PSF is one of the key factors that affects the value of d_{opt}.

To further interpret the effects of σ_1^2 on d_{opt}, we compute the $\mathrm{ESR}_{\mathrm{ZZB}}$ for different σ_1^2 and the corresponding d_{opt}. The PSF σ_1^2-d_{opt} relationship is shown in Fig. 2.6(b), which enables us to directly select the d_{opt} under a certain σ_1^2.

Figure 2.6(c) presents the simulated xy focal plane ($z = 0$ μm) intensity images of a pair of neighboring microspheres separated at $d_{\mathrm{opt}} = 7.095$ μm, 8.075 μm, and 9.405 μm, respectively. This figure illustrates the blurring caused by the microscope PSF. For example, in Fig. 2.6(c)-(1), the blurred region (white dashed circle with radius r_0) is much larger than the true illuminating region (black dashed circles with inner and outer radii r_1 and r_2). Moreover, from Fig. 2.6(c)(1)-(3), we can see that larger PSF variance σ_1^2 results in larger blurring and more substantial energy spreading.

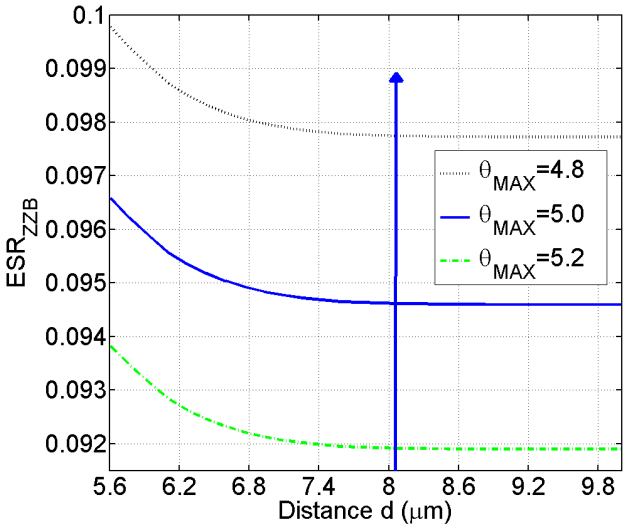

Figure 2.7: The effect of target concentration C. The estimation error-to-signal ratio computed by the Ziv-Zakai bound ($\mathrm{ESR_{ZZB}}$) as a function of the distance d between two microspheres of diameter 5.6 μm, at $\theta_{\max} = 4.8$, 5.0, and 5.2. The arrow indicates the optimal distance d_{opt}.

2.4.5 Effect of Target Concentration

In Fig. 2.7, we plot $\mathrm{ESR_{ZZB}}$ as a function of d, at $\theta_{\max} = 4.8$, 5.0, and 5.2 (recall from Section 2.3.5 that the target concentration is related to $\theta_{\max}$). This figure shows that $\mathrm{ESR_{ZZB}}$ decreases with increased $\theta_{\max}$, which means that a higher target concentration results in a smaller estimation error. This is reasonable, as a higher concentration produces a stronger signal for estimation. Meanwhile, we observe that d_{opt} does not change with varying $\theta_{\max}$, which suggests that our device designed by d_{opt} is robust for target detection across a wide concentration range.

2.5 Experimental Results and Discussion

We performed an imaging experiment with randomly-placed microspheres, an arrangement which is a typical of the conventional microsphere arrays. This experiment illustrates the

drawbacks of random placement, and it also helps us obtain the experimental variables and verify the selection of d_{opt} for the design of the position-encoded microsphere arrays.

In the experiment, polystyrene (PS) microspheres of diameter 5.6 μm (Spherotech Inc., Lake Forest, IL) were randomly placed on a glass slide. These microspheres were encoded with anti-IgG antibodies (~16 nm) on the surfaces as receptors. The targets, IgG proteins (~15 nm), were then bound to the anti-IgG antibodies on one side. The other side of the IgG proteins were conjugated with anti-IgG antibodies with Alexa 488 fluorescent dye (Life Technologies, Grand Island, NY). The fluorescent dye (~10 $\mathring{A}$) was introduced to label the target proteins. They emitted fluorescence upon excitation and formed a shell around each microsphere. The actual shell radii were $r_1 = 2.816$ μm and $r_2 = 2.847$ μm.

The microspheres with the receptors, targets, and dye were imaged using the Olympus Fluoview 1000 Confocal Microscope. A water immersion 60× objective was used to scan and record 91 images along the z axis (from -10 μm to 8 μm), and the step size Δz of these z-stack images was 0.2 μm. The imaging process was performed at 25°C. Each image had 640×640 pixels, with a resolution of $\Delta x = \Delta y = 0.165$ μm/pixel. These 91 images were further processed to collect the intensity measurements at each $[x, y, z]$ position and combine them into the measurement vector $\boldsymbol{g}$, as in our statistical model in Eq. (2.10). The experimental parameters are presented in Table 2.2.

Five trials were performed, and they all showed good consistency in microsphere sizes, shell fluorescence intensities, and noise levels. Considering the good consistency and reproducibility, we use the results of a single trial in the following sections, for simplicity.

2.5.1 Drawbacks of Random Placement of the Microspheres

Figs. 2.8(a) and 2.8(b) present the focal-plane normalized intensity images at $z = 0$ μm and $z = -4$ μm of the optical axis (z-axis) in one trial. In the two images, the microspheres are either widely separated or tightly clustered, which reflects that inefficient microsphere packing due to the random placement. In Fig. 2.8(a), the illuminating ring around every microsphere is the fluorescence emitted by the dyes, which indicates the existence of captured targets. The blurring at the edge of each ring shows the effect of the PSF distortion along the

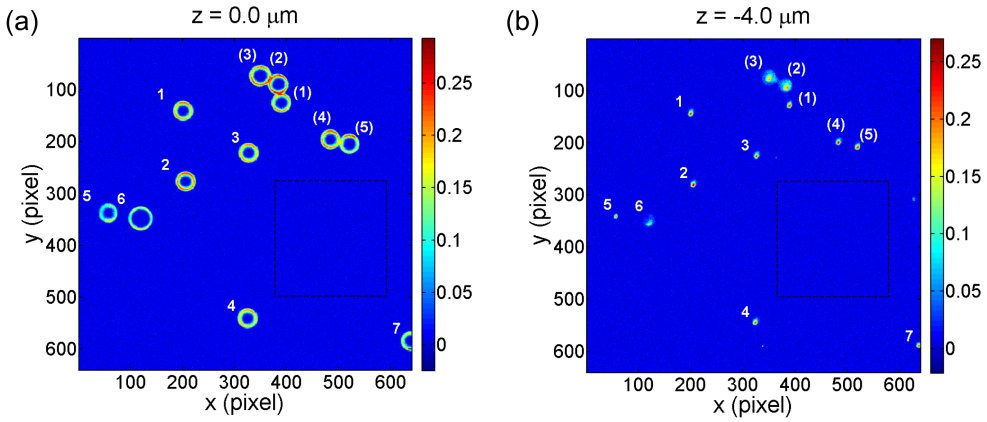

Figure 2.8: Real focal-plane normalized intensity images of 5.6 μm diameter microspheres at (a) $z = 0$ μm, (b) $z = -4$ μm, in one trial. Target IgG proteins were bound to antibodies on the surface of the microspheres. Anti-IgG antibodies with fluorescent dye were bound to the other side of the IgG. The dye emitted light upon excitation and formed spherical shells around the microspheres, which are the rings in the 2D focal plane images in (a). The *training* microspheres (individual microspheres) are indexed from 1-7, and the *test* microspheres (clustered microspheres) are indexed from (1)-(5). The noise-only section is marked with a black dashed rectangle, and is used to estimate the background noise levels (more details in Appendix B).

focal plane. The optical cross-talk among the clustered microspheres (indexed by (1)-(5)) indicates the interferences among them. When the microspheres are closely clustered, the interferences are very large (see Fig. 2.8(a)). The drawbacks of the randomly-placed microspheres motivate the design of the position-encoded microsphere arrays and demonstrate the importance of optimal distance selection.

There is measurable fluorescence on the $z = -4$ μm plane in Fig. 2.8(b), while no fluorescence should be expected because no targets exist there (the shell outer radius $r_2 = 2.847$ μm). This observation confirms the dramatic effect of the PSF distortion along the optical axis.

2.5.2 Verification of Optimal Distance Selection

We use this imaging experiment to obtain the experimental variables to compute the ESR and to select d_{opt} based on the ESR. Then we verify d_{opt} by comparing it with the distances

Table 2.1: Estimation of training and test microsphere parameters

Training Microsphere Index	1	2	3	4	5
$[\hat{x}_c$ (pixel), $\hat{y}_c$ (pixel), $\hat{z}_c$ (μm)]	[201,141,0]	[206,276,0]	[327,221,0]	[325,540,0.4]	[57,338,0.8]
Shell intensity $\hat{\theta}$	1.420	1.524	1.380	1.326	0.875
Photon-conversion factor $\hat{\beta}$	21.836	20.730	22.901	23.983	30.290
SNR (dB)	2.882	2.971	2.964	2.987	2.151
Test Microsphere Index No.	(1)	(2)	(3)	(4)	(5)
$[\hat{x}_c$ (pixel), $\hat{y}_c$ (pixel), $\hat{z}_c$ (μm)]	[390,126,0]	[384,89,-0.2]	[350,72,-0.2]	[483,196,0]	[521,205,0.2]
Microspheres' distance, (μm)	$d_{(1),(2)}$ 6.188		$d_{(2),(3)}$ 6.272		$d_{(4),(5)}$ 6.447

Table 2.2: Experimental parameters

Microscope	pinhole size 178 nm
Microscope objective	M_{obj} 60 × 1, NA 1.3, OTL 160 mm
Refractive index	n_{m} 1.33, n_{c} 1.515, n_{s} 1.57
Thickness (mm)	t_{m} 0.16, t_{c} 0.17, t_{s} 0.17
Wavelength (nm)	λ_{em} 505-530, λ_{ex} 488
Image resolution	$\Delta x, \Delta y$ 0.165 μm/pixel
Image spacing	Δz 0.2 μm
Imaging temperature	25°C

between the clustered microspheres in this experiment. Intuitively, when the distance between two microspheres is close to d_{opt}, their interference should be negligible. When the distance is much smaller than d_{opt}, the interference should be much larger.

We first estimate the experimental variables using the five microspheres appearing as individual objects (indexed 1-5 in Fig. 2.8). We call them *training* microspheres, and we discard the other two individual microspheres (indexed 6 and 7), because the size of microsphere 6 is not consistent with the other microspheres and the information of microsphere 7 is incomplete. From the measurements in the 91 z-stack images, for each *training* microsphere, the shell intensity $\hat{\theta}$, location (microsphere center) $[\hat{x}_c, \hat{y}_c, \hat{z}_c]$, and photon-conversion factor $\hat{\beta}$ are estimated (methods in [12]), and the SNR is computed (2.11). All the parameters for the *training* microspheres are presented in Table 2.1. We also estimate that the Gaussian PSF variances are $\hat{\sigma}_1^2 = 0.105$ μm^2 and $\hat{\sigma}_2^2 = 1.21$ μm^2, and that the noise levels are $\hat{\sigma}_d^2 = \hat{\sigma}_t^2 = 1.9782 \times 10^{-5}$ (methods in Appendixes A and B). Consequently, the maximum intensity level is $\hat{\theta}_{\max} = 1.524$, and the mean of $\hat{\beta}$ is $\bar{\hat{\beta}} = 23.948$.

Given all the estimated experimental variables, we compute the performance measures ESR_{ZZB} and ESR_{PCRB} (2.17). Then we plot the ESRs versus the distance d between the

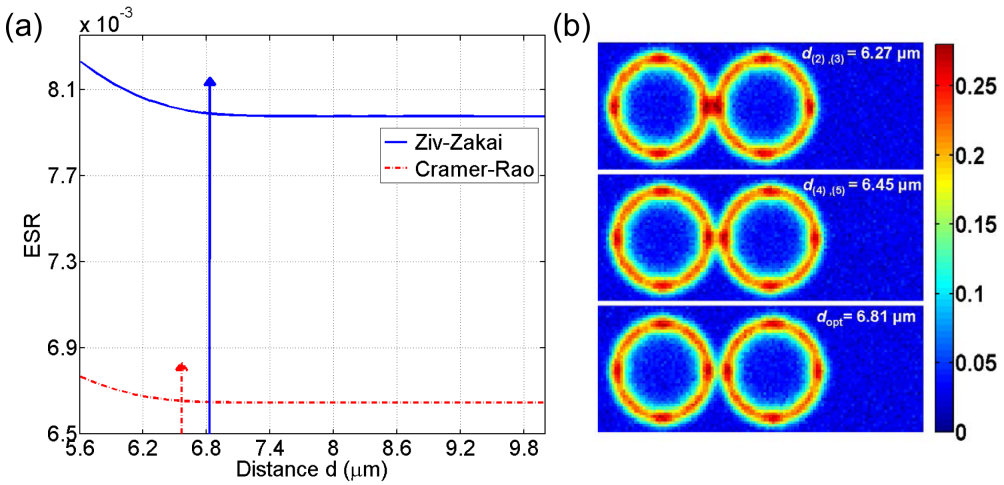

Figure 2.9: Design results based on the estimated parameters from the imaging experiment. (a) The estimation error-to-signal ratio (ESR) computed by the Ziv-Zakai bound and the posterior Cramér-Rao bound, as a function of the distance d between two microspheres of diameter 5.6 μm; $d_{\text{opt}} = 6.81$ μm. (b) Simulated focal plane ($z = 0$ μm) intensity image of two microspheres separated at $d_{(1),(2)} \approx 6.27$ μm, at $d_{(4),(5)} \approx 6.45$ μm, and at $d_{\text{opt}} = 6.81$ μm.

microspheres in Fig. 2.9(a). This figure shows that the magnitudes of both ESR_{ZZB} and ESR_{PCRB} are very small ($< 10^{-2}$), due to the high SNR (~3 dB) in this experiment. Yet ESR_{ZZB} is still slightly larger than the ESR_{PCRB}. This result is consistent with the observation in Fig. 2.3 of the numerical example in Section 2.4. We further obtain $d_{\text{opt}} = 6.81$ μm when the slope of the ESR_{ZZB} equals -10^{-4}.

To verify d_{opt}, we call the clustered microspheres in Fig. 2.8 *test* microspheres (indexed (1)-(5)). We also estimate the locations of the *test* microspheres (method in [12]), and then determine the distances between each two closely located *test* microspheres as $d_{(1),(2)} = 6.188$ μm, $d_{(2),(3)} = 6.272$ μm, and $d_{(4),(5)} = 6.447$ μm (Table 2.1). The *test* microspheres confirm that within the increase of d from very small to close to d_{opt}, the optical cross-talk (interference) between the microspheres is reduced. For example, as $d_{(4),(5)}$ is closest to d_{opt}, the cross-talk between *test* microspheres (4) and (5) is smallest. The cross-talk between microspheres (1) and (2) is most severe as $d_{(1),(2)}$ is farthest from d_{opt}.

Because no microspheres are found to be separated at d_{opt} in this imaging experiment, we plot the the simulated $z = 0.0$ μm focal-plane intensity image of two microspheres separated at $d_{\text{opt}} = 6.81$ μm in Fig. 2.9(b). For comparison, we also plot the simulated microspheres at

$d_{(2),(3)} \approx 6.27$ μm and $d_{(4),(5)} \approx 6.45$ μm in Fig. 2.9(b). We observe that the intensities and interference of the simulated microspheres are consistent with the *test* microspheres ((2)-(5)) in Fig. 2.8(a), and the interference between the microspheres at d_{opt} is negligible.

2.5.3 Discussion

The randomly-placed microsphere imaging experiment demonstrated the drawbacks of random placement, such as inefficient microsphere packing and erroneous target detection and estimation. It further verified the selection of optimal design parameters, which confirmed that our statistical analysis method lays the ground for the implementation of the position-encoded microsphere array device. The device is promising as a highly sensitive, accurate, and inexpensive tool for target detection and quantification.

In this imaging experiment, the estimated dark and thermal noises were very small (1.9782×10^{-5}) at the specific imaging temperature (25°C), and the ESR_{ZZB} was considerably low ($< 10^{-3}$ as shown in Fig. 2.9(a)). Therefore, the effect of T on the ESR_{ZZB} was not very significant; we did not investigate the optimal imaging temperature T_{opt}. The slight effect was attributed to the fact that we used an experimental setup with superior accuracy. In particular, the Olympus Fluoview 1000 Confocal Microscope with embedded CCD image sensor yields very few PSF abberations and a low noise level. Nevertheless, such a superior experimental setup is not always accessible. High noise still occurs on many occasions due to economic and technological limitations. For example, the use of cheaper CMOS image sensors will introduce much greater noise, as we discussed in Section 2.4.3, where the effect of T is not negligible. As our design aims to eventually enable mass production of an efficient and inexpensive device, the statistical performance analysis method, which is robust under different experimental conditions, is important for guiding the design strategy.

2.6 Summary

In this chapter, we computed the ZZB for the microsphere array device and demonstrated that it is more precise than the PCRB in typical low SNR situations, where most biological

experiments are performed. We defined a new performance measure, the ESR, to precisely assess the device's performance with respect to the target concentrations. With numerical examples, we investigated the level of the SNR below which the ZZB is more accurate than the PCRB is. We also demonstrated strategies for choosing the minimal distance d_{opt} between the microspheres, as well as the optimal imaging temperature T_{opt}, for a desired level of ESR_{ZZB}. We further quantitatively evaluated the effects of the microscope PSF and target concentration on the ESR_{ZZB} and d_{opt} in the image analysis. Evaluating the effects of these experimental variables provides valuable guides to the device's design, implementation, and subsequent use in experiments. Finally, an imaging experiment demonstrated and verified our design. Based on the statistical design, we have implemented the position-encoded microsphere array device, integrated with the microfluidics technology described in the next chapter.

Chapter 3

Optimization of Microfluidic Microsphere-Trap Arrays[2]

In the previous chapter, we provided the statistical design of position-encoded microsphere arrays, and used the Ziv-Zakai bound to investigate their performance. In this chapter, we implement the position-encoded microsphere arrays, integrated with microfluidic technology. We further develop an analytical framework to optimize the trap arrays.

3.1 Introduction

With the heightened interest in developing lab-on-a-chip medical diagnostic devices [1], [2], [3], there has been a growing need to bridge multiple disciplines in implementing such technologies to perform rapid disease diagnosis and prognosis [6]. In a single device, microarrays can detect different biological targets, such as DNAs, mRNAs, proteins, antibodies, and cells. They have recently been proven to be a powerful platform for building lab-on-a-chip systems [9]. To fabricate the microsphere array device, the industrial standard methods are robotic printing [20], photolithography patterned *in-situ* synthesis (such as Affymetrix) [21], and self-assembly of microbeads (such as Illumina) [16], [22]. However, due to the limited size of their printed spots, robotic-printed microarrays suffer from inhomogeneous distribution and inefficient packing [20]. Photolithographic patterned microarrays are costly and complicated to implement [21]. Self-assembled microarrays need specially fabricated substrates such

[2]Based on X. Xu, P. Sarder, Z. Li, and A. Nehorai, "Optimization of microfluidic microsphere-trap arrays", *Biomicrofluidics*, vol. 7, 014112, Feb. 2013.

as etched fiber optic bundles or silicon wafers, and thus they are also relatively expensive. To eliminate these drawbacks of the existing methods, researchers recently have implemented microsphere array systems by applying microfluidic technology (we refer to them as microfluidic microsphere-trap arrays) [23], [24], [25]. The microfluidics microsphere-array device has the advantages of a fast reaction rate due to active flow and a gentle liquid environment for biological samples. The device also can employ on-chip micromechanical valves and isolated chambers to distinguish diverse targets in its different compartments [31], [35].

As an independent and dedicated platform, the performance of the microfluidic microsphere-trap array device depends on careful optimization of the device architecture. Several criteria should be taken into account, including maximizing the microspheres' packing density to make the device compact, efficiently immobilizing microspheres, effectively eliminating fluidic errors, minimizing errors introduced during the device's fabrication, and minimizing aberrations induced during the subsequent fluorescence imaging [12]. However, to date (to our knowledge) no studies have been reported on simultaneous optimization of these multiple criteria.

To address the above problems, we design a novel trap array geometry (traps in inverted-trapezoid shapes) and employ a hydrodynamic trapping mechanism to immobilize the microspheres in the traps. Further, we develop an analytical method to optimize the values of the trap's geometric parameters to maximize the microsphere arrays' packing density. In this optimization, we simultaneously satisfy other criteria also, such as efficiently immobilizing a single microsphere in a single trap, effectively eliminating fluidic errors, and minimizing errors in imaging the microspheres. We compute the optimized geometric parameters for a device capturing microspheres of radius 5 μm, and use finite element simulations to validate the trapping mechanism and investigate the effects of these parameters on the packing density. Microsphere-trapping experiments performed using the optimized device demonstrate easy control of the transportation, immobilization, and manipulation of microspheres in the trap arrays. We also fabricate another device with randomly selected values of the geometric parameters, which we call the un-optimized device for reference. Further quantitative comparisons also show that the optimized device greatly outperforms the un-optimized device. The optimized device has a much higher packing density (1438 traps/mm^2) than that of the un-optimized one (762 traps/mm^2). Moreover, the optimized device has a higher microsphere trapping efficiency (only a single microsphere in a trap) than the un-optimized one.

In particular, for the former, more than 99% of the traps are found to be filled with a single microsphere, whereas for the latter the percentage is 58%.

This chapter is organized as follows. Section 3.2 describes the structure of our device, the hydrodynamic trapping mechanism to immobilize the microspheres in the traps, and the optimization formulation of the trap geometry. Section 3.3 shows the finite element fluid dynamics simulation results. In Section 3.4, we compare the results of the microsphere trapping experiments using the optimized device and the un-optimized device. We also discuss the comparison between our device and self assembled three-dimensional (3D) microarrays, and comparison with other hydrodynamic mechanisms. Section 3.5 summarizes the chapter.

3.2 Optimizing Microfluidic Microsphere-Trap Arrays

We first briefly describe the structure of our microsphere-trap arrays and the hydrodynamic trapping mechanism. We then present the geometry of a single trap and its surrounding microfluidic channels and formulate the optimization problem for this geometry. We note that *trapping* here means to immobilize the microspheres at predetermined locations in the trap arrays during the experiments, as Fig. 3.1 shows. Embedded receptors on the trapped microspheres capture targets in subsequent experiments [12], [13].

3.2.1 Structure of the Microfluidic Microsphere-Trap Arrays

Figure 3.1(a) is a schematic diagram of the microfluidic microsphere-trap arrays. It presents the top view of the microfluidic channels with hydrodynamic trap arrays. The traps in the arrays are made of polydimethylsiloxane (PDMS), shaped into inverted-trapezoid grooves. The microfluidic channels are connected with each other by a common inlet and outlet, as shown in Fig. 3.1. Note that a microfluidic channel runs between any two consecutive traps and between any two rows of the trap array. To fill the traps, a liquid, such as phosphate buffered saline (PBS), carries microspheres with specific receptors through the channels, and the traps immobilize the microspheres during the process. When re-using the device, to avoid

cross contamination, before new microspheres are loaded, the residual old microspheres are washed out using buffer solution.

In our design of the trap array device, each row of the traps is offset horizontally with respect to the one above it (Fig. 3.1(a); inset ***a***). This offset ensures that the microspheres not trapped by the first row can easily be captured by the next row of traps. The separations between adjacent traps and rows are optimized to ensure minimal channel clogging (Channel clogging refers to obstruction in a channel region that restricts the flow of microspheres. As a result, unwanted microspheres aggregate in that region [50]). Such separations also eliminate the possibility of two microspheres arriving at a trap simultaneously and contending to fill in the same trap.

Next we will explain the hydrodynamic trapping mechanism of microspheres in the trap arrays. We remind the readers that the device is designed for use in detecting multiple targets, such as DNAs and antibodies, captured by receptors embedded on the surface of the microspheres [12], [13].

3.2.2 Hydrodynamic Trapping Mechanism

The proposed device employs fluidic resistance engineering to perform hydrodynamic trapping of microspheres [24], [51], [52]. To explain this mechanism, we schematically present the possible flow paths of a microsphere in Fig. 3.1(b). In this figure, path P_1 (pink line) is the *trapping* path and path P_2 (green line) is the *bypassing* path. Here we define *trapping* as a microsphere flowing into the trap, and we define *bypassing* as the flow of subsequent microspheres through the channels next to the trap. This scheme for a single trap is applicable for all the traps.

In order to trap the microspheres as shown in Fig. 3.1(b), the trap array geometry should be designed so that the *trapping* path P_1 for an empty trap has a lower flow resistance than the *bypassing* path P_2. Then during the loading process, a microsphere in the fluid is most likely to move into an empty trap through P_1 (Fig. 3.1(b) top). However, once the trap through P_1 is loaded by a microsphere, the flow resistance in P_1 dramatically increases and is much

larger than that in P_2, and thus subsequent microspheres divert to path P_2 and bypass the filled trap (Fig. 3.1(b) bottom).

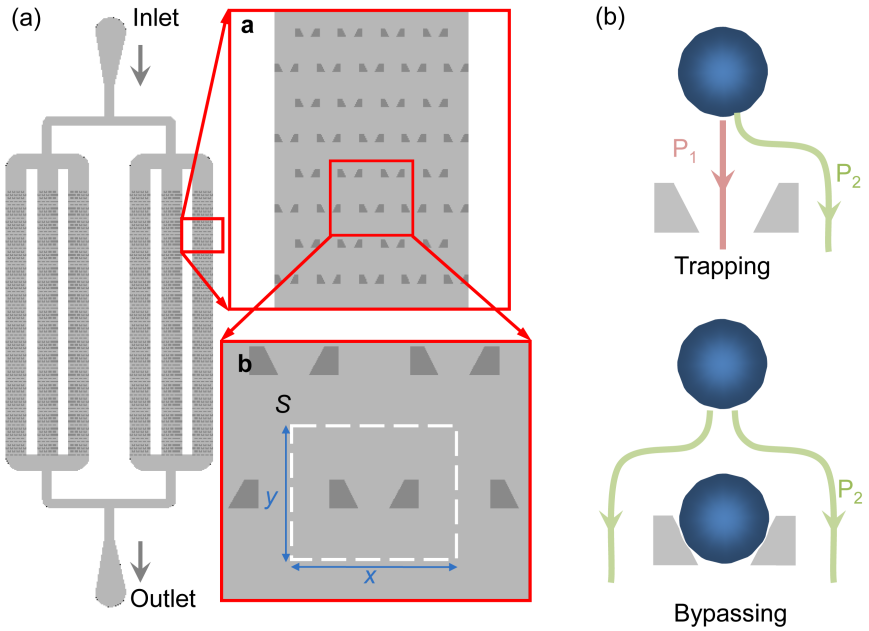

Figure 3.1: Schematic diagram of the microfluidic microsphere-trap arrays. (a) Layout (top view): Microfluidic channels with hydrodynamic trap arrays. The channels are connected by a common inlet and a common outlet. A liquid solution carrying the microspheres flows from the inlet and through the channels. Microspheres are immobilized by the trap arrays during the process. Inset ***a*** shows a zoomed-in view of trap arrays in a microfluidic channel, and inset ***b*** shows a single trap. The white dashed square shows the area S of the single trap and its surroundings, whose length and width are x and y. (b) Trapping mechanism: The top figure shows how an empty trap automatically captures a single microsphere, because path P_1 is designed to have a lower flow resistance than path P_2. We call this mechanism as *trapping*. Once the trap through P_1 is filled, the flow resistance of P_1 increases dramatically and is much larger than that in P_2. Thus, subsequent microspheres flow through P_2. We call this mechanism as *bypassing*.

3.2.3 Trap Geometry and Optimization

Obeying the hydrodynamic trapping mechanism explained above, we have designed a modular trap geometry to immobilize the microspheres, particularly to ensure a single microsphere in each trap. We have optimized this geometry to increase the microspheres' packing density

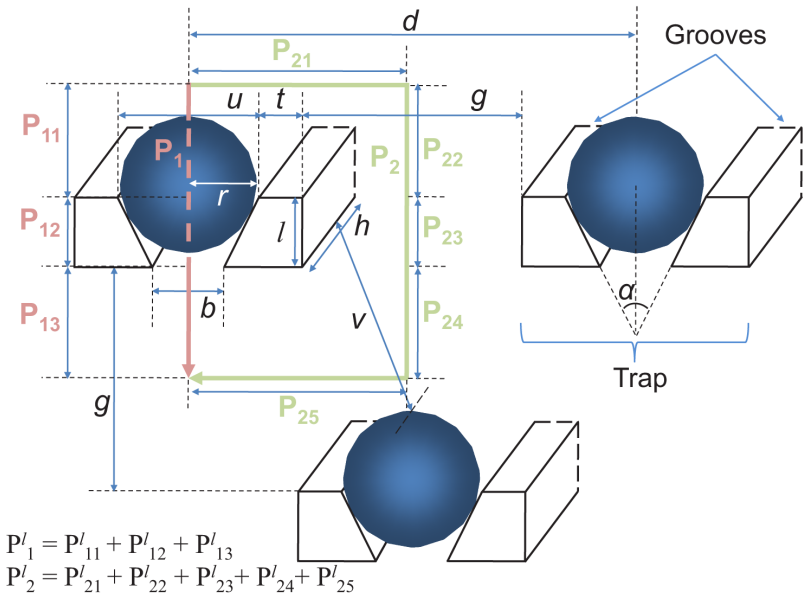

Figure 3.2: Schematic diagram of the proposed trap array geometry. Three adjacent traps are presented here, with the first two traps in the same row and the third trap in a subsequent row. Each trap is made of inverted-trapezoid grooves. This diagram also shows the two flow paths of a microsphere encountering the first trap: the *trapping* path (pink line) and the *bypassing* path (green line). The microsphere chooses the *trapping* path when it experiences smaller flow resistance in this path than in the *bypassing* path; otherwise it chooses the *bypassing* path. The *trapping* path consists of the sub-paths P_{11}, P_{12}, and P_{13}, and the *bypassing* path consists of the sub-paths P_{21}, P_{22}, P_{23}, P_{24}, and P_{25}; see more details in *Constraint 1* of Subsection Optimization constraints.

and simultaneously satisfied other design criteria, such as eliminating channel clogging [50], avoiding multiple microspheres trapping at one trap location, satisfying the trap array device's microfabrication tolerance and feasibility [53], and achieving the optimal distance d_0 between microspheres obtained in the statistical design to minimize image analysis error [12]. Image analysis error is experienced during analysis of the fluorescence images of targets captured by the microsphere array device [12]. In the following, we first present the proposed trap geometry, then discuss the formulation of the optimization for this geometry, including the objective function and constraints.

Figure 3.2 shows a schematic diagram of the trap geometry and depicts the corresponding geometric parameters. We denote the radius of the microsphere as r; the height of the groove walls (i.e., height of the channel) as h; the length and the upper width of the groove

walls as l and t, respectively; the trapezoidal angle of the trap as α; and the upper and the bottom widths of the trap opening as u and b, respectively. We also denote the width of the channel as g, the distance between two microspheres in the same row as d, and the minimal distance between a trap and a microsphere caught in a consecutive row as v. To eliminate the units of these parameters, we normalize them by dividing by the groove walls' height h (see Fig. 3.2). We use below the tilde sign ˜ to represent the resulting normalized parameters; e.g., $\tilde{r}$ represents normalized r. Furthermore, we denote the area of a single trap and its surroundings as S, whose length and width are x and y, respectively (see the white dashed square in Fig. 3.1(a); inset $\boldsymbol{b}$). Finally, we denote the packing density of the arrays as ρ.

Optimization objective function

We aim to maximize ρ of the microsphere arrays. This is equivalent to minimizing the area S of each trap and its surroundings, as seen in Figs. 3.1 and 3.2. From these figures,

$$x = u + 2t + g, \quad y = g + l, \quad S = xy. \tag{3.1}$$

Therefore, the optimization objective function is $\rho = 1/S$, where S is to be minimized with respect to the trap array geometric parameters $\boldsymbol{\delta} = [r, h, l, u, b, t, g, d, v]^T$. For simplicity, we keep the values of r and h fixed in $\boldsymbol{\delta}$, and optimize the other parameters. To summarize, the optimization objective is

$$\rho_{\text{opt}} = 1/S_{\text{opt}}, \text{ with } S_{\text{opt}} = h^2 \cdot \min_{\boldsymbol{\delta}} (\tilde{g} + \tilde{l}) \cdot (\tilde{u} + 2\tilde{t} + \tilde{g}). \tag{3.2}$$

Optimization constraints

The optimization constraints are formulated to achieve the multiple criteria we proposed in Section 3.1, i.e., the desired hydrodynamic trapping, feasible device fabrication, high microsphere trapping efficiency, small fluidic errors, and minimal errors in imaging the microspheres after they capture targets. Details are given below.

- *Constraint $\mathcal{C}_1$:* We first formalize the constraint for the desired hydrodynamic trapping. According to this mechanism, for an empty trap, we require a smaller flow resistance in path P_1 (pink line in Figure 3) than that in path P_2 (green line). This in turn requires the volumetric flow rate Q_1 along the path P_1 be higher than the rate Q_2 along the path P_2 [51], [52], and thus the volumetric flow rate ratio $Q_1/Q_2 > 1$. Note that volumetric flow rate defines the volume of fluid that passes through a given orifice per unit time [54]. Volumetric flow rates Q_1 and Q_2 are related to the pressure drops along the paths P_1 (ΔP_1) and P_2 (ΔP_2), respectively [51], [52]. Therefore, we compute ΔP_1 and ΔP_2 first.

  The general expression of the pressure drop ΔP in a rectangular microchannel is derived [24] based on the Darcy-Weisbach equation and the Hagen-Poiseuille flow problem for continuity and momentum equations [55]. Here, fully established flow is assumed inside the trapping area, which in practice can be achieved by fabricating the trapping area far enough from the liquid entrance port. The expression of ΔP is given by

$$\Delta P = \frac{f(\beta)\mu Q C^2 L}{32 A^3}, \tag{3.3}$$

  where μ is the fluid viscosity, L is the length of the channel, Q is the volumetric flow rate, and A and C are the channel's cross-sectional area and perimeter. The function $f(\beta)$ is a known polynomial of the aspect ratio β [54], which is given by

$$f(\beta) = 96(1 - 1.3553\beta + 1.9467\beta^2 - 1.7012\beta^3 + 0.9564\beta^4 - 0.2537\beta^5), \tag{3.4}$$

  where β is the ratio of the height and width of the rectangular channel, such that $0 \leq \beta \leq 1$.

  For the trap array geometry in Fig. 3.2, we compute ΔP_1 and ΔP_2 as explained below.

  ΔP_1 (pink line in Fig. 3.2): Path P_1 consists of the sub-paths P_{11} (above the trap), P_{12} (through the trap), and P_{13} (below the trap). We have the length of P_{12} as $P_{12}^{l} = l$, where l has been defined as the length of the groove. The width of P_{12} continuously changes from the top opening u to the bottom opening b, both of which are several μm long. Moreover, the widths of P_{11} and P_{13} equal the length of the whole horizontal channel, which is more than 1×10^3 μm long. Therefore, the widths of P_{11} and P_{13} are much greater than that of P_{12}, the pressure drops

along P_{11} and P_{13} are negligible, and most of the pressure drop in P_1 occurs along P_{12} [54].

Therefore, from Eq. (3.3) and Fig. 3.2, we have

$$\Delta P_1 = \int_0^l \frac{f(\beta)\mu Q_1 C^2}{32A^3}\,\mathrm{d}l', \tag{3.5}$$

where $A = wh$, $C = 2(w + h)$, and $\beta = w/h$, with w denoting the width of P_{12}. For the sub-path P_{12} through the trap, at any moment the microsphere is flowing in a piece-wise rectangular channel of infinitesimally small width dw. This infinitesimal metric changes with the length l of the triangular shape inside the trap, and we thus substitute l for w while deriving the pressure drop along P_{12}. Therefore, substituting $w = \frac{(b-u)}{l} \cdot l' + u$, $\tilde{w} = w/h$, and $\tilde{l}' = l'/h$ into Eq. (3.5), we obtain

$$\Delta P_1 = \int_0^{\tilde{l}} \frac{f(\tilde{w})\mu Q_1 (\tilde{w}+1)^2}{8\tilde{w}^3 h^3}\,\mathrm{d}\tilde{l}'. \tag{3.6}$$

ΔP_2 (green line in Fig. 3.2): Path P_2 has the same start and end points as path P_1, and it consists of the sub-paths P_{21} (above the trap), P_{22} (above the separation between the traps), P_{23} (through the separation between the traps), P_{24} (below the separation between the traps), and P_{25} (below the trap). Again, the widths of P_{22} and P_{24} (equaling the length of the whole horizontal channel) are so large that we ignore the pressure drops along them. Most of the pressure drops happen along the sub-paths P_{21}, P_{23}, and P_{25}, which have the same width g. The length of P_2^{l} becomes $P_2^{\mathrm{l}} = P_{21}^{\mathrm{l}} + P_{23}^{\mathrm{l}} + P_{25}^{\mathrm{l}} = \mathrm{u} + 2\mathrm{t} + \mathrm{g} + \mathrm{l}$. Therefore, using $A = gh$ and $C = 2(g + h)$ in Eq. (3.3), we obtain

$$\Delta P_2 = \frac{f(\bar{\tilde{g}})\mu Q_2 (\tilde{g}+1)^2 \tilde{P}_2^l}{8\tilde{g}^3 h^3}, \tag{3.7}$$

where $\tilde{P}_2^l = P_2^{\mathrm{l}}/\mathrm{h}$, $\bar{\tilde{g}} = \tilde{g}$ if $\tilde{g} \leq 1$, and $\bar{\tilde{g}} = \tilde{g}^{-1}$ otherwise.

Equating ΔP_1 and ΔP_2, we obtain the expression of Q_1/Q_2. Recall that we require $Q_1/Q_2 > 1$ to achieve hydrodynamic trapping, *Constraint 1* is $\mathcal{C}_1 = \{G(\boldsymbol{\delta}) < 0\}$,

where

$$G(\boldsymbol{\delta}) = \int_0^{\tilde{l}} \frac{f(\tilde{w})(\tilde{w}+1)^2}{\tilde{w}^3}\,\mathrm{d}\tilde{l}' - \frac{f(\bar{\tilde{g}})(\tilde{g}+1)^2\tilde{\mathrm{P}}_2^l}{\tilde{g}^3}. \tag{3.8}$$

- *Constraint $\mathcal{C}_2$:* To ensure that a microsphere is captured in a trap and to reduce the chance that multiple microspheres are in a trap, we require b to be smaller than the microsphere's diameter ($\tilde{b} < 2\tilde{r}$). We also require u and l to be smaller than the sum of two microspheres' diameters ($\tilde{u} < 4\tilde{r}$ and $\tilde{l} < 4\tilde{r}$). To avoid cases where fabrication variations would not allow the values of these parameters to satisfy this constraint, we use 0.2 μm safety margin [56]. Therefore, *Constraint 2* is given by $\mathcal{C}_2 = \{\tilde{b} \leq 2\tilde{r} - 0.2/h,\ \tilde{u} \leq 4\tilde{r} - 0.2/h,\ \tilde{l} \leq 4\tilde{r} - 0.2/h\}$.

- *Constraint $\mathcal{C}_3$:* To ensure stable trapping of the microspheres, i.e., a microsphere is retained in a trap and is not swept away due to the transient flow motion around the trap, we require the trapezoid angle $\alpha = 2\arctan\left(\frac{0.5(\tilde{u}-\tilde{b})}{\tilde{l}}\right)$ to be greater than 5°. For α smaller than 5°, the vertical component of the trapping force would become too small to hold the microspheres in the traps, and we observed in experiments that the microspheres can escape through the openings. We also require l to be larger than the radius of the microsphere ($l > r$). Therefore, *Constraint 3* is $\mathcal{C}_3 = \{-\alpha \leq -5°,\ -\tilde{l} \leq -\tilde{r}\}$.

- *Constraint $\mathcal{C}_4$:* To avoid channel clogging, we require $\tilde{g} > 2\tilde{r}$ to allow one microsphere to flow through the channel during the *bypassing* process. We also require $\tilde{g} < 4\tilde{r}$ to avoid multiple microspheres flowing side by side through the channel. Similar to *Constraint 2*, we use 0.2 μm margins, considering fabrication variations. Therefore, we modify this inequality to be $2\tilde{r} + 0.2/h < \tilde{g} < 4\tilde{r} - 0.2/h$.

  We also require v, the minimal distance between a trap and a microsphere filled in a consecutive row, to be greater than the microsphere's diameter, i.e., $\tilde{v} > 2\tilde{r}$, where $\tilde{v}^2 = (\tilde{g} - \sqrt[2]{\max(0, \tilde{r}^2 - (0.5\tilde{u})^2)} - \tilde{r})^2 + (0.5\tilde{g})^2$. Allowing for fabrication variations, the requirement becomes $\tilde{v} > 2\tilde{r} + 0.2/h$. Therefore, *Constraint 4* is $\mathcal{C}_4 = \{\tilde{g} \leq 4\tilde{r} - 0.2/h, -\tilde{g} \leq -2\tilde{r} - 0.2/h, -\tilde{v} \leq -2\tilde{r} - 0.2/h\}$.

- *Constraint $\mathcal{C}_5$:* For fabrication feasibility, the possible aspect ratios (the ratio of transverse dimensions to height, for example, t/h, i.e., $\tilde{t}$) of the geometric parameters in the device should be limited to the range of $[0.4, 2.5]$. Features with too small aspect ratios

are difficult to fabricate using soft lithography, and channels with too large aspect ratios easily collapse. Therefore, *Constraint 5* is $\mathcal{C}_5 = \{\tilde{l}, \tilde{g}, \tilde{b}, \tilde{u}, \tilde{t} \leq 2.5, -\tilde{l}, -\tilde{g}, -\tilde{b}, -\tilde{u}, -\tilde{t} \leq -0.4\}$.

- *Constraint $\mathcal{C}_6$:* To minimize the error in imaging the targets captured by the microspheres, the distance $d = u + 2t + g$ between the centers of two immobilized microspheres should be greater than the minimal distance d_0 that can be computed using the method developed in our earlier publication [12]. Therefore, *Constraint 6* is given by $\mathcal{C}_6 = \{-\tilde{d} \leq -\frac{d_0}{h}\}$.

The optimization problem is summarized as

$$\boxed{\rho_{\text{opt}} = 1/S_{\text{opt}}, \text{ with } S_{\text{opt}} = h^2 \cdot \min_{\boldsymbol{\delta}} (\tilde{g} + \tilde{l}) \cdot (\tilde{u} + 2\tilde{t} + \tilde{g}),} \tag{3.9}$$

where $\boldsymbol{\delta} \in \{\mathcal{C}_1 \bigcap \mathcal{C}_2 \bigcap \mathcal{C}_3 \bigcap \mathcal{C}_4 \bigcap \mathcal{C}_5 \bigcap \mathcal{C}_6\}$.

To solve Eq. (3.9), we used the interior-point optimization algorithm [57]. We further confirmed the result obtained from this method using the grid-search method [58] on the feasible parameter space defined by $\boldsymbol{\delta}$.

3.3 Finite Element Fluid Dynamics Simulations

In this section, by solving Eq. (3.9), we compute the optimum trap array geometry for capturing microspheres of radius $r = 5$ μm. We use finite element fluid dynamics simulations to validate the hydrodynamic trapping of the microspheres in the device. We also investigate the sensitivities of the packing density ρ to the geometric parameters in $\boldsymbol{\delta}$, to evaluate the effects of these parameters.

First, we set the fixed parameter h to be 13 μm, for microspheres of radius 5 μm. For our optimization, h acts as a normalizing factor but does not affect the packing density of the device. However, h should be larger than one microsphere's diameter to avoid the microsphere flowing out of the channel. It also should be shallow enough to avoid one microsphere flowing on top of another microsphere so that the two arrive at the trap simultaneously.

Table 3.1: Fixed and optimized geometric parameters for the microfluidic microsphere-trap array

Fixed values (μm)	r	h			
	5	13			
Optimized values (μm)	l_{opt}	u_{opt}	b_{opt}	t_{opt}	g_{opt}
Interior-point	5.210	10.001	6.915	5.205	14.546
Grid-search	5.200	10.020	6.900	5.200	14.600

Based on experimental testing results, we choose $h = 2.6r$. The values of r and h are summarized in Table 3.1. We note that the minimum distance d_0 to minimize the imaging error for microspheres of radius 5 μm is 20 μm [12].

We then obtain the optimum values of the parameters in $\boldsymbol{\delta}$, following the method described in the previous section. As stated, the interior-point algorithm and the grid-search method are used to solve Eq. (3.9). The two optimization methods give almost identical results for the optimization parameters l, u, b, t, and g; see Table 3.1. To restate, l is the length of the groove wall, u is the upper width of the trap opening, and b is the bottom opening width. t is the upper width of the groove wall, and g is the width of the channel. Note that the parameters d and v are not listed because they are functions of the other parameters. The S_{opt} computed from the interior-point method and the grid-search method are 690.61 mm^2 and 686.39 mm^2, respectively, with corresponding ρ_{opt} of 1448 traps/mm^2 and 1456 traps/mm^2.

To validate the hydrodynamic trapping mechanism for immobilizing the microspheres in our device, we perform finite element simulation of the transient motion of the microspheres flowing with the fluid into the device, using COMSOL Multiphysics 4.3 [59]; the simulation details are described in Chapter 4. Due to the high computational demand in 3D fluid dynamics simulations, the simulations are done in 2D. The accuracy of the 2D time-dependent simulations of the hydrodynamic trapping of microspheres is validated by experiments in Chapter 4. Figs. 3.3 and 3.4 present the positions of the microspheres, as well as the fluid velocity surface plot and streamline plot, at several time points. Particularly, Fig. 3.3 demonstrates that when the trap is empty, the microsphere directly flows into the trap and is immobilized (the *trapping* process). Figure 3.4 shows that when the trap is filled with a microsphere, the subsequent microsphere passes by the trap (the *bypassing* process). These finite element simulation results clearly verify the flow-resistance-based design parameters given above.

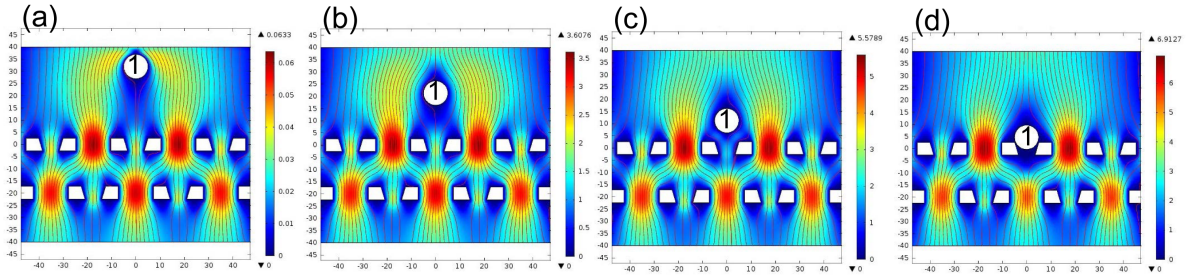

Figure 3.3: Finite element fluid dynamics simulation of one microsphere (denoted as 1) being *trapped* in an empty trap ((a) - (d)). Fluid flows into the inlet with fully developed laminar characteristics with a parabolic velocity profile. The boundary condition for the outlet is 0 Pa pressure with no viscous stress.

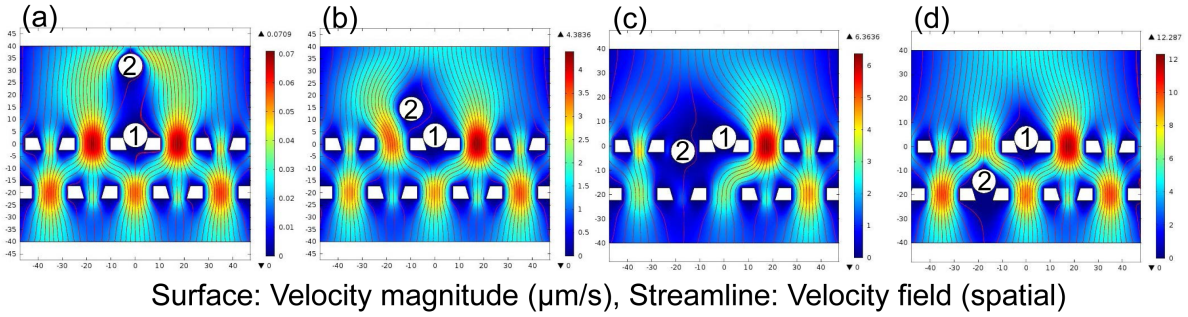

Figure 3.4: Finite element fluid dynamics simulation of one microsphere (denoted as 2) *bypassing* a trap ((a) - (d)), when the trap is already filled by a microsphere (denoted as 1). Fluid flows into the inlet with fully developed laminar characteristics with a parabolic velocity profile. The boundary condition for the outlet is 0 Pa pressure with no viscous stress.

To study the effects of the optimization geometric parameters and compare the different sensitivities of ρ in response to their changes, in Fig. 3.5 we plot ρ as individual functions of l, u, b, t, and g. In each sub-plot of a specific parameter, the range of the x-axis is this parameter's feasible range as determined by the optimization constraints (Eq. (3.9)), and the other four parameters are all set at their optimum values, obtained from the grid-search method. For example, in Fig. 3.5(a), l is feasible in the range [5.2 μm, 18 μm], $u = u_{\text{opt}}$ (10.02 μm), $b = b_{\text{opt}}$ (6.9 μm), $t = t_{\text{opt}}$ (5.2 μm), and $g = g_{\text{opt}}$ (14.6 μm). Among the five parameters, g appears to exert the most dramatic effect on ρ (Fig. 3.5(e)). Explicitly, a slight increase of g above the optimum value $g_{\text{opt}} = 14.6$ μm induces a large decrease in ρ, as indicated by the largest first derivative of ρ with respective to g. In contrast, l, u, and t are

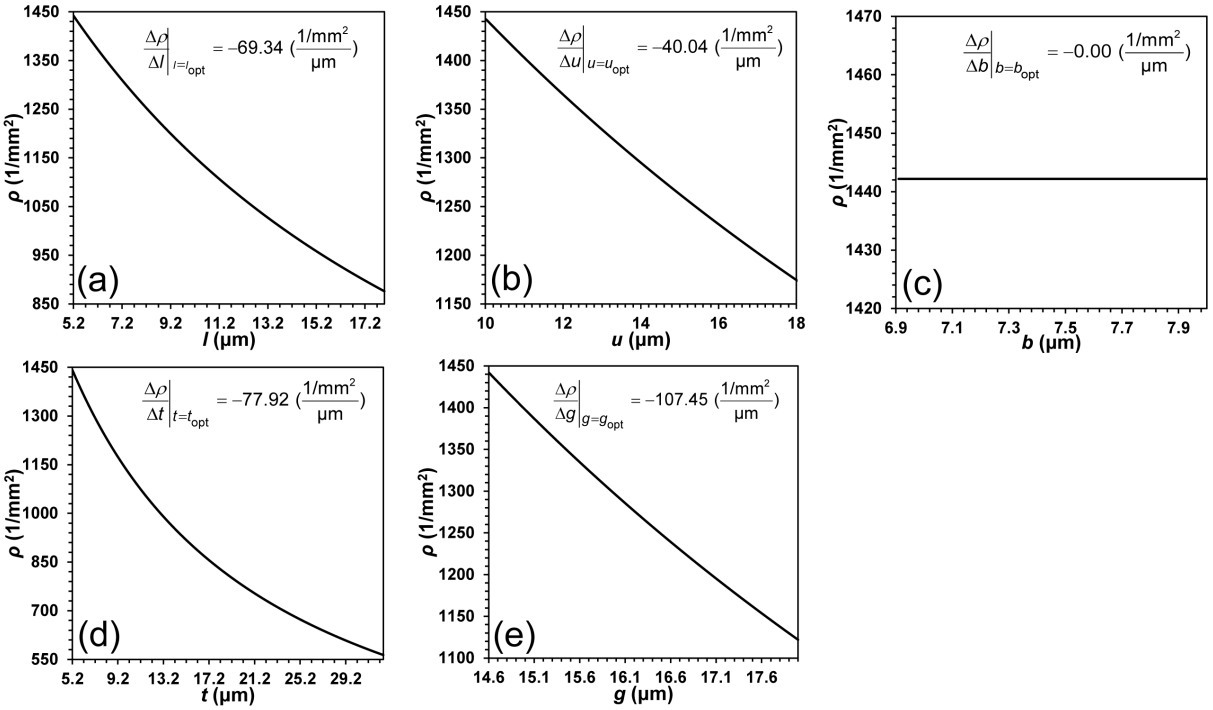

Figure 3.5: Effects of the optimization geometric parameters of (a) l, (b) u, (c) b, (d) t, and (e) g, on the packing density ρ of the microfluidic microsphere-trap arrays. These parameters are plotted in their feasible ranges with respect to the optimization constraints. The first derivatives of ρ with respective to l, u, b, t, and g are computed at these parameters' optimum values, obtained from the grid-search method.

less influential on ρ since ρ is less sensitive to their changes (Fig. 3.5(a), 3.5(c), and 3.5(d), respectively). ρ is independent of b (Fig. 3.5(b)). Figure 3.5 also implies that the feasible ranges of the five parameters are large enough to tolerate fabrication errors. The analysis of various geometric parameters provides insight into their relative significance, which guides us in controlling the precision of these parameters when fabricating the trap arrays.

The simulated optimal values of the geometric parameters here are used in the fabrication of the optimized microfluidic microsphere-trap array device. More details are given in the next section.

3.4 Experimental Results and Discussion

To evaluate the optimization results, we fabricated ten devices with the optimized geometric parameters obtained from the simulation. For performance comparison with the optimized devices, we also fabricated another ten devices. The geometric parameters of these ten devices were randomly selected, and satisfy only the flow resistance constraint to ensure hydrodynamic trapping (*Constraint 1*). We call these ten devices un-optimized devices for reference; though the values of their parameters may not satisfy the other proposed constraints. The geometric parameters of the optimized and un-optimized devices are listed in Table 3.2. Considering the fabrication feasibility, we constrained the parameter precision to 0.1 μm. A number of microsphere-trapping experiments was performed for each set. In these experiments both devices were tested under the same operation conditions, including driving pressure, microsphere concentration, microsphere solution viscosity, etc. Details are given below.

3.4.1 Device Fabrication

Microfluidic trap array devices were fabricated by using standard soft lithography techniques [31,35]. The devices were made of PDMS, a widely used material in microfluidics and micro-optics. Briefly, we first fabricated a patterned photoresist SU8 mold on a silicon wafer using photolithography. Then PDMS prepolymer (RTV615, 1:10 ratio) was poured onto the mold and degassed in a vacuum chamber. The prepolymer was partially cured in a 60°C oven for 45 minutes. The 45 min curing time was found to be optimal as: shorter curing time led to collapsed structures in the final device, and longer curing time made the release of PDMS from the mold difficult. The partially cured PDMS was peeled from the mold, and the liquid inlet and outlet ports were punched through the whole layer, using a biopsy punch. The PDMS layer was permanently bonded to a standard glass slide by oxygen plasma treatment.

Table 3.2: Geometric parameters of the optimized and un-optimized microfluidic microsphere-trap arrays

Values (μm)	h	r	u	b	t	g
Optimized device	13	5.2	10.1	6.9	5.2	14.6
Un-optimized device	13	14.6	27.5	5.0	17.5	12.5

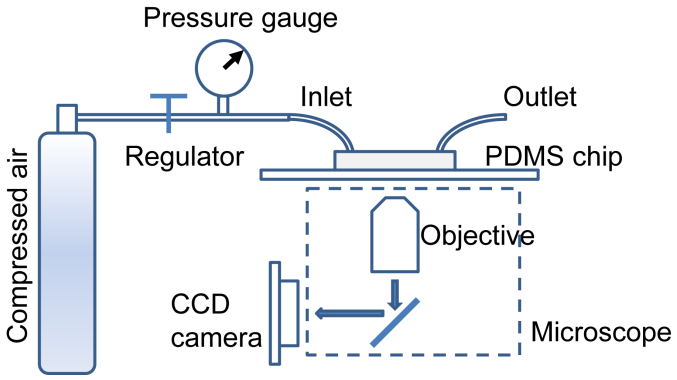

Figure 3.6: Schematic diagram of the experimental setup.

The master SU8 molds could be reused many times, thus reducing the fabrication cost and time.

3.4.2 Device Operation

The PDMS microfluidic device was mounted on an inverted microscope (Olympus IX71, San Jose, CA) equipped with an iXon+ EMCCD camera (Andor, South Windsor, CT). A solution of 10 μm polystyrene microspheres (Bangs Lab, Fishers, IN) was prepared in 1X PBS buffer with 0.05% Tween-20 (Sigma Aldrich, St. Louis, MO) at a concentration of 10^5/mL. The microsphere solution was loaded into 22 gauge Tygon tubing (Cole Parmer, Vernon Hills, IL). One end of the tubing was connected to the device input port via a stainless steel tube and the other end was connected to a pressure source controlled by a pressure regulator with a resolution of 0.4 psi. The microsphere solution was pushed into the device by applying 1-2 psi pressure to the Tygon tubing. Snapshots and videos of the microsphere trapping process were captured by the EMCCD camera. A schematic diagram of the experimental setup is shown in Fig. 3.6.

3.4.3 Results

We present the results of the microsphere-trapping experiments of the optimized and un-optimized devices. The optimization maximizes the packing density ρ of the trap arrays,

favors a single microsphere in each trap, and avoids multiple trapping and channel clogging. To compare the performances of the optimized and un-optimized devices, in addition to ρ, we define four experimental measurements as follows:

- *single*, the fraction of traps that immobilizes a single microsphere;
- *multiple*, the fraction of traps that immobilizes more than one microsphere;
- *empty*, the fraction of traps without immobilized microspheres;
- *clogged*, the fraction of channels clogged by the microspheres.

Illustrative examples of the above measurements are highlighted in Fig. 3.7(c). We expect that an optimized device should have large values for ρ and *single*, but small values for *multiple*, *empty*, and *clogged*.

From Table 3.2, we compute the areas of each trap and its surroundings for the optimized device and the un-optimized device as 694.98 μm^2 and 1312.5 μm^2. Therefore, the packing densities ρ of the two devices are 1438 traps/mm^2 and 762 traps/mm^2, respectively. Compared with the un-optimized device, the optimized one improves the packing density by a factor of two.

For a qualitative comparison of the trapping effectiveness of both devices, we present snapshots of one microsphere-trapping experiment at three critical time points: the start (Fig. 3.7(a)), middle (Fig. 3.7(b)), and end (Fig. 3.7(c)). We observe that the optimized device is remarkably more compact and neat in the layout of the trapped microspheres (larger *single*; smaller *multiple*, *empty*, and *clogged*) than the un-optimized one is. Though the optimized device requires a slightly longer time (18.67 min) to completely fill the traps than the un-optimized one does (16 min), it traps many more microspheres, virtually all of them *single*. Snapshots of the time-resolved progress of the entire trapping experiment of the two devices are available in Appendix D. Illustrative videos showing the microspheres being trapped are in [60].

To further compare the microsphere trapping performances of the optimized and un-optimized devices, we conducted five replicate experiments on each device and plotted the values of *single* as a function of time in Fig. 3.8. The *single* value of the optimized device experiences a sharp linear increase until 14 min, when over 90% of the traps are occupied correctly with a single microsphere. After this time point, the increase of *single* slows down because the still-available traps may be relatively less accessible. At the end time point, *single* of the

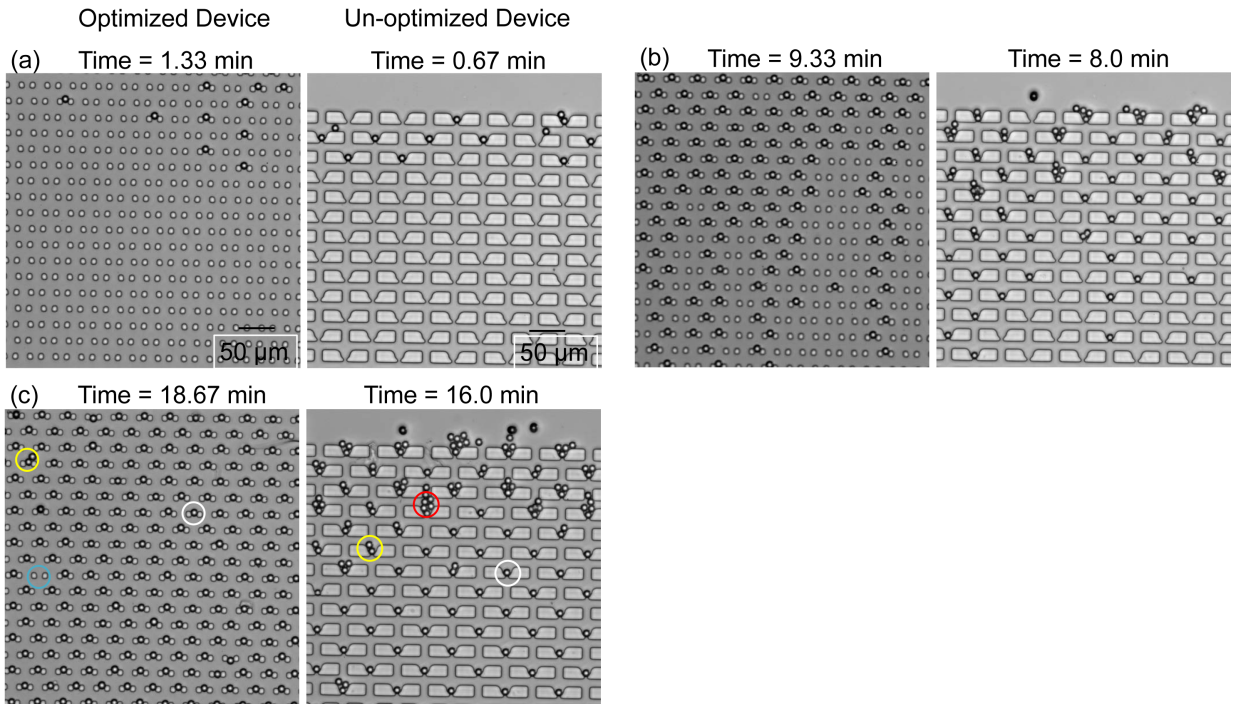

Figure 3.7: Time-lapse high-speed camera snapshots of the one microsphere-trapping experiment of an optimized device (left) and an un-optimized device (right), at (a) the start time point, (b) the middle time point, and (c) the end time point. The packing densities for the optimized and the un-optimized devices are 1390 traps/mm^2 and 762 traps/mm^2, respectively. Illustrative examples of trapping results: *single* (white circle), *multiple* (yellow circle), *empty* (blue circle), and *clogged* (red circle) are highlighted in (c). Note that due to their negligible fractions, *clogged* is not found in the snapshot of the optimized device, neither is *empty* in the snapshot of the un-optimized device.

optimized device achieves more than 99% (see Fig. 3.9 for more details). The *single* value of the un-optimized device, however, experiences a slow and concave increase almost from the beginning and reaches the limit of around 58% in the end. This figure shows that the optimized device is more efficient and accurate in trapping a single microsphere in each trap.

As an evaluation of the final outcomes of the optimized and un-optimized devices, we compute the *single*, *multiple*, *empty*, and *clogged* of ten optimized and ten un-optimized devices, at the conclusions of the experiments (such as shown in Fig. 3.7(c)). These values are presented in Fig. 3.9 and Appendix E. The small standard deviations of these measurements for both devices suggest the trapping processes are highly reproducible and the results are

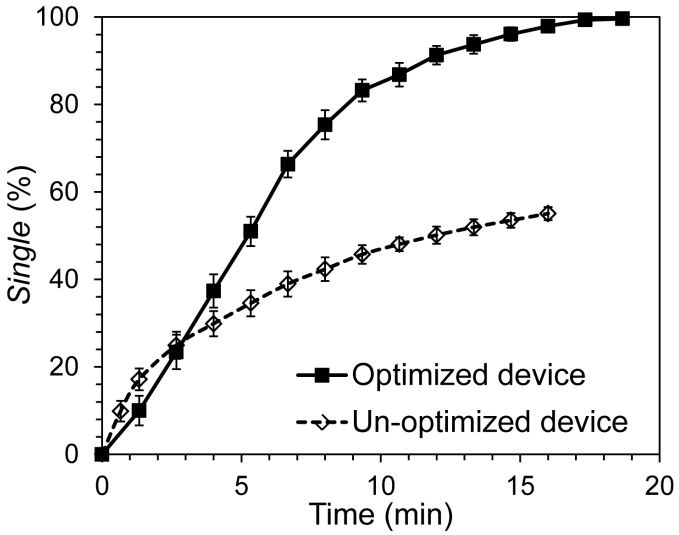

Figure 3.8: Time-lapse plots of the *single* values of the optimized device and the un-optimized device, with five replicate trapping experiments on each. Error bars indicate the standard deviations. The average experiment times needed to fill all the traps for the optimized device and the un-optimized device are 18.67 min and 16.0 min, respectively.

statistically representative. The values of *empty* are close to 0% for both devices, indicating that almost no traps remain empty in the end. As long as there exist paths for the microspheres to reach the empty traps, these traps will be eventually filled as the experiment proceeds. However, filling the empty traps runs the risk of getting more microspheres trapped at a single trap or clogging the channels. As we have observed from Figs. 3.7(c) and 3.9, the optimized device effectively avoids such risk. In other words, most of the influent microspheres in the optimized device, if not immobilized in the still-vacant traps, will pass by the channels directly. Therefore, in the optimized device, *single* is dominant (99.29%) and the undesired *multiple* and *clogged* are negligible (0.38% and 0%, respectively). On the contrary, in the un-optimized device the risk of multiple-trapping and channel clogging is obviously dramatic (Fig. 3.7(c)). That is, the influent microspheres in the un-optimized device are more likely to aggregate in the already occupied traps or channels, rather than pass through. Therefore, compared to the optimized device, *single* of the un-optimized device is much lower (58.57%), and its *multiple* and *clogged* are much higher (41.43% and 6.93%, respectively). Overall, Figure 10 confirms the effectiveness of the optimization with highly reproducible experimental results.

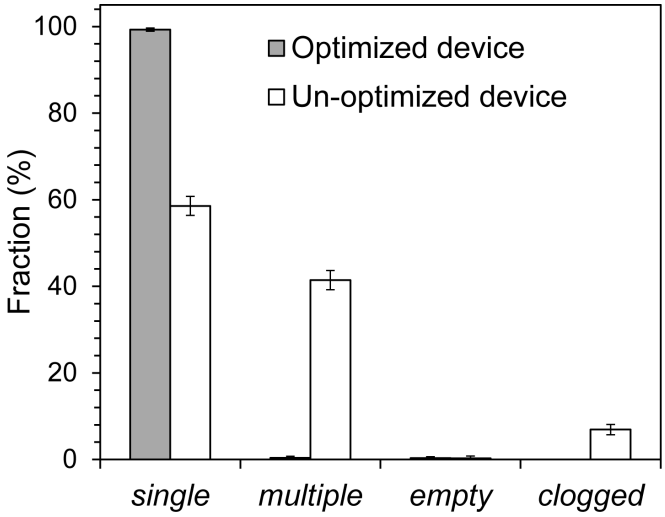

Figure 3.9: Trapping results for the optimized devices and un-optimized devices at the conclusions of the experiments. The reported values are averaged results obtained on ten devices. Error bars indicate the standard deviations of the results on ten devices.

The microsphere-trapping experiments successfully demonstrate the advantages of the optimized device over the un-optimized device. The optimized device remarkably improves the packing density and the efficiency in capturing a single microsphere at each trap. It also effectively reduces the undesirable behaviors (multiple trapping and channel clogging) in the trapping process.

The systematic optimization framework for building the optimal structure of the microfluidic microsphere-trap arrays is comprehensive and efficient. The hydrodynamic trapping mechanism employed in the optimization is accurate and effective in immobilizing the microspheres. The framework is highly robust to incorporate the specific sizes of the microspheres into the optimization problem (Eq. (3.9)). The other parameters in Eq. (3.9) are also readily modified with respect to varying requirements of device fabrication and applications. This optimization problem is simple to solve and takes less than five seconds to yield results.

It is noteworthy to mention that this work does not consider the inclusion of on-chip micromechanical valves [31], [35], [61] for simultaneously detecting targets of diverse types. However, it lays the foundation for future work in integrating statistical optimization, physical device fabrication, lab-on-a-chip instrumentation, optical imaging, and statistical analysis of data to develop the microchip device. The resulting system should simplify image analysis,

enable error-free target identification, and be highly reliable, sensitive, efficient and inexpensive. Expanded versions of the highly miniaturized arrays will be capable of processing many microarray experiments economically, and are promising for large-scale clinical applications.

3.4.4 Comparison with Self Assembled 3D Microarrays

Compared with contemporary industrial 3D microarray standards, e.g., Illumina's BeadArray systems [22], [16], our proposed microsphere arrays have several advantages, but also their own limitations. First, the microspheres in Illumina's devices are randomly ordered and require several complex steps of hybridization and dehybridization to identify their types. Our device is capable of combining micromechanical valves and isolated microfluidic chambers to trap different types of microspheres at predetermined locations, and use the locations to identify the types [12], [13]. This position encoding feature achieves simple and error-free identification. Second, Illumina's devices can identify thousands of different microspheres and thus can be applied to genotyping and gene expression profiling. However, our device is applicable only when the number of microspheres types (i.e., target types) is small or moderate. Finally, the microspheres in Illumina's devices are permanently immobilized, and thus the captured targets cannot be recovered. In our device, the microspheres are not permanently immobilized, which makes it possible to recover minute and precious captured targets after imaging, for subsequent studies or assays.

3.4.5 Comparison with Other Hydrodynamic Mechanisms

We compare here our hydrodynamic mechanism for trapping polystyrene microspheres in the proposed trap-array geometry with other mechanisms that have been recently published in the literature. In our work, we analytically optimize the trap-array to efficiently capture the microspheres in the traps, in order to use the device for sensing bio-targets. Using a laminar flow field, this optimization controls the differential flow resistance in and out of the traps to efficiently capture the microspheres in them. The concept of such analytical optimization could also be applied to other mechanisms involving various other hydrodynamic forces to separate microspheres without an externally applied field other than the flow field. The recent literature is rich in investigating such various forces as briefly highlighted below. Some

of the hydrodynamic mechanisms considered in this literature could be used in conjunction with our device in conducting efficient bio-assays, and some could be used as alternatives to our mechanism for capturing bio-targets without using any traps. In the following, we briefly summarize the relevant results in the literature.

Hou *et al.* [62] report a high-throughput and label-free microfluidic approach by exploiting particle deformation for intrinsic and non-specific removal of both microbes and inflammatory cellular components from whole blood. As blood flows through a narrow microchannel, deformable red blood cells migrate axially to the channel center, resulting in migration of other cells (bacteria, platelets, and leukocytes) towards the channel sides. These other cells are removed using smaller side channels. Whereas this study involves separating micron size species, it confines itself to filtering impurities from blood, and thus cannot be employed for our purpose.

Wang *et al.* [63] investigate the inertial effects due to vortical flow separation and the particles in such flow, and found that oscillating microbubbles driven by ultrasound can initiate a steady streaming flow around the bubbles. This flow affects the microspheres' movement, causing them to exhibit size-dependent behaviors. Adjusting the relative strengths of the streaming flow and a superimposed Poiseuille flow allows control of the spheres' flow behavior, separating the trajectories of spheres with a size resolution on the order of 1 μm. We believe that the flow mechanism described in their study has the potential to be conjugated with our device to obtain position encoding without using any microfluidic chamber.

In a study using a similar hydrodynamic mechanism, Yang *et al.* [64] propose a novel microflow cytometer in which the particles are focused in the horizontal and vertical directions by means of the Saffman shear lift force generated within a microweir microchannel. Their study shows that the microweir structures can confine a microsphere stream to the center of the microchannel without the need for a shear flow. Similar to the previous mechanism, this mechanism can also be integrated with our proposed system to automatically sort microspheres after they capture targets. We note that this is possible where microspheres of different sizes are used for capturing distinct targets.

In a similar study, Kurup *et al.* [65] demonstrate a passive, field-free, and gravitationally driven approach to perform particle concentration inside microfluidic plugs. The method requires only changing the flow velocity for efficient performance. Their work represents an

alternative approach to detecting and identifying multiple targets in a liquid sample, using functionalized microspheres without employing any microfluidic trapping mechanism.

To summarize, we believe that our proposed analytical optimization method applies to a state-of-the-art hydrodynamic mechanism based on laminar flow in a microsphere trap-array geometry. It complements very well the recently investigated hydrodynamic mechanisms studied using cutting-edge microfluidic techniques. These two directions could be combined in future research, for efficiently sorting, detecting, and identifying micron-size species in a liquid sample.

3.5 Summary

In this chapter, we provided a novel geometric structure of a microfluidic microsphere-trap array device and employed fluidic resistance to hydrodynamically trap the microspheres. We built a comprehensive, robust, and simple framework to optimize the geometry of the trap arrays to maximize the packing density, while simultaneously satisfying other criteria. These criteria include efficiently immobilizing the microspheres (i.e., trapping a single microsphere in each trap stably and avoiding multiple trapping and channel clogging), and minimizing the error in imaging the target captured microspheres in subsequent studies. Microsphere-trapping experiments confirmed that the performance of the optimized device was significantly improved with respect to the optimization goal and criteria, compared with the un-optimized device.

In this chapter, we also employed finite element (FEM) fluid dynamics simulations to validate the hydrodynamic trapping mechanism in our trap arrays. In the next chapter, we provide a step-by-step formulation of a FEM model for the device and apply the model to investigate the hydrodynamic trapping of the microspheres. In Chapter 5, we extend our analytical framework to build a optimized microfluidic microsphere-trap array device that enables simultaneous, efficient, and accurate screening of multiple biological targets in a single microfluidic channel.

Chapter 4

Finite Element Simulations of Hydrodynamic Trapping in Microfluidic Microsphere-Trap Arrays[3]

In the previous chapter, we designed and implemented position-encoded microsphere arrays, integrated with microfluidic technology (microfluidic microsphere-trap arrays). We further formulated an analytical framework to optimize the geometry of the microfluidic microsphere-trap arrays for maximized packing density, optimized trapping efficiency, and minimized fluidic errors. We employed finite element (FEM) fluid dynamics simulations to validate the hydrodynamic trapping mechanism in our trap arrays. In this chapter, we provide a step-by-step formulation of a FEM model for our device and apply the model to investigate the hydrodynamic trapping of the microspheres. This FEM model can be tailored to similar microfluidic systems that may accommodate a variety of structured particles and can help guide microfluidic system design and experimental operation.

[3]Based on X. Xu, Z. Li, and A. Nehorai, "Finite element simulations of hydrodynamic trapping in microfluidic particle-trap array systems", *Biomicrofluidics*, vol. 7, 054108, Sep. 2013.

4.1 Introduction

In recent years, microfluidic systems have received great interest in life science, biochemistry, pharmacology, and medical diagnostics [66], [67], [68]. By miniaturizing and integrating diverse functionalities, microfluidic systems provide the ability to perform laboratory operations on small scales (i.e., lab-on-a-chip devices). They can synthesize and analyze small volumes of sample, minimize reagent consumption, integrate high-throughput sample processing steps, and reduce processing time, all of which provide great promise for both fundamental research and practical applications. Most microfluidic systems involve complex mixtures of biological particles, such as functionalized microspheres or colloids [69], [70], and cell suspensions [71]. Applications of these microfluidic systems include biomolecule detection and profiling [19], [72], microsphere-based micromixing and immunoassays [73], [74], and cell sorting and separation [75], [76]. For example, the experiments on sorting, separating, and trapping CTCs have been performed using microfluidic systems with similar hydrodynamically engineered configurations [77], [78], [79]. To optimize the functionalities of these systems, one needs to understand the hydrodynamic behavior of the particles so as to manipulate them in a controlled manner. In [27], Karimi *et al.* briefly reviewed the hydrodynamic mechanisms of cell and particle trapping. However, microfluidic devices are not simply scaled-down versions of conventional macro-scale systems. Because the dimensions of a microfluidic structure are small, particles suspended in a fluid become comparable in size to the structure itself, which dramatically alters the system's behaviors. As a result, the fluidic dynamics are rather complicated and are affected by many parameters, e.g., the fluid's viscosity, velocity, and pressure; the device geometry; the particle number, shape, and elastic flexibility (specially for blood cells or emulsions); and fluid-particle interactions. The interactive complexity of these parameters often prevents a holistic understanding of the systems, making it difficult to achieve reliable designs and effective experimental operation.

To study microfluidic systems, computational fluid dynamic (CFD) simulations coupled with solid mechanics have become an increasingly important tool. By incorporating the complexities of the system's parameters, the microfluidic system's hydrodynamic behavior can be predicted and visualized, even though the system's minute dimensions make that behavior difficult (but not impossible) to prove via explicit mathematical methods or experiments. Therefore, the simulations help researchers assess design alternatives at reduced cost and

guide experimental operation [28], [29]. For our microfluidic microsphere-trap arrays as an example, microspheres with receptors on their surfaces to capture biological targets (DNAs, RNAs, or proteins) are immobilized by the trap arrays through microfluidic techniques. The trap array geometry must be rationally designed to maximize the trapping efficiency of microspheres and minimize fluidic errors. The importance of hydrodynamic properties in the successful trapping of the microspheres, demonstrated in Chapter 3 [80], highlighted the value of CFD simulations in predicting and investigating the movement of microspheres in the microfluidic device.

To address this need, in this chapter we create a finite element (FEM) [81] simulation model to study the hydrodynamic trapping of microspheres in our device [80]. To our knowledge, no similar systems have been simulated before. Therefore, our simulation will be a significant addition to the existing toolbox on the theoretical design and understanding of increasingly complex hydrodynamically engineered microfluidic systems. A time-dependent simulation of a microsphere's trapping process shows excellent agreement with the experimental observation, which benchmarks the microfluidic device. Based on the simulation, we investigate the fluid velocity field, pressure field, and force and stress on the microsphere in the device. We further explore the trap's geometric parameters and the critical fluid velocity, above which subsequent microspheres will not bypass the already-filled trap but will collide with it. Selecting appropriate geometric parameters and obtaining the critical fluid velocity are helpful to ensure efficient trapping of microspheres and reduce potential fluidic errors in the device.

While we employ the FEM simulation to study the hydrodynamic trapping of microspheres in our device, one can tailor and customize it for similar microfluidic systems with complex structures and different particles. We implement the simulation in COMSOL Multiphysics [59] and release it on our website, accessible by following the link in [82]. The simulation set-up discussed in this chapter also provides guidelines to help future users to tailor the model to their specific problems.

This chapter is organized as follows. In Section 4.2, we outline the theoretical fundamentals of the simulation model. In Section 4.3, we briefly review the configuration of the microfluidic microsphere-trap array device. Then, we discuss the simulation set-up in detail. In Section 4.4, we compare the simulated trapping process for one microsphere with our experimental

Table 4.1: Input parameters and output variables for the simulation model

Input parameters
Geometry of the microfluidic device (e.g., device length L (m), width W (m), height H (m))
Location and geometry of obstacles in the device, if any
Location, release method, and shape of the particles (e.g., spherical particle radius r (m))
Properties of the fluid (e.g., fluid density ρ_f (kg/m^3), dynamic viscosity μ_f (Pa·s), volume force affecting the fluid $\boldsymbol{F}_\mathrm{f}$ (N/m^3))
Properties of the particles (e.g., particle density ρ_s (kg/m^3), Young's Modulus E_s (Pa), Poisson ratio R_s)
Inlet and outlet conditions (e.g., velocity (m/s), pressure (Pa), stress (N/m^2), or mass flow (kg/s))
Boundary conditions of device sidewalls and obstacles (e.g., no-slip wall)
Initial conditions of the fluid and the particles
Properties of mesh (scale and size Δx)
Computation set-up (e.g., time range (s), time step size Δt (s), relative tolerance, solver type, etc.)
Basic output variables, from which other variables of interest can be computed
Fluid velocity field $\boldsymbol{u}_\mathrm{f} = (u_\mathrm{f}, v_\mathrm{f}, w_\mathrm{f})$ (m/s, m/s, m/s)
Fluid pressure p_f (Pa)
Particle displacement field $\boldsymbol{u}_\mathrm{s} = (u_\mathrm{s}, v_\mathrm{s} w_\mathrm{s})$ (m, m, m)
Particle infinitesimal strain tensor $\boldsymbol{\epsilon}_\mathrm{s}$
Particle Cauchy stress tensor $\boldsymbol{\sigma}_\mathrm{s}$
Volume force affecting the particle F_s (N/m^3)
Coordinates of the spatial frame x, y, z
Coordinates of the material frame X, Y, Z

results, in terms of the microsphere's displacement over time. For the fluid, we present its velocity and pressure fields. For the microsphere, we compute its velocity and the total force acting on it. We also show the stress on and deformation of the microsphere. We further explore the trap's geometric parameters and fluid velocities, which affect the microsphere's motion towards the trap. At the end of this section, the merits and limitations of the model are discussed. Section 4.5 summarizes the chapter.

4.2 Theoretical Fundamentals

The conceptual principles of the simulation model for the microfluidic system are straightforward. In this system, the fluid flow is described by the Navier-Stokes equations [52], and the particles (e.g., microspheres) obey linear elastodynamics and Newton's equation of motion [83]. The coupling of fluid flow and solid mechanics is implemented by fluid-solid interaction, where the fluid imposes force on the particles' surfaces from fluid pressure and

viscous drag. The finite element method (FEM) [81] is employed to create a mesh of the simulation domain and discretize governing equations for solutions. Due to the movements and interactions of the fluid and particles, the mesh geometry is continuously moving and deformed. The arbitrary Lagrangian-Eulerian (ALE) technique [84] is further employed to describe the dynamics of the deforming geometry and moving boundaries of the mesh, which helps create a new mesh and maintains numerical stability and accuracy. Table 4.1 summarizes required and changeable input parameters and output variables in the simulation model. Detailed equations are presented next.

4.2.1 Fluid Flow

The fluid flow in microfluidic systems, if assumed incompressible, is described by the Navier-Stokes equations [52]:

$$\rho_{\mathrm{f}}\frac{\partial \boldsymbol{u}_{\mathrm{f}}}{\partial t} + \rho_{\mathrm{f}}(\boldsymbol{u}_{\mathrm{f}} \cdot \nabla)\boldsymbol{u}_{\mathrm{f}} = \nabla \cdot [-p_{\mathrm{f}}\boldsymbol{I} + \mu_{\mathrm{f}}(\nabla \boldsymbol{u}_{\mathrm{f}} + (\nabla \boldsymbol{u}_{\mathrm{f}})^T)] + \boldsymbol{F}_{\mathrm{f}}, \tag{4.1}$$

$$\rho_{\mathrm{f}}\nabla \cdot \boldsymbol{u}_{\mathrm{f}} = 0, \tag{4.2}$$

where ρ_{f} denotes the fluid density (kg/m^3), $\boldsymbol{u}_{\mathrm{f}} = (u_{\mathrm{f}}, v_{\mathrm{f}}, w_{\mathrm{f}})$ the fluid velocity field (m/s, m/s, m/s), t the time (s), p_{f} the pressure (Pa), $\nabla \cdot ()$ the divergence operator, $\nabla()$ the gradient operator, $\boldsymbol{I}$ the identity matrix, and μ_{f} the fluid dynamic viscosity (Pa·s). Moreover, $\rho_{\mathrm{f}}\frac{\partial \boldsymbol{u}_{\mathrm{f}}}{\partial t}$ represents the unsteady inertia force (N/m^3), $\rho_{\mathrm{f}}(\boldsymbol{u}_{\mathrm{f}} \cdot \nabla)\boldsymbol{u}_{\mathrm{f}}$ represents the non-linear inertia force, and $\boldsymbol{F}_{\mathrm{f}}$ is the volume force affecting the fluid (N/m^3, or N/m^2 for a 2D model). For a pressure-driven flow without gravitation or other volume forces, $\boldsymbol{F}_{\mathrm{f}} = \boldsymbol{0}$. Given the values of ρ_{f}, t, μ_{f}, and $\boldsymbol{F}_{\mathrm{f}}$, the Navier-Stokes equations solve for $\boldsymbol{u}_{\mathrm{f}}$ and p_{f}.

Due to the high computational demand of three dimensional (3D) fluid dynamics simulation, two dimensional (2D) simulation is preferred. For microfluidic channels with an almost rectangular cross section, where the thickness is much less than the channels' width, simple 2D models often fail to give correct results because they exclude the boundaries, which have a great effect on the flow. To consider the effect of these boundaries, shallow channel approximation is proposed [52]. The approximation adds a drag term as a volume force to the fluid flow equation, which represents the resistance that the parallel boundaries place on

the flow. The form of the drag term is

$$\boldsymbol{F}_{\mu} = -12\frac{\mu_{\mathrm{f}}\boldsymbol{u}_{\mathrm{f}}}{H^2}, \tag{4.3}$$

where H is the channel thickness (m).

Because of the microfluidic system's small dimensions and fluid velocities, the Reynolds number $Re = lU\rho_{\mathrm{f}}/\mu_{\mathrm{f}}$ (l is the characteristic length and U is the average velocity) of the flow is small ($Re \ll 100$). Thus the flow stays laminar over most of the area [52]. When the velocities of the fluid are very small, Re becomes very low ($Re \ll 1$). The Strouhal number $St = Fl/U$ (F is the frequency of vortex shedding) is large (on the order of 1), and viscosity dominates the fluid flow, resulting in a collective oscillating movement of the fluid. Under this circumstance, flow in the system becomes Stokes flow (also called creeping flow), and the unsteady inertia force greatly dominates over the non-linear inertial force. Therefore, the non-linear inertial force $\rho_{\mathrm{f}}(\boldsymbol{u}_{\mathrm{f}} \cdot \nabla)\boldsymbol{u}_{\mathrm{f}}$ can be neglected. Combining the shallow channel and Stokes flow approximations with the incompressible Navier-Stokes equations, Eq. (4.1) becomes

$$\rho_{\mathrm{f}}\frac{\partial \boldsymbol{u}_{\mathrm{f}}}{\partial t} = \nabla \cdot [-p_{\mathrm{f}}\boldsymbol{I} + \mu_{\mathrm{f}}(\nabla \boldsymbol{u}_{\mathrm{f}} + (\nabla \boldsymbol{u}_{\mathrm{f}})^T)] - 12\frac{\mu_{\mathrm{f}}\boldsymbol{u}_{\mathrm{f}}}{H^2} + \boldsymbol{F}_{\mathrm{f}}. \tag{4.4}$$

4.2.2 Solid Mechanics

The solid, if assumed to undergo only small deformation and be subjected to low load, has isotropic linear elasticity. The displacement and deformation of the solid satisfy the governing equations of linear elastodynamics [83]:

$$\boldsymbol{\epsilon}_{\mathrm{s}} = \frac{1}{2}[(\nabla \boldsymbol{u}_{\mathrm{s}})^T + \nabla \boldsymbol{u}_{\mathrm{s}} + (\nabla \boldsymbol{u}_{\mathrm{s}})^T(\nabla \boldsymbol{u}_{\mathrm{s}})], \tag{4.5}$$

$$\nabla \cdot \boldsymbol{\sigma}_{\mathrm{s}} + \boldsymbol{F}_{\mathrm{s}} = \rho_{\mathrm{s}}\frac{\partial^2 \boldsymbol{u}_{\mathrm{s}}}{\partial^2 t}, \tag{4.6}$$

$$\boldsymbol{\sigma}_{\mathrm{s}} = \boldsymbol{C}\boldsymbol{\epsilon}_{\mathrm{s}}. \tag{4.7}$$

Here, Eq. (4.5) is the strain-displacement (compatibility) equation, with $\boldsymbol{\epsilon}_{\mathrm{s}}$ denoting the infinitesimal strain tensor and $\boldsymbol{u}_{\mathrm{s}} = (u_{\mathrm{s}}, v_{\mathrm{s}}w_{\mathrm{s}})$ denoting the solid displacement field (m, m, m). Eq. (4.6) is Newton's equation of motion, with $\boldsymbol{\sigma}_{\mathrm{s}}$ the Cauchy stress tensor, $\boldsymbol{F}_{\mathrm{s}}$ the

body force per unit volume (N/m^3) or boundary force per unit area in 2D (N/m^2), and ρ_s denoting the solid density (kg/m^3). Eq. (4.7) is the linear elastic stress-strain law, with $\boldsymbol{C}$ as the stiffness matrix given by

$$\boldsymbol{C} = \frac{E_\mathrm{s}}{(1+R_\mathrm{s})(1-2R_\mathrm{s})} \begin{bmatrix} 1-R_\mathrm{s} & R_\mathrm{s} & R_\mathrm{s} & 0 & 0 & 0 \\ R_\mathrm{s} & 1-R_\mathrm{s} & R_\mathrm{s} & 0 & 0 & 0 \\ R_\mathrm{s} & R_\mathrm{s} & 1-R_\mathrm{s} & 0 & 0 & 0 \\ 0 & 0 & 0 & 1-2R_\mathrm{s} & 0 & 0 \\ 0 & 0 & 0 & 0 & 1-2R_\mathrm{s} & 0 \\ 0 & 0 & 0 & 0 & 0 & 1-2R_\mathrm{s} \end{bmatrix}, \tag{4.8}$$

where E_s is Young's modulus of the solid (Pa), and R_s is the Poisson ratio of the solid.

Given the values of ρ_s, t, $\boldsymbol{F}_\mathrm{s}$, E_s, and R_s, Eqs. (4.5)-(4.8) solve for $\boldsymbol{u}_\mathrm{s}$, $\boldsymbol{\epsilon}_\mathrm{s}$, and $\boldsymbol{\sigma}_\mathrm{s}$.

4.2.3 Fluid-solid Interaction (FSI)

The FSI couples fluid flow with solid mechanics to capture the interaction between the fluid and the solid, which is applied through their boundary. It defines the fluid load on the solid and how the solid displacement affects the fluid's velocity:

$$\boldsymbol{f}_\mathrm{s} = -\boldsymbol{n} \cdot [-p_\mathrm{f}\boldsymbol{I} + \mu_\mathrm{f}(\nabla \boldsymbol{u}_\mathrm{f} + (\nabla \boldsymbol{u}_\mathrm{f})^T)], \tag{4.9}$$

$$\boldsymbol{u}_\mathrm{W} = \frac{\partial \boldsymbol{u}_\mathrm{s}}{\partial t}, \quad \boldsymbol{u}_\mathrm{f} = \boldsymbol{u}_\mathrm{W}, \tag{4.10}$$

where Eq. (4.9) presents the total force (caused by the fluid pressure and viscous force) exerted on the solid boundary, and $\boldsymbol{n}$ is the outward normal to the boundary. From Eq. (4.10), on the fluid-solid boundary the fluid velocity $\boldsymbol{u}_\mathrm{f}$ equals the rate of change for the displacement of the solid $\boldsymbol{u}_\mathrm{W}$. In other words, the solid boundary acts as a no-slip wall for the fluid domain.

FEM [81] is employed to create a mesh of the simulation domain and discretize the governing Eqs. (4.1)-(4.10), so as to approximate the solutions within a mesh element using simple functions. For a time-dependent problem, the Navier-Stokes equations of the fluid flow are solved using an Eulerian description and a spatial frame. Explicitly, the mesh in the fluid

domain is freely moving, with an initial mesh displacement of zero. With each moving mesh element, a smoothing function is associated and leads to effective forces between neighboring elements, resulting in substantial redistribution and deformation of the whole configuration of the mesh. The solid mechanics are formulated using a Lagrangian description and a material (reference) frame. That is, the mesh in the solid domain is fixed and undeformed [84]. Therefore, the force $\boldsymbol{F}_\mathrm{s}$ on the solid is a transformation of $\boldsymbol{f}_\mathrm{s}$:

$$\boldsymbol{F}_\mathrm{s} = \boldsymbol{f}_\mathrm{s} \frac{\mathrm{d}v}{\mathrm{d}V}, \tag{4.11}$$

where $\mathrm{d}v$ and $\mathrm{d}V$ are the mesh element scale factors for the spatial frame and the material frame, respectively.

To combine the interface between the spatial frame of the fluid and the material frame of the solid, the arbitrary Lagrangian-Eulerian (ALE) method is employed [84], which computes new mesh coordinates based on both the movement of the solid's boundary and mesh smoothing of the fluid.

4.2.4 Boundary and Initial Conditions

The fluid flows from the channel inlet to the outlet, driven by the pressure difference between the inlet and the outlet. At the inlet, the flow is defined to have fully developed laminar characteristics with a parabolic velocity profile and mean velocity u_0 (m/s). By defining a parabolic velocity profile instead of a constant velocity, one ensures a better convergence of the nonlinear solver at the beginning. A simple definition of the inflow velocity profile U_0 for a rectangular channel is [52]

$$U_0 = u_0 \cdot \frac{6(W - Y)Y}{W^2}, \tag{4.12}$$

where W is the width of the inlet, and Y is the material frame coordinate along the inlet.

At the outlet, the boundary condition is defined as vanishing viscous stress along with a Dirichlet condition on the pressure:

$$p_\mathrm{f} = 0, \quad \mu_\mathrm{f}(\nabla \boldsymbol{u}_\mathrm{f} + (\nabla \boldsymbol{u}_\mathrm{f})^T)\boldsymbol{n} = \boldsymbol{0}. \tag{4.13}$$

On the solid walls, such as the simulation domain sidewalls and fixed obstacles (e.g., traps in our particle-trap array device), no-slip wall condition is applied to the fluid:

$$\boldsymbol{u}_{\mathrm{f}} = \mathbf{0}, \tag{4.14}$$

and the prescribed mesh displacements of these walls are defined as zero.

For the initial values of the fluid velocity field $\boldsymbol{u}_{\mathrm{f}}$, pressure p_{f}, particle displacement field $\boldsymbol{u}_{\mathrm{s}}$, and particle velocity field $\partial \boldsymbol{u}_{\mathrm{s}}/\partial t$, one can assign specific values if there are good estimations. Otherwise, one can set them as zeros for simplicity.

4.3 From Design to Simulation

We apply the finite element simulation to our microfluidic microsphere-trap array device design and validation [80], [85]. We also investigate the set-up requirements of the simulation, including the selection of mesh scales, moving mesh conditions, time step size, solver types, etc.

4.3.1 Configuration of the Microfluidic Microsphere-trap Array Device

Figure 4.1 presents a schematic diagram of the microfluidic microsphere-trap array device. The microfluidic channel has an inlet on the left side and an outlet on the right side. The traps in the channel are made of polydimethylsiloxane (PDMS), with each trap shaped as inverted-trapezoid grooves. The trap arrays are periodic, with each row offset horizontally with respect to the one ahead of it. A liquid solution (water) carrying polystyrene microspheres of radius $r = 5$ μm flows from the inlet and through the channel. We note that the microspheres are the only 'solid' to be considered in the equations of the solid mechanics and the fluid-solid interaction described in the previous section, while the traps are assumed to be fixed and act as the no-slip boundary to the fluid. In a simulation, one usually can shorten the length and the width of the channel with respect to the real device to reduce the computation,

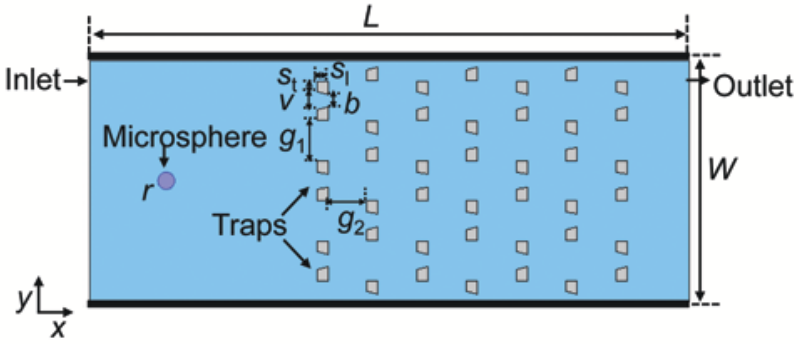

Figure 4.1: Schematic diagram of a microfluidic microsphere-trap array device. The microfluidic channel has an inlet on the left side and an outlet on the right side. The traps in the channel are made of polydimethylsiloxane (PDMS), with each trap shaped as inverted-trapezoid grooves. The trap arrays are periodic, with each row offset horizontally with respect to the one ahead of it. A liquid solution carrying a polystyrene microsphere of radius 5 μm flows from the inlet and through the channel. The values of the device's geometric parameters are given in Table 4.2.

without changing its hydrodynamic characteristics. One also can make other appropriate simplifications of the experimental situation. As the inlet effectively injects single or several microspheres into the channel at a time, the inflow of microspheres can be emulated in the simulation by a generic source of microspheres placed at a certain distance away from the traps. The geometric parameters of the trap array device [85] and the present simulation parameters are given in Table 4.2.

4.3.2 Assessment of the Simulation

The flow through the device (Fig. 4.1) is characterized by the Reynolds number ($Re = lU\rho_f/\mu_f$). In our case, the characteristic length l is the microsphere's diameter $2r$, and U is the relative velocity between the steady state flow and the microsphere. Therefore, when the relative velocity $\ll$10 cm/s and $Re \ll 1$, the system can be treated at the asymptotic limit of Stokes flow [52].

Table 4.2: Present simulation parameters

L (channel length)	360 μm
W (channel width)	140 μm
H (channel height)	20 μm
v (upper width of trap opening)	10 μm
b (bottom width of trap opening)	7.6 μm
s_{t} (upper width of groove walls)	6.6 μm
s_{l} (length of groove walls)	6.6 μm
h (height of groove walls)	16.5 μm
g_1 (gap between two neighboring traps on the same row)	23.3 μm
g_2 (gap between two successive row)	23.3 μm
r	5 μm
ρ_{f}	1,000 kg/m^3
μ_{f}	0.001 Pa·s
u_0	70 μm/s
ρ_{s}	1,050 kg/m^3
E_{s}	3 MPa
R_{s}	0.33
Δt	0.001 s

As for the thermal motion (Brownian motion), its relative importance can be characterized by the Peclet number Pe [86]:

$$Pe = UL/D_{\mathrm{diff}}, \quad D_{\mathrm{diff}} = K_{\mathrm{B}}T/6\pi\mu_{\mathrm{f}}r, \tag{4.15}$$

where U (m/s) is the velocity of the microsphere, L (m) is a typical distance that the microsphere can travel (say, the distance from the inlet to outlet of the microfluidic channel), D_{diff} is the Einstein expression for the diffusion coefficient of a spherical particle of radius r (m/s), K_{B} is the Boltzmann constant, and T (K) is the experiment temperature. In our case, Pe is much larger than 1. Thus, the thermal motion of the microsphere is negligible [86], and is not considered in our simulation.

4.3.3 Mesh Creation, Smoothing, Independence Test, and Remeshing

As we mentioned in Section 4.2, to solve the governing equations, FEM is employed to create a mesh of the simulation domain and to discretize the equations. The ALE technique

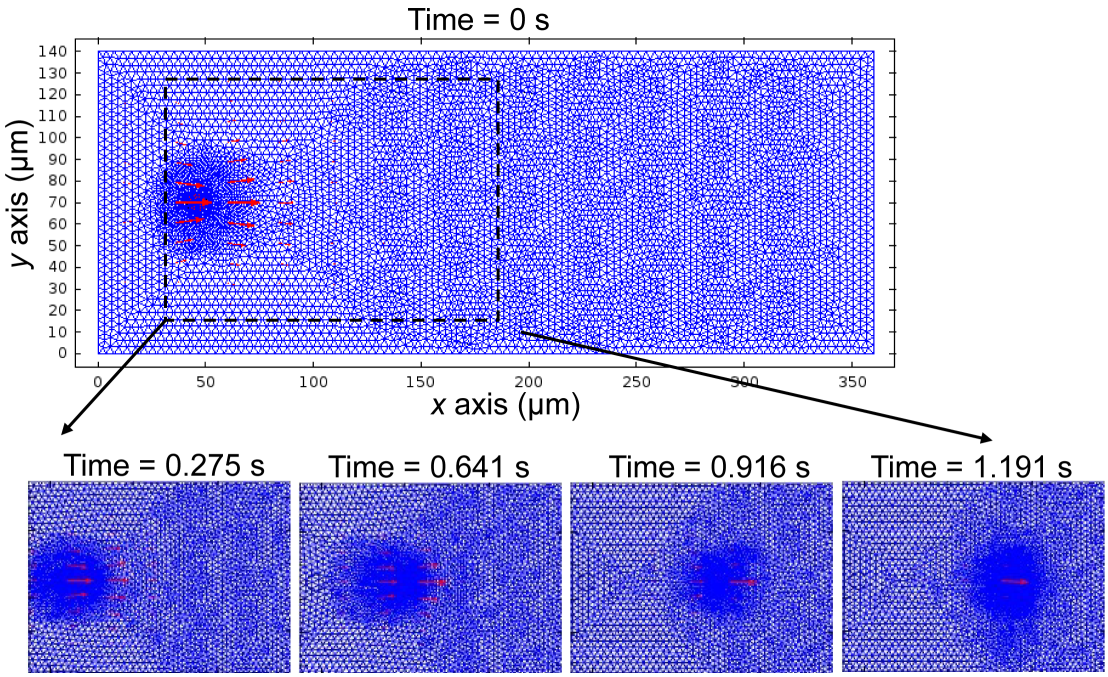

Figure 4.2: Mesh and geometry movement and deformation at a series of time points: initial mesh (full-size plot) at $t = 0$ s, and deformed mesh (zoomed-in plots) at $t = 0.275$ s, 0.641 s, 0.916 s, and 1.191 s. The microsphere is shown in red, which is underneath the densest meshes in each plot. The arrows represent the mesh direction and velocity, with their sizes indicating the velocity magnitude.

is used to describe the interface between the fluid and the microsphere. During the time-dependent solution process, the mesh in the microsphere domain is fixed and undeformed, while the mesh in the fluid domain is freely moving and deformed in response to mesh smoothing and the movement of the microsphere. For the mesh smoothing function, Winslow smoothing or hyperelastic smoothing is recommended [87], [88]. Both smoothing methods are nonlinear and robust, and work well for our problem. The hyperelastic method can give a smoother result than Winslow does, particularly in regions where the mesh is highly stretched. Therefore, when the solid particle has large elasticity (e.g., a blood cell) with large deformation expected, the hyperelastic method is more suitable.

Figure 4.2 presents the initial mesh (with free triangular shape) at $t = 0$ s, which is generated prior to solving the model. Though the mesh is not uniform, with denser and smaller elements at the fluid-solid boundaries and looser and larger elements in the fluid domain, the mesh is equally distributed around the microsphere. Figure 4.2 also illustrates how the mesh moves

Table 4.3: Mesh scales in mesh independence study

Mesh scale	Maximum element size (μm)	Minimum element size (μm)	Maximum element growth rate	Resolution of curvature	Number of elements	Degrees of freedom
Extremely fine	0.938	0.028	1.05	0.25	167,324	408,559
Extra fine	1.82	0.21	1.08	0.25	46,780	114,918
Finer	3.92	0.56	1.1	0.25	12,214	30,759
Fine	4.9	1.4	1.13	0.3	9,708	24,299
Normal	6.3	2.8	1.15	0.3	7,629	18,794
Coarse	9.28	4.2	1.2	0.4	2,942	7,518

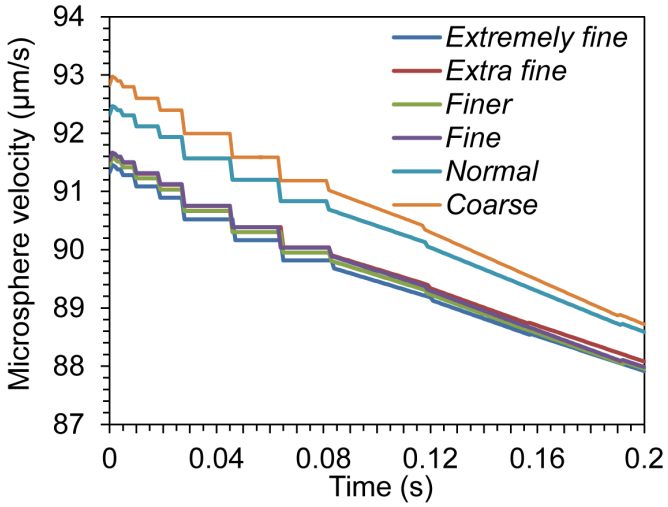

Figure 4.3: Time-dependent plots of the microsphere's velocity along the x direction at different mesh scales.

with a continuously deforming geometry at a series of subsequent time points t = 0.275 s, 0.641 s, 0.916 s, and 1.191 s. Because the microsphere is moving along the x direction, the mesh is also moving in this direction (shown by the red arrows in the figure).

As exact analytical solutions to the equations are unknown, a mesh independence test can be used to choose an appropriate mesh size. It is performed by increasing the mesh size (denoted as mesh scale) until the difference between the results for two successive mesh scales is negligible. Table 4.3 presents the properties of different mesh scales and the degrees of freedom in solving the equations. Figure 4.3 plots the velocity of the microsphere at $t = 0$ s$\sim$0.2 s under different mesh scales. It can be seen that the differences among the velocities for the mesh scales *fine*, *finer*, *extra fine*, and *extremely fine* (as defined in Table 4.3) are

very small. Considering computational efficiency and to reduce the chance that the solver might not converge at an extreme, the scale *finer* is used for subsequent simulation.

When the mesh deformation of ALE becomes large (in our case when the microsphere draws near to the trap), the quality of the mesh created by the smoothing function deteriorates and the mesh elements may be (partially) warped inside-out (inverted coordinates). Inverted coordinates do not mean a failure of the simulation, but they do imply that results at these elements will not be used in further iterations. If these elements are not in the vicinity of the area of interest, the simulation is still expected to be reliable. However, if there are many inverted coordinates, the accuracy of the solution is reduced and the solver runs into convergence problems. To solve this issue, a new mesh can be generated for the region covered by the deformed mesh, and then letting the solver continue by deforming the new mesh. Explicitly, we define a requested mesh quality (as a scalar number between 0 and 1, typically smaller than 0.2). When the mesh quality becomes smaller than the requested one, the solver stops and remeshes at a previously stored solution time. Then the simulation continues using the new mesh from this solution time.

4.3.4 Selection of Time Step Size

The time step size Δt (s) affects the numerical stability, accuracy, and efficiency of the computation. The selection of Δt can be quite complex, and here we provide only guidelines. First of all, an appropriate Δt should satisfy the necessary Courant-Friedrichs-Lewy (CFL) condition ($U\Delta t/\Delta x \ll 1$), where U (m/s) is the velocity and Δx (m) is the mesh size [89], [90]. Then one can use a single Δt for the simulation time. However, this may result in a too small Δt and an inefficient computation. Alternatively, one can use a Δt that meets the local CFL condition. In such an arrangement, most of the computation is concentrated in simulation time ranges with the finest mesh and largest mesh deformation. In the time ranges of coarse mesh and small mesh deformation, the solution is updated only occasionally, with a much larger Δt.

4.3.5 Selection of Solvers

To solve the time-dependent simulation problem, we consider two solution approaches, fully coupled or segregated. For the fully coupled solver, the multiple physics from Eqs. (4.1)-(4.14) are coupled together. Thus the fluid velocity and pressure, as well as the microsphere motion, stress, and strain, are solved at the same time. For the segregated solver, the solution process is split into several steps. Explicitly, for a current microsphere position, the fluid flow is solved using the velocities at the microsphere surface from the previous step, which used the fluid-solid interaction boundary condition Eq. (4.10) and fluid flow Eqs. (4.1)-(4.4). Then the total force, which includes viscous and pressure terms from the fluid, is evaluated at the microsphere surface (Eqs. (4.9) and (4.11)). The force is further used in Eqs. (4.5)-(4.8) for defining the microsphere's motion and deformation. In our case, we observe that the segregated solver takes far more computational time than the fully coupled solver does, and its estimated error of solution (on the order of 10^6) is also much larger than that of the fully coupled one (on the order of 10). Therefore, the fully coupled solver is employed. Moreover, we choose a damped version of Newton's method for the solver, and let the solver automatically determine the damping factor in each iteration [91].

4.4 Simulation Results, Validation, and Discussion

In this section, we present the simulation results of the hydrodynamic trapping in the microfluidic microsphere-trap array device. First, to validate the accuracy of the simulation, we perform a microsphere trapping experiment using the device and compare the experimental results with the simulation in terms of the microsphere's displacement over time. Then we investigate the simulation results of some variables that are difficult to measure experimentally in the trapping process. For the fluid, we provide its velocity and pressure fields. For the microsphere, we compute its velocity and the total force on it. We also show the stress on and deformation of the microsphere. We further explore the trap's geometric parameters and the critical fluid velocity, above which the subsequent microspheres would collide with, instead of bypassing, a trap that is already filled by a microsphere. Finally, the merits and limitations of the model are discussed.

4.4.1 Flow Velocity Field and Microsphere Displacement: Simulation versus Experiment

Figure 4.4 presents the simulated flow velocity field at a series of time points (full size plot at $t = 0$ s, and zoomed-in plots at $t = 0.275$ s, 0.641 s, 0.916 s, and 1.191 s). The streamlines indicate the flow direction, and the rainbow color represents the flow-velocity magnitude distribution, with a fixed value range for all plots. We observe that the flow moves faster through the gaps among the traps, and slower through the traps due to the traps' small openings. The flow's velocity is zero at the boundaries of the traps. The streamlines clearly show that there are no vortices in the creeping flow. Moreover, only the flow in close proximity to the microsphere is affected by the microsphere's motion. Once a trap is filled by the microsphere, the flow is blocked at the trap.

Figure 4.4(a) also shows the positions of a microsphere at the different time points in the experiment and the simulation. Figure 4.4(b) further compares the time-dependent displacements of the microsphere along the x direction in the experiment and in the simulation. The displacement of the microsphere increases almost linearly and finally stays constant when the microsphere becomes immobilized in the trap. The simulation results agree well with the experiment. Two video recordings of the experiment and of the simulation of the microsphere's trapping process ($t = 0$ s$\sim$2.02 s) are provided in [92].

4.4.2 Microsphere Velocity and Total Experienced Force

Figure 4.5 presents time-dependent plots of the microsphere's velocity (4.5(a)) and experienced total force (4.5(b)) along the x direction. At the beginning, when the microsphere is far away from the trap, it has almost the same velocity as that of the surrounding steady-state fluid, and thus experiences little force from the fluid. As the microsphere flows toward the trap, the velocity of the fluid ahead decreases because of the trap in path, and exerts negative drag on the microsphere. When the microsphere is very close to the trap, it experiences a large negative force and its velocity reduces sharply. Finally, the total force (force imposed by the trap and fluid force) and velocity become zero when the microsphere is immobilized in the trap.

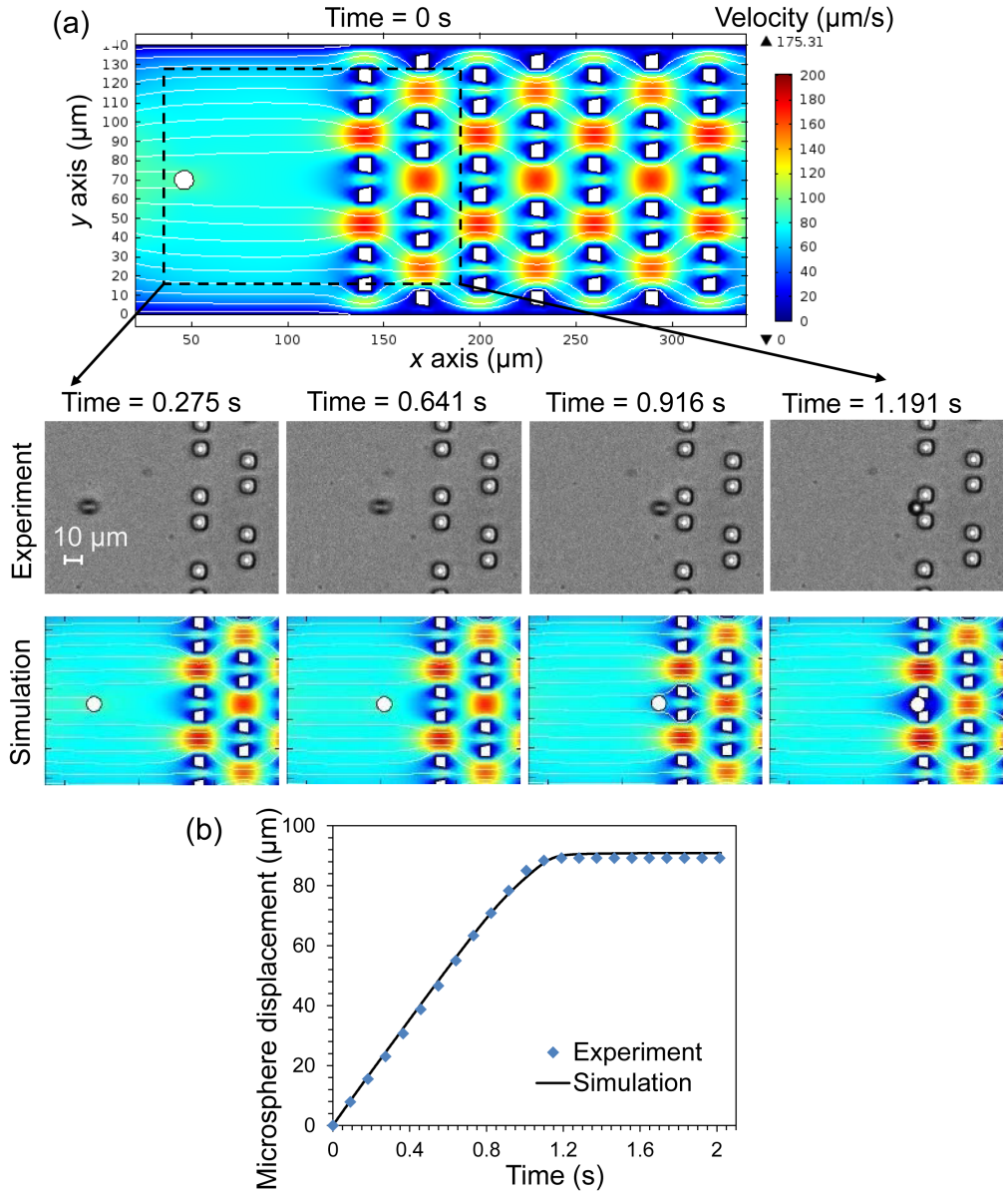

Figure 4.4: (a) Flow velocity field at a series of time points (full size plot at $t = 0$ s, and zoomed-in plots at $t = 0.275$ s, 0.641 s, 0.916 s, and 1.191 s). The streamlines indicate the flow direction, and the rainbow color represents the flow-velocity magnitude distribution with a fixed value range for all plots. These plots also present the positions of a 10 μm microsphere at these different time points in the experiment and in the simulation. (b) Time-dependent plots of the displacements of the microsphere along the x direction in the simulation and in the experiment.

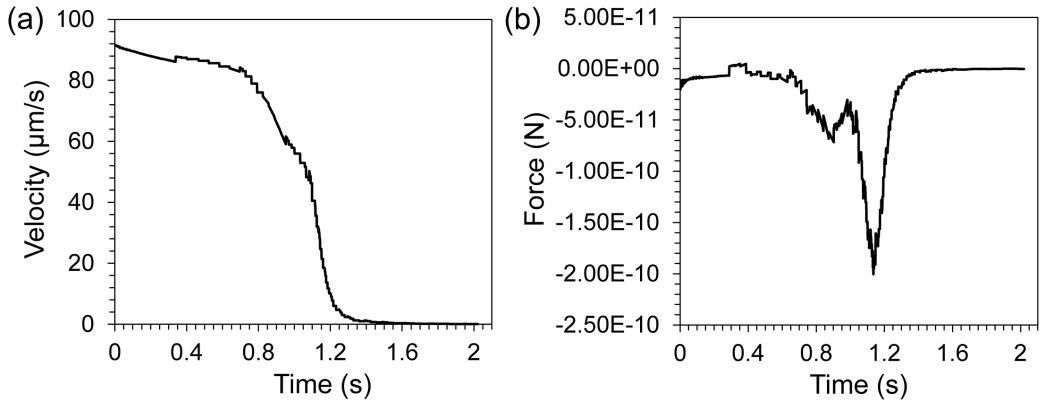

Figure 4.5: Time-dependent plots of the microsphere's (a) velocity and (b) experienced total force, along the x direction.

We note that the line plots of the velocity and force are not smooth and have discontinuities. Because the velocity is the displacement's first derivative and the force is related to its second derivative, when the sizes of the discrete elements in solving the equations are not infinitely small, any small perturbation in the solution of displacement will result in large discontinuities in its derivatives. There is even a peak in the force plot before this variable decreases sharply. Remeshing and solution mapping seem to have resulted in the peak, because at that time the gap between the microsphere and the trap is too small to cause severe mesh deformation.

4.4.3 Flow Pressure Field

Figure 4.6 shows the pressure field of the flow at a series of time points (full size plot at $t =$ 0 s, and zoomed-in plots at $t = 0.275$ s, 0.641 s, 0.916 s, and 1.191 s). The rainbow-colored contour represents the pressure magnitude distribution: the magnitude of the pressure at the inlet is the greatest and it gradually decreases along the channel until the outlet. However, we note that the pressure at the outlet is actually predefined as zero through boundary condition Eq. (4.12), which may not be the real situation. An accurate description of pressure boundary conditions merits application-specific refinements.

When the microsphere is far from the trap, it is impacted only by the flow pressure and viscous drag surrounding it. When the microsphere is close to the trap, the pressure between

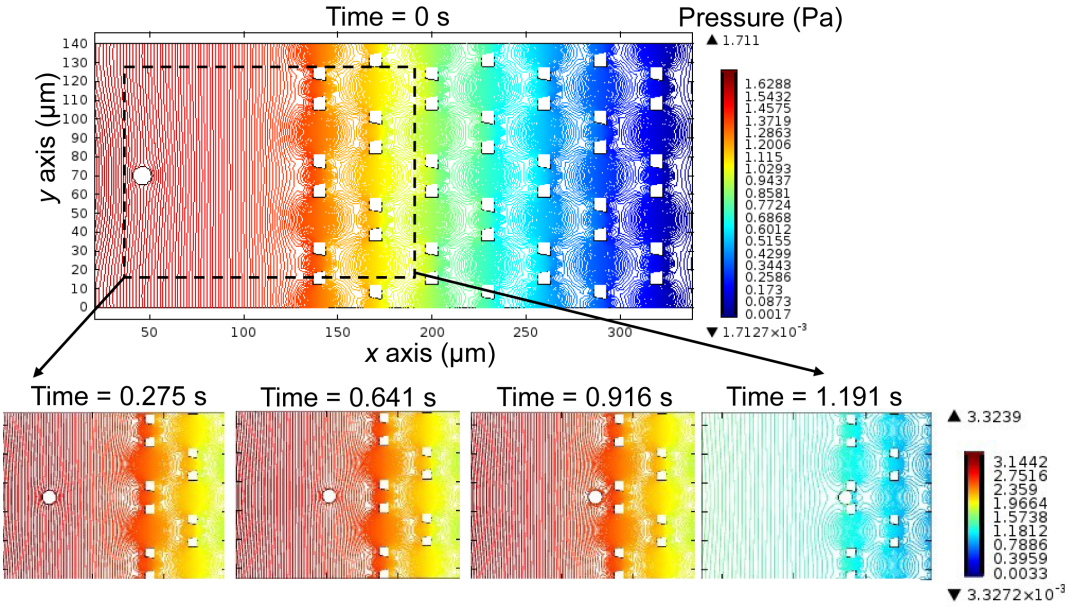

Figure 4.6: Flow pressure field at a series of time points (full size plot at $t = 0$s, and zoomed-in plots at $t = 0.275$ s, 0.641 s, 0.916 s, and 1.191 s). The rainbow-colored contour represents the pressure magnitude distribution. The pressure magnitude ranges of the plots are the same (0 Pa∼1.711 Pa) except for that of the plot at $t = 1.191$ s (0 Pa∼3.3239 Pa), where the greatest pressure (3.3239 Pa) occurs in the very small gap between the microsphere and the trap.

the microsphere and the trap increases and imposes negative force on the microsphere. When the microsphere is immobilized in the trap, the pressure in the very small gap between the microsphere and the trap becomes even larger than that at the inlet. Therefore, to ensure stable trapping of the microsphere, i.e., that the microsphere is retained in the trap and is not swept away due to the transient flow motion around the trap, a persistent pressure should be provided at the inlet.

4.4.4 Stress on the Microsphere

Figure 4.7 presents the von Mises stress on the microsphere at a series of time points (zoomed-in plots at $t = 0$ s, 0.275 s, 0.641 s, 0.916 s, and 1.191 s). The von Mises stress [93] is a scalar stress value computed from the stress tensor of a solid, which is often used in determining whether a particle will yield when subjected to a complex loading force. In this figure, the

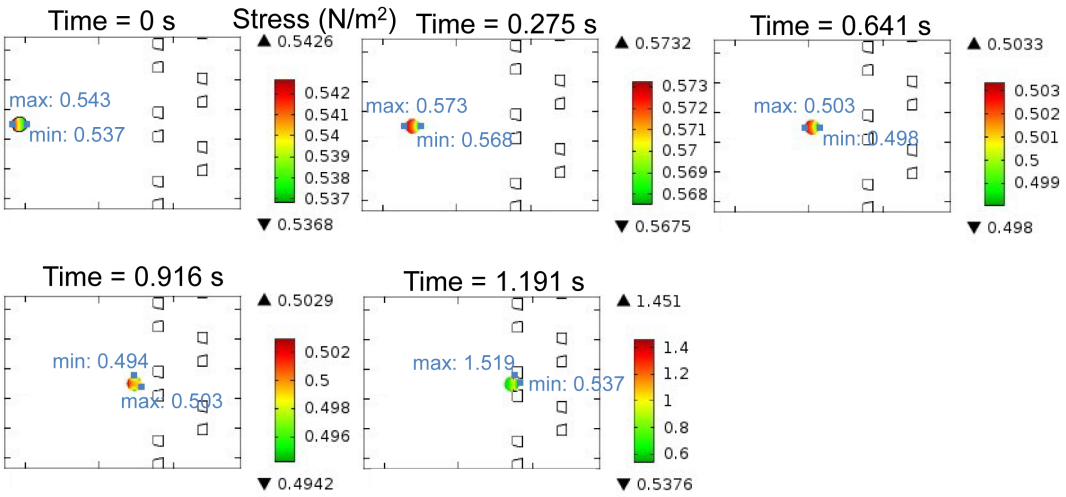

Figure 4.7: Stress on the microsphere at a series of time points (zoomed-in plots at $t = 0$ s, 0.275 s, 0.641 s, 0.916 s, and 1.191 s). The color of the microsphere represents the stress magnitude distribution, and the maximum and minimum stress points on the microsphere are also presented in small blue squares.

traffic color on the microsphere represents the stress magnitude distribution. The maximum and minimum stress points are also presented. When the microsphere is far from the trap, the stress on the microsphere is almost a constant and is uniformly distributed, although due to the larger fluid pressure, the stress close to the inlet is a bit larger than that of the outlet. When the microsphere is trapped, because of the force from the trap, the stress on the microsphere increases dramatically, especially at the contact points of the microsphere. Nevertheless, the stress is not sufficient to cause any obvious deformation of the microsphere, due to its low elasticity.

If the trap array device is applied to trap biological cells (e.g., blood cells), the investigation of stress acting on the cells is useful. Stress can lead to biological and biochemical consequences in cells, such as cell deformation, differentiation, and even cell death [94], [95]. Simulation will help select proper experimental conditions (fluid pressure, velocity, trap material, etc.) that avoid undesired damage to the fragile particles.

4.4.5 Investigations of the Trap's Geometric Parameters and Critical Fluid Velocity

The microfluidic microsphere-trap array device employs fluidic resistance and path engineering to perform precise hydrodynamic trapping of micron-scaled particles. The mechanism is detailed in Chapter 3 [80]. Now we employ the FEM simulations to explore the critical fluid velocity and the critical trap width, above which subsequent microspheres will collide with the filled trap by inertia, instead of bypassing the trap. Such collisions prevent us from operating the microsphere trapping process in a controlled manner and may cause large fluidic errors. The critical velocity found in the simulations suggests that microsphere-trapping experiments be operated below this velocity. The critical trap width found in the simulations adds an additional optimization constraint (i.e., an upper limit of the trap width) to the optimal design framework of the device [80].

To study the effect of the trap width, both v (the upper width of the trap opening) and s_t (the upper width of the groove walls) can be adjusted. Here, we gradually increase v from 10 μm and keep $s_t = 6.6$ μm constant. For a feasible fabrication, the value of s_t is selected to ensure that the aspect ratio (the ratio of transverse dimensions to height $h = 16.5$ μm) is greater than 0.4 [85]. The other geometric parameters of the trap array are also kept constant, as given in Table 4.2. To eliminate simulation symmetry, the microsphere is released 5 μm off the centerline of the y direction of the flow domain. Figure 4.8(a) shows that at $v = 10$ μm and an inlet mean velocity $u_0 = 70$ μm/s, the microsphere easily bypasses the trap. When the width of the trap increases, the zero-flow-velocity area increases and the microsphere has to travel a longer distance along the trap to bypass it. Our simulation indicates that when v increases to 24 μm (Fig. 4.8(b)), the microsphere collides with the trap. Therefore, to ensure efficient bypassing of the occupied trap, v should not be larger than 24 μm. On the other hand, v should not be too small compared with the microsphere's diameter. Otherwise, only the bottom of the microsphere enters the trap, and the microsphere is easily swept away by the transient flow around it.

To study the effect of fluid velocity, we keep the trap's geometric parameters constant and gradually increase the inlet mean velocity u_0. As shown in Fig. 4.8(c), when u_0 increases

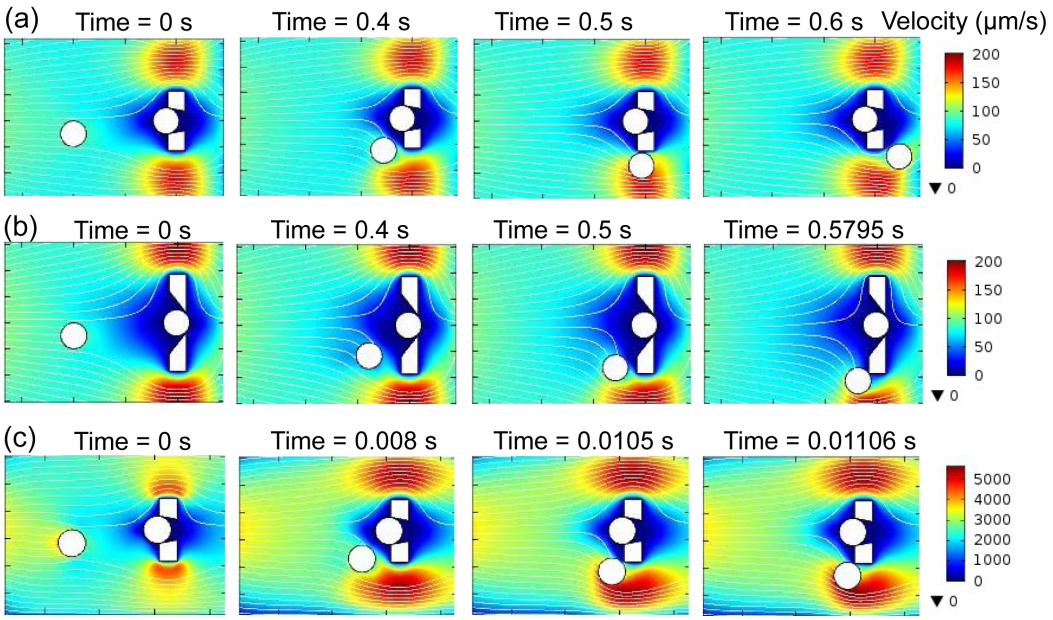

Figure 4.8: Effects of trap width and fluid velocity on the microsphere's motion toward a filled trap, shown by zoomed-in flow velocity field plots. The streamlines indicate the flow direction, and the rainbow color represents the flow-velocity magnitude distribution. (a) When the upper width of the trap opening v = 10 μm and the inlet mean velocity u_0 = 70 μm/s, the microsphere easily bypasses the filled trap. (b) When u_0 is fixed at 70 μm/s and v increases to 24 μm, the microsphere collides with the boundary of the trap. (c) When v is fixed at 10 μm and u_0 increases to 2500 μm/s, the microsphere also collides with the boundary of the trap.

to 2500 μm/s, the microsphere collides with the boundary of the trap. Therefore, we estimate u_0 = 2500 μm/s as the critical fluid velocity, and suggest that microsphere-trapping experiments be operated below this velocity.

Note that in this subsection's simulations, the mesh size is assigned to be extremely fine and the time step size is set as Δt=1e-6 s, to ensure the convergence of the solver and the accuracy of these critical parameters.

4.4.6 Discussion

Numerical simulation may not exactly replicate events in reality, especially when some physical phenomena are not considered or incorporated in the model. Numerical approximations

in the finite element method also lead to slightly inaccurate simulation results. However, careful examination of simulation results and comparison with the experimental data can validate the use of the model as a benchmarking and explorative tool.

In this chapter we focused on the hydrodynamic trapping of the microsphere, i.e., the interactions among fluid and the microsphere, the fluid viscous drag force and pressure exerted on the microsphere, and the microsphere's trajectories (displacements). The interactions among the microspheres were enabled by the changes of fluid flow. While the interactions actually comprise a variety of mechanisms and forces spanning several length scales, such as electrostatic, elastic, and other short range surface forces; these phenomena are difficult to represent at the present level of modeling. Nevertheless, in situations where the number of microspheres in the fluid is small, such as in our trap array device where the concentration of microspheres is carefully selected to avoid aggregation and channel clogging, the interactions among microspheres seldom happen. Therefore, for these situations, the overall numerical efficiency is not affected. Further refinements of the model could include the full hydrodynamic interactions among the microspheres.

Though we tested only hydrodynamic trapping of microspheres in our device, we have made the simulation customizable and openly accessible to other researchers and have provided guidelines on the simulation set-up, including how to choose the mesh properties, moving mesh conditions, time step size, and solver type. Therefore, one may tailor the simulation to investigate similar microfluidic systems with complex structures and a variety of particles, such as colloids, biological cells (e.g., red blood cells, circulating tumor cells), polymers, and target-tagged microspheres, by modifying the properties of the particles (e.g., elasticity, structure). To our knowledge, such customizable and ready-to-use tools for similar microfluidic systems are not easily accessible for device fabricators or users. We believe this model will be of particular interest to biomedical research that involves blood flow within microvessels, cell or particle transport and migration, bio-imaging, or drug delivery.

4.5 Summary

In this chapter, we studied the hydrodynamic trapping in the microfluidic microsphere-trap arrays by finite element simulation. In the simulations, the time-dependent, laminar,

and incompressible fluidic dynamics and solid mechanics equations were coupled and solved computationally through finite element techniques. The simulated hydrodynamics in the microfluidic channel impacting the moving microsphere agreed well with the experimental observation. The study of the hydrodynamic trapping enables rational design on the geometric parameters, fluid velocity and pressure, and stress on the microspheres in the flow. Therefore, the FEM simulations provide a powerful explorative tool in designing and implementing microfluidic devices.

Chapter 5

Simultaneous Detection of Multiple Biological Targets using Optimized Microfluidic Microsphere-Trap Arrays[4]

In the previous two chapters, we provided a novel geometric structure for a microfluidic microsphere-trap array device and built an analytical framework to optimize the geometry of the trap arrays to maximize the packing density, while simultaneously satisfying other criteria. We also provided a step-by-step formulation of a FEM model for this device and applied the model to investigate the hydrodynamic trapping of the microspheres. In this chapter, we extend our analytical framework to build a optimized microfluidic microsphere-trap array device that enables simultaneous, efficient, and accurate screening of multiple biological targets in a single microfluidic channel.

5.1 Introduction

Microsphere arrays can be used to effectively detect and quantify biological targets, such as mRNAs and proteins, which are key biomolecules for maintaining normal physiological and

[4]Based on X. Xu, Z. Li, P. Sarder, N. Kotagiri, and A. Nehorai, "Simultaneous Detection of Multiple Biological Targets using Optimized Microfluidic Microsphere-Trap Arrays", *Journal of Micro/Nanolithography, MEMS, and MOEMS*, vol. 13, 013017, Mar. 2014.

molecular activities in cells and organs. In the arrays, the microspheres are functionalized with ligands (receptors) on their surface that are specific to certain targets [11], [19], [69], [96]. These arrays have great potential for the independent, quantitative, and simultaneous assay of multiple types of targets in small volumes of material, and for collecting statistically rigorous data from numerous microspheres for each type of target. Integrating microfluidic technology with microsphere arrays has many advantages, such as offering a controlled liquid environment, reducing reagent cost and hybridization assay time, and providing the potential for mass production of devices at low cost [23], [26]. Therefore, these systems have played an increasingly important role in life science research and medical diagnostics.

To simultaneously detect and correlate multiple targets, researchers have designed advanced array systems. To identify the different targets on the microspheres, Luminex's suspension array technology sorts microspheres based on their colors [69], Illumina's bead array systems utilize complex protocols and setups to code and decode the microspheres [16], and label-based approaches rely on different labels on the targets (e.g., fluorescent dyes at distinct emission wavelengths) [11]. In these approaches, the microspheres are randomly suspended or placed so that the captured different targets are mixed. As a result, subsequent imaging and data analysis requires complex segmentation of the microspheres, and the noise in the imaging makes the analysis even more prone to errors in identifying the targets [97], [98], [99]. To solve the limitations of these label-based approaches, we have designed a microsphere array device with microspheres immobilized at predetermined locations in a highly parallel and compact fashion [19], [80]. Thus target identification can be achieved according to the precise positioning of the microspheres, which simplifies the image analysis and is error-free. For simultaneous detection of multiple targets, one possibility is to implement multiple channels connected with individual chambers on a microfluidic chip, and use on-chip valves to open or lock the channels to direct the microspheres for a specific type of targets to flow into a specific chamber [30], [31], [32], [33], [34], [35]. While this approach can achieve multiplexing, a disadvantage is that the valves occupy considerable space on the chip and they need sophisticated external control and actuation [36]. Moreover, for effective collection of information, such as profiling multiple proteins or simultaneous mRNA and protein profiling, and for precise control of flow condition and local environment, there is a need for multi-analyte detection in a single microfluidic channel. Therefore, we aim to develop a simple, easy-to-control, and efficient one-channel platform for simultaneous detection and quantification of multiple targets.

In this chapter, to achieve simultaneous and efficient detection of multiple targets by position-encoding in a single-channel device, we design the trap arrays by proposing a simple but effective idea [85]. Specifically, we propose to use microspheres of difference sizes to capture different targets. We select the geometric parameters of the traps to separate and immobilize the different-sized microspheres at different known regions in the same channel by microfluidic hydrodynamic trapping [27], without using different channels (chambers) with on-chip valves. Finally, the targets captured by the microspheres are detected according to their positions [19]. To optimize the performance of our proposed device, we compute the values of the trap arrays' geometric parameters by extending our optimization framework for designing a single target detection device in Chapter 3 [80]. Besides the extension, the adopted optimization constraints from the previous framework are also modified to consider more experimental conditions, such as the variations in the microspheres' sizes and inconsistencies in device's fabrication. To demonstrate the design, we fabricate a device for simultaneous detection of two types of targets, by trapping microspheres of two sizes. We validate the design through finite element fluid dynamics simulations and also by microsphere-trapping experiments on the fabricated device. The results show that the device achieves the position-encoding of the microspheres with few fluidic errors, making our framework promising for building devices for simultaneous detection of more targets. We envision that the device can be utilized to separate, sort, or enumerate cells, including circulating tumor cells and blood cells, based on cell size and deformability [77], [79], [100], [101]. To achieve these goals, however, further development of the device is required to solve issues such as blood clogging. Overall, our device for simultaneous detection of multiple targets in a single channel improves information gathering efficiency, reduces fabrication complexity, and is promising as a fast and cheap disease diagnostic tool.

This chapter is organized as follows. In Section 5.2, we describe the design strategy of the microsphere-trap arrays for simultaneous detection of multiple targets. We then present the optimization framework to select the device's trap geometry. In Section 5.3, to demonstrate our design, we compute the geometric parameters of a device for detecting two types of targets. We then provide finite element fluid dynamics simulations and experimental validation of the device, both of which show the device has excellent performance. Section 5.4 provides the biological experiments that we are currently working on with our device. Section 5.5 summarizes the chapter.

5.2 Methods

5.2.1 Design Strategy

The design of the microfluidic microsphere array platform for simultaneous detection of multiple targets in a single channel is based on our previous work, in which we proposed and implemented a microfluidic microsphere-trap array device to capture uniform-sized microspheres [80]. Here we briefly describe the general configuration of the device, as shown in the schematic Fig. 5.1. The trap arrays, consisting of inverted-trapezoid grooves, are made of polydimethylsiloxane (PDMS). Each row of the trap arrays is offset horizontally with respect to the one ahead. The platform has an inlet and an outlet to let through a fluidic stream. The microspheres with specific ligands are contained in the stream and are immobilized in the traps by hydrodynamic trapping when the stream flows through the channel. The trapping mechanism is detailed in our previous Chapter 3 [80].

For simple and simultaneous screening of multiple types of targets in a single channel, we employ microspheres of different sizes to capture different targets. We design the geometric parameters of the traps to immobilize the different-sized microspheres at different known regions on a single channel. Particularly, from the inlet to the outlet in the chip, the arrays of the largest traps are located nearest to the inlet, the upper and bottom openings of which are optimized to trap the largest microspheres and let through the smaller microspheres. The arrays of the second largest traps follow the largest trap arrays, then the arrays of the third largest traps, and so on. Trapping of the different-sized microspheres during the experiment occurs in reverse order. We first load the fluidic stream containing the smallest microspheres, which are to be immobilized by the smallest trap arrays at the bottom of the channel. Then we load the second smallest microspheres, until all the different-sized microspheres are immobilized at their corresponding regions. The targets, either tagged on the microspheres before the loading, or tagged on the immobilized microspheres in the traps through on-chip reaction, will be identified by the positions of their tagged microspheres [19]. The targets are further quantified by subsequent microscopy. We note that to avoid overload of these microspheres, their concentrations should be carefully controlled so that the numbers of microspheres are less than the numbers of their corresponding traps (i.e., a few traps may remain empty).

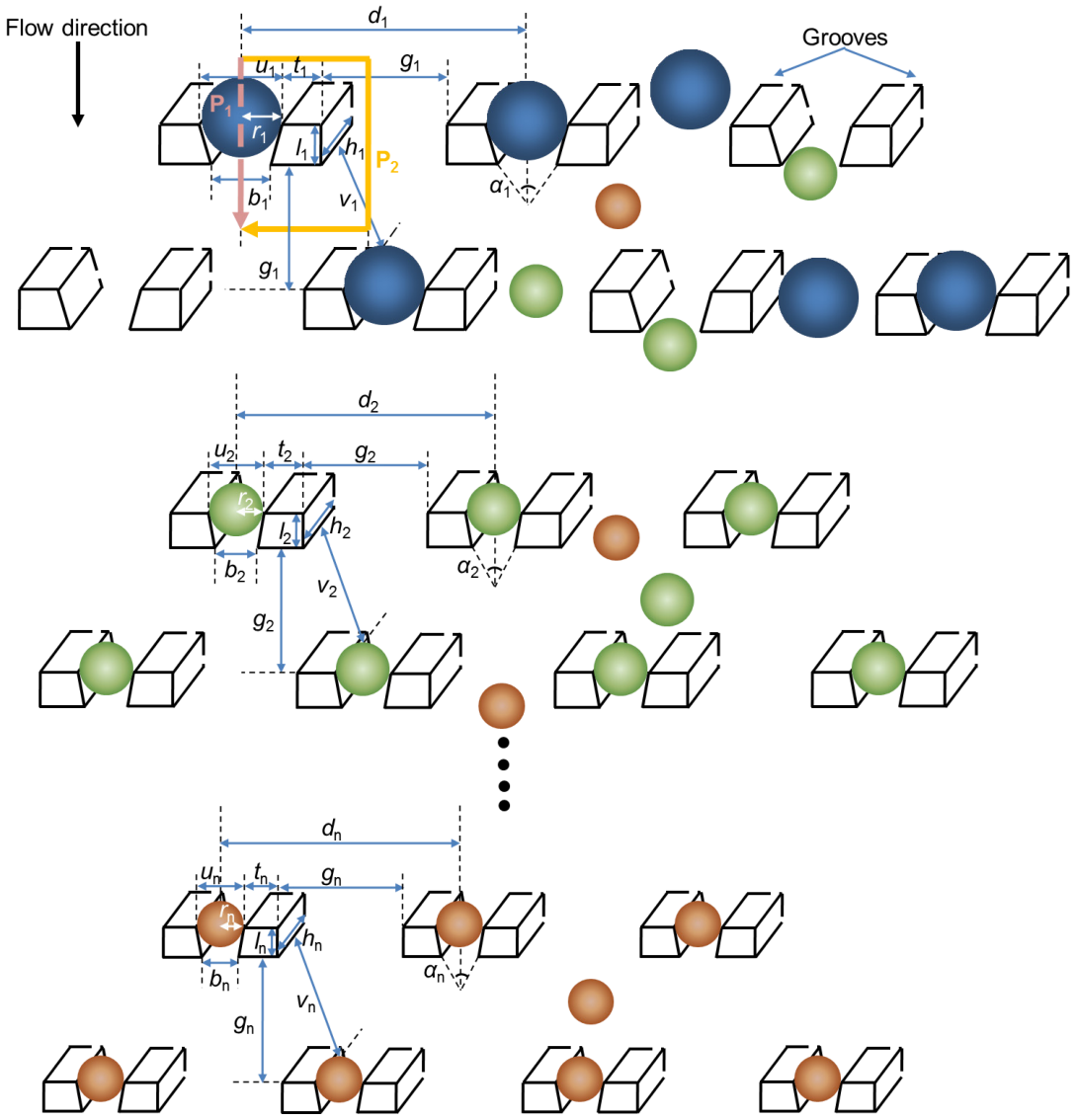

Figure 5.1: Schematic diagram of microfluidic microsphere-trap array geometries for simultaneous detection of multiple types of targets. Microspheres of distinct sizes (shown in blue, green, and orange) are encoded with different specific receptors (not shown) to capture different types of targets. The corresponding trap arrays for immobilizing the microspheres are presented here, with two adjacent rows for microspheres of each size. From the inlet to the outlet, the arrays of the largest traps are located nearest to the inlet, to trap the largest microspheres and let through the smaller microspheres. The arrays of the second largest traps follow the largest trap arrays, to trap the second largest microspheres and let through the remaining smaller microspheres, and so on.

To optimize the device performance, in Chapter 3 [80], we developed an analytical method to optimize the values of the trap array geometric parameters. This optimization maximized the microsphere arrays' packing density to make the device compact. It simultaneously satisfied other criteria, such as efficient microsphere trapping, minimum fluidic errors such as channel clogging or multiple microspheres in a single trap, feasible fabrication, and minimum errors induced during the subsequent fluorescence imaging. Microsphere-trapping experiments showed that the optimized device greatly outperforms the un-optimized device. Here, to optimize the geometric parameters for our multiple target detection device, we extend and modify the optimization framework by revising the objective function and adding constraints to satisfy the design strategy. Besides the extension, we also consider more constraints involving experimental conditions, such as the variations of the microspheres' sizes. The next subsection describes the optimization of our design in details.

5.2.2 Optimization of the Trap Geometry

Here we present the formulation of the optimal design, including the optimization objective and constraints, of our microfluidic microsphere-trap arrays for simultaneous detection of multiple targets. Figure 5.1 shows the schematic diagram of the trap array geometries and depicts the corresponding geometric parameters. Microspheres of n distinct sizes (for demonstration, three sizes are presented in blue, green, and orange colors) are encoded with n specific ligands (not shown) to capture n types of targets. For the microsphere of the i^{th} largest ($i = 1, ..., n$) size and its corresponding traps, we first define r_i as the microsphere radius. However, due to manufacturing limitation, the sizes of the microspheres used in experiments are not perfectly uniform. In other words, the radius of the i^{th} microsphere is a random variable R_i, with its mean $\mathbb{E}[R_i]$ and standard deviation $\sigma[R_i]$ provided by the manufacturer. We also denote h_i as the trap groove walls' height, l_i and t_i as the groove walls' length and upper width, u_i and b_i as the trap opening's upper and bottom widths, and α_i as the trap's trapezoidal angle. We further denote g_i as the gap width between two traps in the same row, v_i as the distance between a trap groove wall and a microsphere caught in a trap in the next row, and d_i as the distance between two immobilized microspheres in the same row. Again, to eliminate the units of these parameters, we normalize them by dividing by the corresponding groove walls' height h_i (see Fig. 5.1). We use below the tilde sign ˜ to

represent the resulting normalized parameters; e.g., $\tilde{u}_i$ represents the normalized u_i. Finally, for the i^{th} microsphere, we denote a single trap and its surrounding area as S_i, and use ρ_i to denote the corresponding trap array's packing density.

Now we present our optimization framework to obtain the optimal geometric parameters of the trap arrays for microspheres of n sizes. The optimization objective to maximize the packing density $\rho_i, i = 1, ..., n$ for each trap region, which is equivalent to minimizing the area S_i with respect to the geometric parameters $\boldsymbol{\delta}_i = [R_i, h_i, l_i, u_i, b_i, t_i, g_i, d_i, v_i]^T$. To summarize, the optimization problem is

$$\boxed{\rho_{i,\text{opt}} = 1/S_{i,\text{opt}}, \text{ with } S_{i,\text{opt}} = h_i^2 \cdot \min_{\boldsymbol{\delta}_i} (\tilde{g}_i + \tilde{l}_i) \cdot (\tilde{u}_i + 2\tilde{t}_i + \tilde{g}_i),} \tag{5.1}$$

where $\boldsymbol{\delta}_i \in \{\mathcal{C}_{i1} \bigcap \mathcal{C}_{i2} \bigcap \mathcal{C}_{i3} \bigcap \mathcal{C}_{i4} \bigcap \mathcal{C}_{i5} \bigcap \mathcal{C}_{i6} \bigcap \mathcal{C}_{i7} \bigcap \mathcal{C}_{i8}\}$ and $\mathcal{C}_{ij}, j = 1, ..., 8$ are the optimization constraints providing the feasible parameter spaces for the i^{th} microspheres and traps. We note that constraints $\mathcal{C}_{i1}$, $\mathcal{C}_{i5}$, and $\mathcal{C}_{i6}$ are adapted from the previous optimization framework [80], $\mathcal{C}_{i2} - \mathcal{C}_{i4}$ are modified to consider the randomness of microsphere size and fabrication variations, and $\mathcal{C}_{i7}$ and $\mathcal{C}_{i8}$ are specifically proposed to achieve simultaneous detection of multiple targets. Details are given below.

- *Constraint* $\mathcal{C}_{i1}$ ensures hydrodynamic trapping. That is, the trap array geometry is designed so that path P_1 (pink line in Fig. 5.1) for an empty trap has a lower flow resistance than path P_2 (green line in Fig. 5.1). Then the microsphere in the fluid through the channels chooses path P_1 to move into an empty trap. However, once the trap through P_1 is filled by a microsphere, the flow resistance in P_1 increases and becomes larger than that in P_2. Thus, subsequent microspheres divert to path P_2 and bypass the filled trap. The specific representation of $\mathcal{C}_{i1}$ is adapted from Eq. (7) in Chapter 3 [80].

- *Constraint* $\mathcal{C}_{i2}$ ensures a single microsphere in each trap and avoids multiple microspheres trapped at one location. We require that the trap opening bottom width b_i be smaller than the microsphere diameter ($b_i < 2R_i$), and that the trap opening upper width u_i and the groove wall length l_i be smaller than the sum of two microsphere diameters ($u_i < 4R_i$,$l_i < 4R_i$). Because R_i is a random variable and is not present in the objective function, these constraints can be written in a probabilistic form [102].

For example, the probabilistic constraint for b_i is $\text{Prob}\{b_i < 2R_i\} \geq q$, with q as the probability that is usually selected close to 1. Because the number of microspheres is usually large and the mean $\mathbb{E}[R_i]$ and standard deviation $\sigma[R_i]$ of the microsphere's radius can be obtained from the manufacturer, we assume R_i follows a normal distribution by the Central Limit Theorem [103]. Therefore, the constraint for b_i is rewritten as $b_i < 2(\mathbb{E}[R_i] - \Phi^{-1}(q)\sigma[R_i])$, where $\Phi^{-1}(\cdot)$ is the quantile function of the standard normal distribution. Similarly, we rewrite the probabilistic constraints for u_i and l_i as $u_i < 4(\mathbb{E}[R_i] - \Phi^{-1}(q)\sigma[R_i])$ and $l_i < 2(\mathbb{E}[R_i] - \Phi^{-1}(q)\sigma[R_i])$, respectively. Finally, we consider possible fabrication variations and add 0.2 μm safety margin [56]. Therefore, constraint $\mathcal{C}_{i2}$ is

$$\begin{aligned} \mathcal{C}_{i2} = \{&\tilde{b}_i \leq 2(\mathbb{E}[R_i] - \Phi^{-1}(q)\sigma[R_i])/h_i - 0.2/h_i, \\ &\tilde{u}_i \leq 4(\mathbb{E}[R_i] - \Phi^{-1}(q)\sigma[R_i])/h_i - 0.2/h_i, \\ &\tilde{l}_i \leq 4(\mathbb{E}[R_i] - \Phi^{-1}(q)\sigma[R_i])/h_i - 0.2/h_i\}. \end{aligned} \tag{5.2}$$

- *Constraint* $\mathcal{C}_{i3}$ ensures that a microsphere is stably immobilized in a trap and is not swept away by the transient fluid flow around it. This constraint is given by constraining the trapezoid angle α_i to be greater than 5° ($\alpha_i = 2\text{arctan}(0.5(u_i - b_i)/l_i) \geq 5°$) and the groove wall length l_i to be greater than the microsphere's radius ($l_i > R_i$). Similar to constraint $\mathcal{C}_{i2}$, we consider the randomness of R_i and the safety margin, $\mathcal{C}_{i3}$ becomes

$$\mathcal{C}_{i3} = \{-\alpha_i \leq -5°, -\tilde{l}_i \leq -(\mathbb{E}[R_i] + \Phi^{-1}(q)\sigma[R_i])/h_i - 0.2/h_i\}. \tag{5.3}$$

- *Constraint* $\mathcal{C}_{i4}$ avoids channel clogging. We require the gap width g_i between two traps in the same row to be greater than one microsphere's diameter ($g_i > 2R_i$) while be smaller than the sum of two microspheres' diameters ($g_i < 4R_i$). We also require the distance v_i between a trap groove wall and a microsphere filled in a trap in the next row to be greater than one microsphere's diameter ($v_i > 2R_i$, where $v_i = \sqrt{(g_i - R_i)^2 + (0.5g_i)^2}$). Again, considering the variations of microsphere size

and fabrication, $\mathcal{C}_{i4}$ becomes

$$\begin{aligned}\mathcal{C}_{i4} = \{&\tilde{g}_i \leq 4(\mathbb{E}[R_i] - \Phi^{-1}(q)\sigma[R_i])/h_i - 0.2/h_i, \\ &-\tilde{g}_i \leq -2(\mathbb{E}[R_i] + \Phi^{-1}(q)\sigma[R_i])/h_i - 0.2/h_i, \\ &-\tilde{v}_i \leq -2(\mathbb{E}[R_i] + \Phi^{-1}(q)\sigma[R_i])/h_i - 0.2/h_i\}.\end{aligned} \tag{5.4}$$

- *Constraint* $\mathcal{C}_{i5}$ ensures feasible fabrication, i.e., the device geometric aspect ratios (the ratio of transverse dimensions to trap groove wall height, e.g., $\tilde{t}_i = t_i/h_i$) should be limited to the range of $[0.4, 2.5]$. This constraint is given by

$$\begin{aligned}\mathcal{C}_{i5} = \{&\tilde{l}_i, \tilde{g}_i, \tilde{b}_i, \tilde{u}_i, \tilde{t}_i \leq 2.5, \\ &-\tilde{l}_i, -\tilde{g}_i, -\tilde{b}_i, -\tilde{u}_i, -\tilde{t}_i \leq -0.4\}.\end{aligned} \tag{5.5}$$

- *Constraint* $\mathcal{C}_{i6}$ satisfies the optimal distance $d_{i,\text{opt}}$ between microspheres obtained in the statistical design to minimize image analysis error [12], [13], i.e., the distance d_i ($d_i = u_i + 2t_i + g_i$) between the centers of two immobilized microspheres should be greater than $d_{i,\text{opt}}$. Therefore, $\mathcal{C}_{i6}$ is

$$\mathcal{C}_{i6} = \{-\tilde{d}_i \leq -d_{i,\text{opt}}/h_i\}. \tag{5.6}$$

- *Constraint* $\mathcal{C}_{i7}$ considers geometry in our design strategy. We expect the i^{th} largest microspheres to be immobilized by the i^{th} traps, while the $(i+1)^{\text{th}}$ microspheres flow through the channels or the openings of the 1^{st} to i^{th} traps, and then are immobilized by the $(i+1)^{\text{th}}$ traps. This requirement adds one constraint ($\mathcal{C}_{i7}$) in the optimization of the geometric parameters, i.e., the bottom width of the i^{th} trap opening b_i should be larger than the diameter of the $(i+1)^{\text{th}}$ microsphere ($\tilde{b}_i > 2\tilde{R}_{i+1}$). Therefore,

$$\mathcal{C}_{i7} = \{-\tilde{b}_i \leq -2(\mathbb{E}[R_{i+1}] + \Phi^{-1}(q)\sigma[R_{i+1}])/h_i - 0.2/h_i\}. \tag{5.7}$$

- *Constraint* $\mathcal{C}_{i8}$ avoids excess large microspheres clogging the channels in the small microsphere trap region. Though the concentrations of the microspheres will be carefully controlled to ensure the microspheres of each size be fully immobilized at their corresponding region, there might be excess $(i-1)^{\text{th}}$ microspheres flowing into the i^{th} trap

region in the worst case. We assume the i^{th} trap region is long enough that the excess $(i-1)^{\text{th}}$ microspheres will not flood into the $(i+1)^{\text{th}}$ trap region. To avoid channel clogging by the $(i-1)^{\text{th}}$ microspheres, we add constraint $\mathcal{C}_{i8}$ on the channel width g_i and the distance v_i with respect to the $(i-1)^{\text{th}}$ microsphere's radius R_{i-1}, i.e.,

$$\begin{aligned}\mathcal{C}_{i8} = \{&-\tilde{g}_i \leq -2(\mathbb{E}[R_{i-1}] + \Phi^{-1}(q)\sigma[R_{i-1}])/h_i - 0.2/h_i, \\ &-\tilde{v}_i \leq -2(\mathbb{E}[R_{i-1}] + \Phi^{-1}(q)\sigma[R_{i-1}])/h_i - 0.2/h_i\}.\end{aligned} \tag{5.8}$$

Therefore, given the number of target types n and the radii ($\mathbb{E}[R_i]$, $\sigma[R_i]$, $i = 1, ..., n$) of the microspheres to capture the targets, we can obtain the geometric parameters $\boldsymbol{\delta}_i$ ($i = 1, ..., n$) of our device by solving the optimization problems in Eqs. (5.1)-(5.8). We apply the grid-search method [58] to solve $\boldsymbol{\delta}_i$ ($i = 1, ..., n$).

5.3 Results and Discussion

To demonstrate the applicability of the proposed design strategy, we designed a device for detecting two types of targets. To validate the device, we used COMSOL Multiphysics 4.3 [59] to perform finite element fluid dynamics simulations of sequential loading of microspheres of two sizes. To further evaluate its performance, we fabricated the device and performed a number of microsphere sequential loading and trapping experiments on it.

5.3.1 Optimized Device for Simultaneous Detection of Two Targets

Based on the optimization formulation, here we compute the optimal geometric parameters of the trap arrays for immobilizing microspheres of two sizes ($n = 2$), for the demonstration of our design in finite element fluid dynamics simulations and experiments. To tolerate manufacturing variations in the two sizes of the microspheres, the values of their radii should be selected with sufficient distinction; we use $\mathbb{E}[R_1] = 7.725$ μm and $\mathbb{E}[R_2] = 5.055$ μm (Bangs Lab, Fishers, IN), with corresponding standard deviations $\sigma[R_1] = 0.55$ μm and $\sigma[R_1] = 0.3515$ μm, respectively. Next we set the constraint probability, i.e., considering the

randomness of the microsphere size, we require the constraints to be satisfied 90% of the time. For simplicity, we keep the values of the trap groove walls' heights h_1 and h_2 fixed. To further simplify the chip fabrication, we assign the same value for h_1 and h_2 ($h_1 = h_2 = h$). The heights should be shallow enough to prevent stacking of multiple microspheres at a single trap. They should also be deep enough to keep the microsphere from flowing out of the channel. Here, according to experimental testing, we choose $h = 2.2\mathbb{E}[R_1] = 3.3\mathbb{E}[R_2] = 16.5$ μm. Furthermore, the minimal distances $d_{1,\text{opt}}$ and $d_{2,\text{opt}}$ to minimize the imaging errors for microspheres of radii $\mathbb{E}[R_1]$ and $\mathbb{E}[R_2]$ are 30 μm and 20 μm, respectively [12]. We further denote the remaining parameters in $\boldsymbol{\delta}_1$ and $\boldsymbol{\delta}_2$ in Eq. (5.1) as the optimization parameters. The values of these optimization parameters are solved and summarized in Table 5.1 (the parameters d_1, d_2, v_1, and v_2 are not listed as they are functions of the other parameters).

5.3.2 Finite Element Fluid Dynamics Simulations

Because three dimensional (3D) fluid dynamics simulations are prohibitively computationally expensive, we perform two dimensional (2D) simulations. The accuracy of the 2D time-dependent simulations of the hydrodynamic trapping of microspheres has been validated by experiments in Chapter 4 [104]. In the simulations, we precisely consider the geometric parameters of the microspheres and the trap arrays as presented in Table 5.1. Recall that the microspheres of different sizes are loaded sequentially to simplify operation; therefore we perform our simulations by first loading the small microspheres and then loading the large microspheres.

Table 5.1: Fixed and optimized geometric parameters for the microfluidic microsphere-trap arrays for simultaneous detection of two types of targets

Fixed values (μm)	$\mathbb{E}[R_1]$	$\mathbb{E}[R_2]$	$\sigma[R_1]$	$\sigma[R_2]$	h_1	h_2
	7.725	5.055	0.55	0.3515	16.5	16.5
Optimized values for the large microsphere-trap arrays (μm)	$l_{1,\text{opt}}$	$u_{1,\text{opt}}$	$b_{1,\text{opt}}$	$t_{1,\text{opt}}$	$g_{1,\text{opt}}$	$S_{1,\text{opt}}$ (μm^2)
	8.62	15.18	11.88	6.60	25.73	1859.3
Optimized values for the small microsphere-trap arrays (μm)	$l_{2,\text{opt}}$	$u_{2,\text{opt}}$	$b_{2,\text{opt}}$	$t_{2,\text{opt}}$	$g_{2,\text{opt}}$	$S_{2,\text{opt}}$ (μm^2)
	6.60	9.90	6.93	6.60	19.36	1102.2

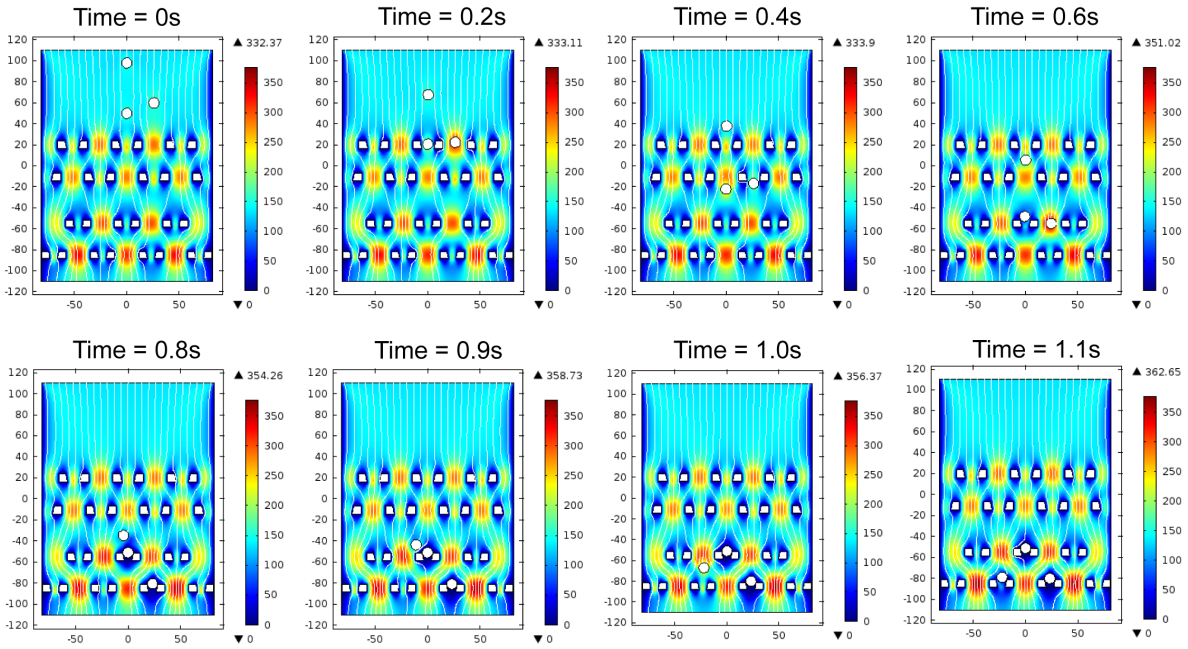

Figure 5.2: Finite element fluid dynamics simulation of small microspheres flowing in the device for detecting two types of targets. The streamlines indicate the flow direction, and the rainbow color represents the flow-velocity magnitude distribution (μm/s) with a fixed value range for all plots. The three small microspheres flow through the large trap array region, into the small trap array region, and are finally immobilized by their corresponding small traps.

Figs. 5.2 and 5.3 present the positions of the microspheres, as well as the fluid velocity magnitude distributions and fluid directions, at several time points. Figure 5.2 shows that the small microspheres flow through the large trap array region, into the small trap array region, and are finally immobilized by their corresponding small traps. Figure 5.3 demonstrates that the large microspheres flow into the large trap region and are immobilized by their corresponding large traps. These finite element simulation results verify the applicability of the device design strategy for simultaneous detection of two types of targets.

The simulations show sequential loading and trapping processes of only two-sized microspheres. In sequential loading, there is no difference between simulations of microspheres of two or more sizes, because the smallest microspheres are loaded and trapped first, then the second smallest microspheres, and so on. Therefore, for modeling of our experiments in the next subsections, we present the simulations of two-sized microspheres here.

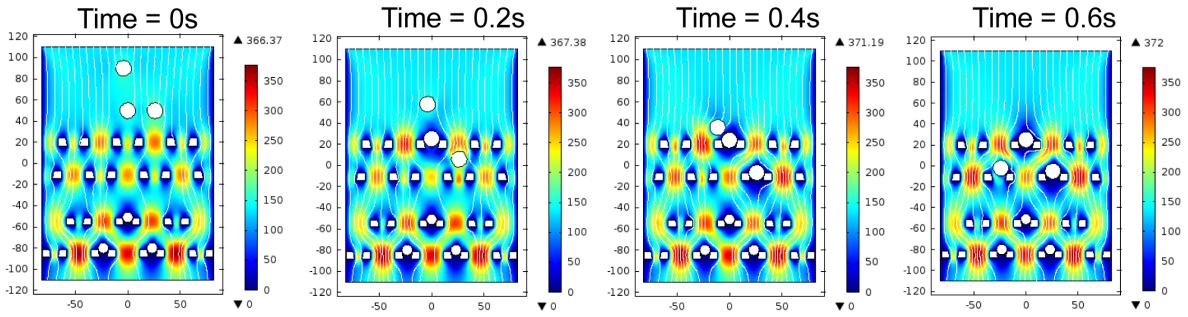

Figure 5.3: Finite element fluid dynamics simulation of large microspheres flowing in the device for detecting two types of targets. The streamlines indicate the flow direction, and the rainbow color represents the flow-velocity magnitude distribution (μm/s) with a fixed value range for all plots. The three large microspheres flow into the large trap array region and are immobilized by their corresponding large traps.

5.3.3 Device Fabrication and Operation

The microsphere-trap array chip was connected by an inlet and an outlet to the fluid source (Fig. 5.4). The optimized chip has a width of 1,000 μm and a length of 1,613 μm. The device, made of PDMS, was fabricated by using soft lithography techniques [35]. We first fabricated a master SU8-3025 mold on a 3" silicon wafer using conventional photolithography. Then PDMS prepolymer (RTV615) was mixed at 10:1 A:B ratio and poured onto the mold. It was degassed in a vacuum chamber and was then cured in an 80 °C oven for 30 minutes. Then we peeled the partially cured PDMS from the mold, and punched liquid inlet and outlet ports through the whole layer using a 0.75 mm diameter biopsy punch. Finally the PDMS layer with fluidic pattern was permanently bonded to a standard glass slide after air plasma treatment. The master molds could be reused many times.

Figure 5.4(a) shows the experimental setup. The PDMS microfluidic trapping device was mounted on an inverted fluorescent microscope (Olympus IX71 (San Jose, CA) equipped with an EMCCD camera (Andor iXon+). Two solutions of polystyrene microspheres (7.725 μm and 5.055 μm mean radii, Bangs Lab, Fishers, IN) were prepared in 1X PBS buffer with 0.05% Tween-20 (Sigma Aldrich, St. Louis, MO) at a concentration of 5×10^4/mL. We note that in the following text, 7.775 μm is referred to as 7.7 μm, and μm is referred to as 5 μm. First, the 5 μm microsphere solution was loaded into a 22 gauge Tygon tubing (Cole Parmer, Vernon Hills, IL). One end of the tubing was connected to the device input port via

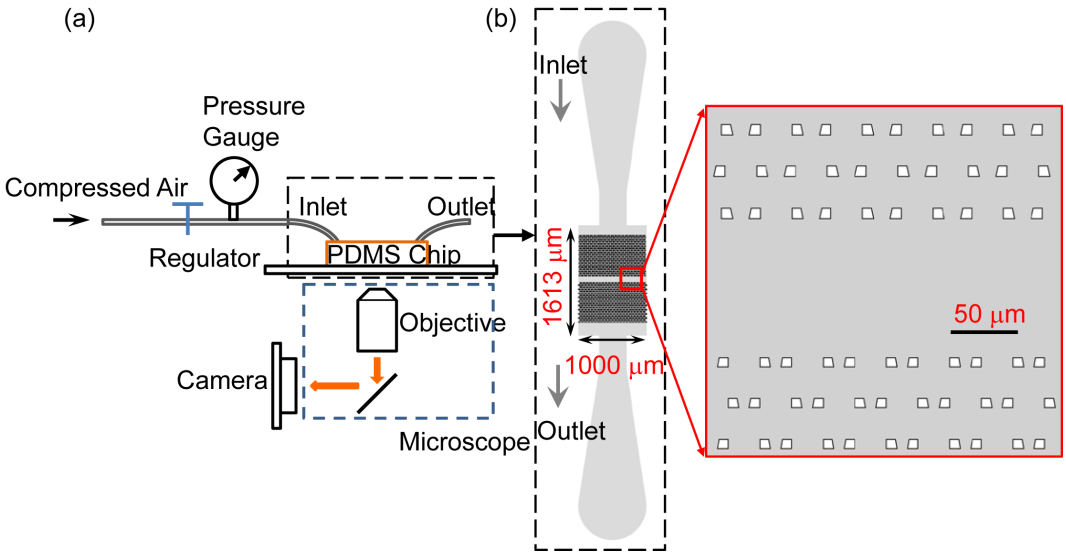

Figure 5.4: (a) Schematic diagram of the experimental setup. (b) Layout (top view) of the microfluidic microsphere-trap array for simultaneous detection of two types of targets.

a stainless steel tube, and the other end was connected to a compressed N_2 pressure source controlled by a pressure regulator with a resolution of 0.1 psi. The microsphere solution was pushed into the device by applying 1 psi pressure to the Tygon tubing. After loading the 5 μm microspheres, the same loading procedure was repeated with a 7.7 μm microsphere solution to complete the loading process. The EMCCD camera captured snapshots and recorded videos of the experimental process.

5.3.4 Experimental Results

We present the experimental results using the fabricated device to sequentially trap microspheres of mean radii 5.055 μm and 7.725 μm. Figure 5.5 presents snap-shots after the 5 μm microsphere loading process (Fig. 5.5(a)) and after the 7.7 μm microsphere loading process (Fig. 5.5(b)). Videos showing the two loading processes are in [105]. The 5 μm traps are located after the 7.7 μm ones to avoid 7.7 μm microspheres trapped at the 5 μm locations. However, overflow of 7.7 μm microspheres to the 5 μm traps can still occur if too many 7.7 μm microspheres are loaded into the device. Therefore, it is preferable to load the 5 μm microspheres first, so that even when the 7.7 μm microspheres overflow to the 5 μm trap region, they will encounter mostly filled 5 μm traps and thus use the bypass routes to

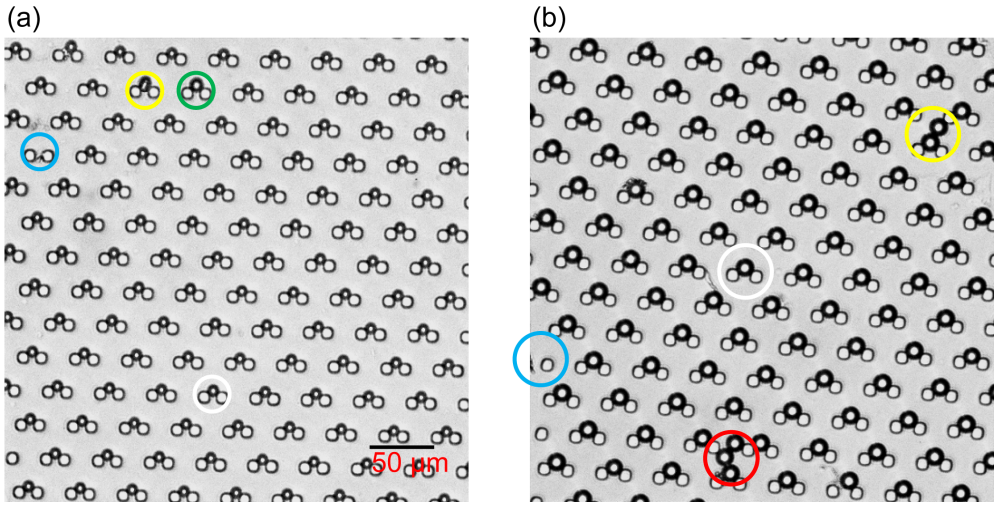

Figure 5.5: Time lapse high-speed camera snap-shots at the end time points of (a) the 5 μm microsphere loading process and (b) the 7.7 μm microsphere loading process. Highlighted areas of trapping results: *single* (white circle), *multiple* (yellow circle), *empty* (blue circle), *clogged* (red circle), and *wrong-trapped* (green circle).

escape the device. In the experiments, to simplify device operation and improve trapping performance, we controlled the microsphere concentration and volume to ensure that very few 7.7 μm microspheres overflowed to the 5 μm trap region.

As for the packing density of our device, from Table 5.1 we compute the areas of each trap and its surroundings, for the small trap and the large trap, as 1102.2 μm^2 and 1859.3 μm^2. The corresponding packing densities for the two trap regions are 907 traps/mm^2 and 537 traps/mm^2, respectively. Therefore, our device provides a much smaller unit cell area and thus much higher packing density than other designs does [24]. Furthermore, in order for the device to function, it is important to have high trapping efficiency, i.e., a single microsphere in one trap (*single*), and to avoid fluidic errors such as multiple microspheres in one trap (*multiple*), empty traps (*empty*), channel clogged by microspheres (*clogged*), and small microspheres captured in the large traps or large microspheres captured in the small traps (*wrong-trapped*). Figure 5.5 also provides illustrative examples of *single*, *multiple*, *empty*, *clogged*, and *wrong-trapped*, highlighted in circles. Intuitively, for both the small and large trap array regions, our device has large *single*, but small values for *multiple*, *empty*, *clogged*, and *wrong-trapped*. To further evaluate the performance of our device, we compute the fractions of traps for *single*, *multiple*, *empty*, and *wrong-trapped* and the fraction of

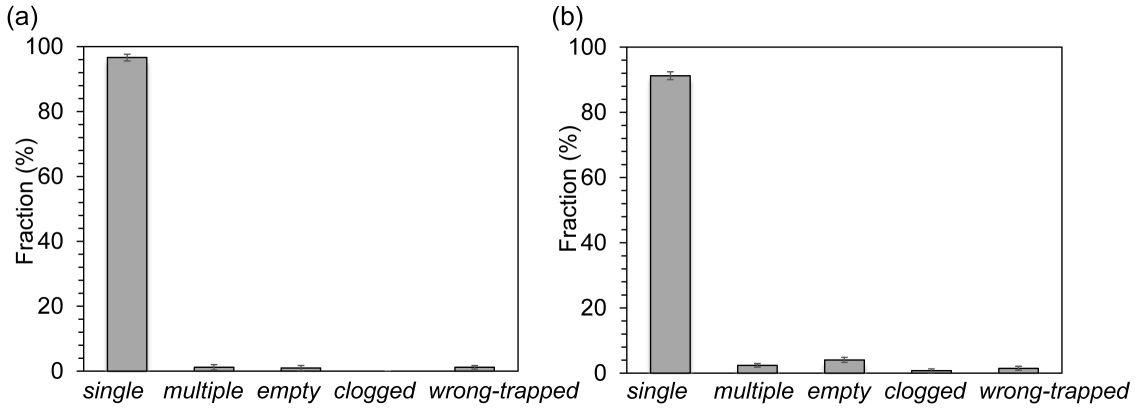

Figure 5.6: Device performance for the sequential loading and trapping of (a) the 5 μm microspheres and (b) the 7.7 μm microspheres at the conclusions of the experiments. The reported values are averaged results obtained on ten devices, and the error bars indicate the standard deviations of the results.

channels for *clogged*, at the conclusions of microsphere-trapping experiments. Figure 5.6 presents these performance measurements, which are computed separately for the small (Fig. 5.6(a)) and the large (Fig. 5.6(b)) trap arrays, based on the results of ten fabricated devices. The standard deviations of these measurements for both trap arrays are small, suggesting that our experimental results are statistically representative and reproducible. For the small and large trap regions, *single* is dominant (96.64% and 91.25%, respectively), and the undesired *multiple* is negligible (1.20% and 2.42%). The percentage of *empty* is close to 0% for the small trap arrays, indicating that almost no small traps remain empty at the end. As long as the small microspheres can find paths to reach the empty traps, they will eventually fill them. However, *empty* is a bit higher (4.08%) for the large trap arrays, because we intentionally limit the total number of large microspheres to avoid overflow. Moreover, the observed *clogged* (0% and 0.58%) and *wrong-trapped* (0.54% and 0.63%) are also negligible for the small and the large trap arrays, given that we carefully controlled the concentrations of the two-sized microspheres.

In summary, the microsphere-trapping experiments successfully demonstrate the high efficiency and few fluidic errors of our microfluidic microsphere-trap array device in trapping microspheres of two sizes, which paves the way for the application of this device for simultaneous detection of two types of targets. However, our design is not limited to detecting two target types. By changing the number of microsphere sizes and providing the microspheres'

radius in the design framework in Eqs. (5.1)-(5.8), we can build a device for simultaneous detection of more targets.

5.3.5 Discussion

In the design of our device, we considered the randomness of the microsphere size and incorporated it into our optimization framework. While the size variation of microspheres is sufficiently small that the consideration may not affect much of the design results, the consideration can be of great importance when designing a device for cells that have a rather wide size distribution.

In the experiments, we loaded two different-sized microspheres into the device sequentially to minimize trapping errors. Ideally, if we can mix the two microspheres and load them simultaneously into the device, simpler and scalable device operation can be achieved. In our preliminary experiments with this approach, we found that it was more difficult to achieve error-free trapping. With mixed loading, we can no longer guarantee the preferred first loading of 5 μm microspheres because large microspheres can overflow to the small microsphere trap region due to the finite chip size, resulting in misplaced microspheres. To achieve simultaneous mixed loading, further investigation is needed to confirm this hypothesis and to help design better trap structures. One possible solution is to ensure the large microspheres never (or rarely) overflow to the small trap region by increasing the number of large traps if the application allows; although this may lead to less efficiently utilized large traps. Better solutions will be to spatially separate the different-sized traps and use hydrodynamic metamaterials, such as deterministic lateral displacement (DLD) structures [106], [107], to direct different-sized microspheres to their corresponding trap regions.

Through finite element simulations and experiments, we demonstrated our design for simultaneous detection of two types of biomolecules captured by microspheres of two sizes. However, as formulated in the Methods Section, our design generally works for the detection of multiple (n up to 5) types of targets, which is limited by the number of commercially available microsphere sizes and the size uniformity. Given the number of target types n and the carefully selected radius r_i $(i = 1, ..., n)$ of the microspheres to capture the targets, we can

obtain the geometric parameters $\boldsymbol{\delta}_i$ $(i = 1, ..., n)$ of our device by solving the optimization problem in Eqs. (5.1)-(5.8).

We proposed the device to immobilize microspheres for capture and detection of multiple biomolecules, such as mRNAs and proteins. However, according to the structure and hydrodynamic trapping mechanism of the device, we also believe that the device can be utilized for label-free approaches to identify, isolate, and enumerate cells of different sizes, including circulating tumor cells and blood cells [77], [79], [100], [101]. To achieve these goals, however, further development of the device is required to solve issues such as blood clogging, cell deformation, etc.

5.4 Biological Experiments

We are currently applying our device to simultaneously detect epithelial growth factor receptor (EGFR) protein and mRNA, commonly overexpressed in cancers of the breast, lung, colon, etc. [108]. Overexpression of EGFR correlates with a poor prognosis and therefore carries significant predictive value in its quantification. Based on the results using our device, we can estimate EGFR and EGFR mRNA expression levels and perform correlation analysis to accurately determine the significant values necessary for early detection of cancer. Figure 5.7 provides an example experiment where we applied our device to perform sensitivity detection of cancer biomarkers through fluoroimmunoassays. Protein G coated polystyrene microspheres pre-incubated with an anti-EGFR polyclonal antibody (capture Ab) were first immobilized by the traps. Sequential washing-loading steps were implemented, and purified EGFR was introduced, followed by quantum dot (QD525) labeled anti-EGFR monoclonal Ab. We tested the capture Ab and proper functioning of the fluoroimmunoassay using purified samples of EGFR at various titrations. The capture and detection Ab used in this assay bound to different epitopes of the extracellular domain of EGFR. Figure 5.7(a) shows a fluorescent microscope image of EGFR on the Protein G based microsphere-array platform. We observed a strong positive correlation between fluorescence intensity and EGFR concentration (Fig. 5.7(b)). We further carried out sensitivity studies to determine the limit of detection (LOD) of the assay, using confocal microscopy. The intensity of the fluorescent halo seen surrounding the microsphere was used as a measure of varying EGFR concentration.

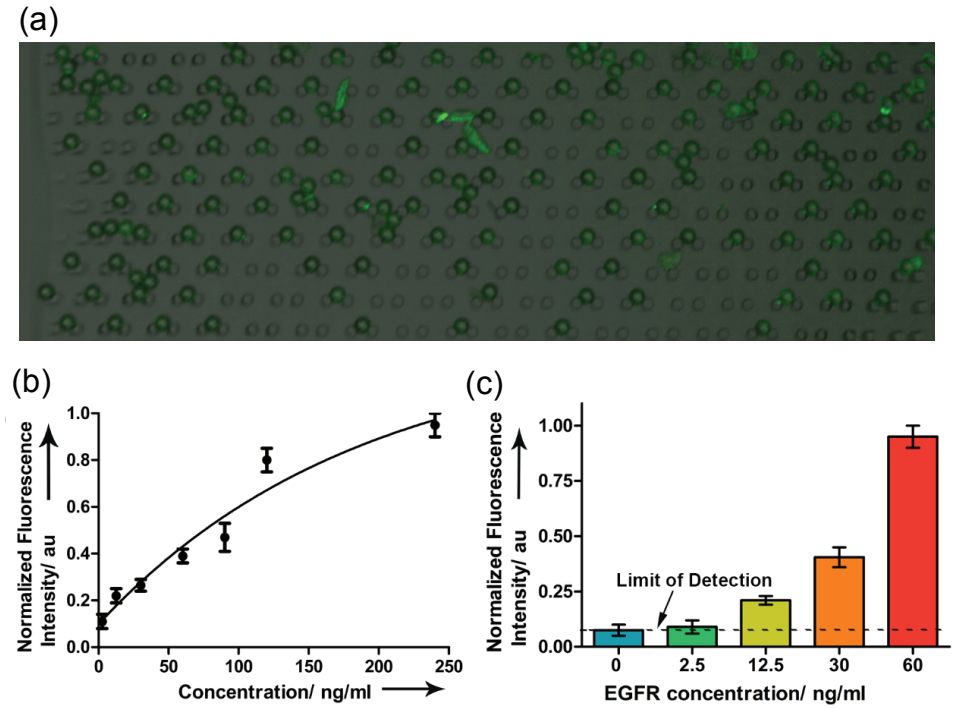

Figure 5.7: Application of our device for sensitivity detection of cancer biomarkers through fluoroimmunoassays. (a) Fluorescent microscope image of EGFR on a Protein G based microsphere-array platform. (b) Fluorescence spectrum shows the response of the assay to increasing concentrations of EGFR. (c) Sensitivity of the fluoroimmunoassay using purified EGFR defines the limit of detection.

There was no detectable fluorescence at < 12.5 ng/ml EGFR concentration (Fig. 5.7(c)). Based on the results here, more experiments will be carried out to detect the expression pattern of EGFR biomarkers across several tumor types. They will provide an integrated insight into the molecular basis of tumor proliferation in different patients.

5.5 Summary

We developed an analytical framework to build a microfluidic microsphere-trap array device for simultaneous, efficient, and accurate detection of multiple targets in a single channel. We proposed to immobilize microspheres of different sizes at different regions in the channel of the device. These different-sized microspheres capture different targets and further identify

the targets based on their positions. We extended our previous optimization framework for optimal design of this device. To demonstrate our design, we designed a device for trapping microspheres of two different sizes for detection of two types of targets, and validated the design by finite element fluid dynamics simulations. We also fabricated the device and performed microsphere-trapping experiments to evaluate its performance. The results showed that our device achieved position-encoding of the microspheres with high efficiency and few fluidic errors. Thus, the device offers the advantages of easy fabrication, convenient operation, and multiplex and high throughput biological targets detection. We also envision utilizing the device to separate, sort, or enumerate cells, such as circulating tumor cells and blood cells, based on cell size and deformability. Therefore, the device is promising as a cost-effective and point-of-care miniaturized disease diagnostic tool.

Chapter 6

Conclusions and Future Work

In this dissertation, we designed and implemented a novel position-encoded microfluidic microsphere-trap array device. We first provided the statistical design of the position-encoded microsphere arrays, and employed the Ziv-Zakai bound to investigate their performance. We then implemented the arrays, integrated with microfluidic technology. We further developed an analytical framework to optimize the geometry of the arrays for maximized packing density, optimized trapping efficiency, and minimized fluidic errors. We formulated a finite element (FEM) fluid dynamics simulation model for the device, and used it to validate the hydrodynamic trapping mechanism and investigate the trapping of the microspheres. We finally extended our analytical framework to build a optimized device that enables simultaneous, efficient, and accurate screening of multiple biological targets in a single microfluidic channel. In the following, we first summarize the key contributions of this dissertation, and then provide some directions in which this work can be extended.

6.1 Summary of Contributions

We first provided a statistical design for the position-encoded microsphere arrays and analyzed their statistical performance in imaging targets at different signal-to-noise ratio (SNR) levels, especially at low SNR. We computed the Ziv-Zakai bound (ZZB) on the errors in estimating the unknown parameters, including the target concentrations. Through numerical examples, we found the SNR level below which the ZZB provided a more accurate estimation of the error than the posterior Cramér-Rao bound (PCRB) did. We further applied the ZZB to select the optimal design parameters of the device, such as the distance between

the microspheres, and to investigate the effects of the experimental variables, such as the microscope point-spread function. We performed an imaging experiment on microspheres with protein targets that verified the optimal design parameters using the ZZB.

We then implemented the microsphere arrays by employing microfluidic technology and a hydrodynamic trapping mechanism. We designed a novel geometric structure of the device, and developed a comprehensive and robust framework to optimize the values of the geometric parameters to maximize its packing density. We also simultaneously optimized multiple criteria, such as efficiently immobilizing a single microsphere in each trap, effectively eliminating fluidic errors such as channel clogging and multiple microspheres in a trap, minimizing errors in subsequent imaging experiments, and easily recovering targets. We used finite element fluid dynamics simulations to validate the trapping mechanism and to study the effects of the optimization geometric parameters on the packing density. We further performed microsphere-trapping experiments using the optimized device and a device with randomly selected geometric parameters, which we denote as the un-optimized device. These experiments demonstrated easy control of the microspheres' transportation and manipulation in the optimized device. They also showed that the optimized device greatly outperforms the un-optimized device by increasing the packing density by a factor of two, improving the microsphere trapping efficiency from 58% to 99%, and reducing fluidic errors from 48% to a negligible level (less than 1%).

To investigate the hydrodynamic trapping of microspheres in our device, we built a finite element simulation model. The accuracy of the time-dependent simulation of a microsphere's motion towards the traps was validated by our experimental results. Based on the simulations, we studied the fluid velocity field, pressure field, and force and stress on the microsphere in the device. We further explored the trap array's geometric parameters and critical fluid velocity, which affect the microsphere's hydrodynamic trapping. The information is valuable for designing microfluidic devices and guiding experimental operation. Additionally, we provided guidelines on the simulation set-up, and we released an openly available implementation of our simulation in one of the popular FEM softwares, COMSOL Multiphysics. Researchers may tailor the model to simulate similar microfluidic systems to accommodate a variety of structured particles. Therefore, the simulation will be of particular interest to biomedical research involving cell or bead transport and migration, blood flow within microvessels, and drug delivery.

We finally extended our analytical optimization framework to build a microfluidic microsphere-trap array device that enables simultaneous, efficient, and accurate screening of multiple biological targets in a single microfluidic channel. The traps in the channel of the device can immobilize different-sized microspheres at different regions, obeying hydrodynamically engineered trapping mechanism. Different biomolecules can be captured by the receptors on the surfaces of microspheres of different sizes. They are thus detected according to the microspheres' positions, simplifying screening and avoiding target identification errors. To demonstrate the proposition, we built a device for simultaneous detection of two target types, by trapping microspheres of two sizes. We evaluated the device's performance using finite element fluid dynamics simulations and microsphere-trapping experiments. These results validated that the device efficiently achieves position-encoding of the two-sized microspheres with few fluidic errors, providing the promise of utilizing our framework to build devices for simultaneous detection of more targets. We also envision utilizing the device to separate, sort, or enumerate cells, such as circulating tumor cells and blood cells, based on cell size and deformability. Therefore, our device is promising as a cost-effective and point-of-care miniaturized disease diagnostic tool.

6.2 Future Work

In the future, we plan to extend the work in several directions expounded in the following.

6.2.1 Integrating Microsphere-Trap Arrays with Deterministic Lateral Displacement

In the experiments for multiplex detection, we loaded sequentially different-sized microspheres into the device, which achieved high packing density and low fluidic errors. Ideally, if we can mix the microspheres and load them simultaneously into the device, simpler and scalable device operation can be achieved. However, in our preliminary experiments with this approach, we found that it was still challenging to achieve error-free trapping. To achieve simultaneous mixed loading, one promising solution is integrate our hydrodynamic trap arrays with hydrodynamic metamaterials such as deterministic lateral displacement (DLD)

microfabricated post arrays [106], [107]. In the refined device, DLD will first spatially separate different-sized microspheres in the fluid. Then the microspheres will be immobilized at predetermined positions by their corresponding traps.

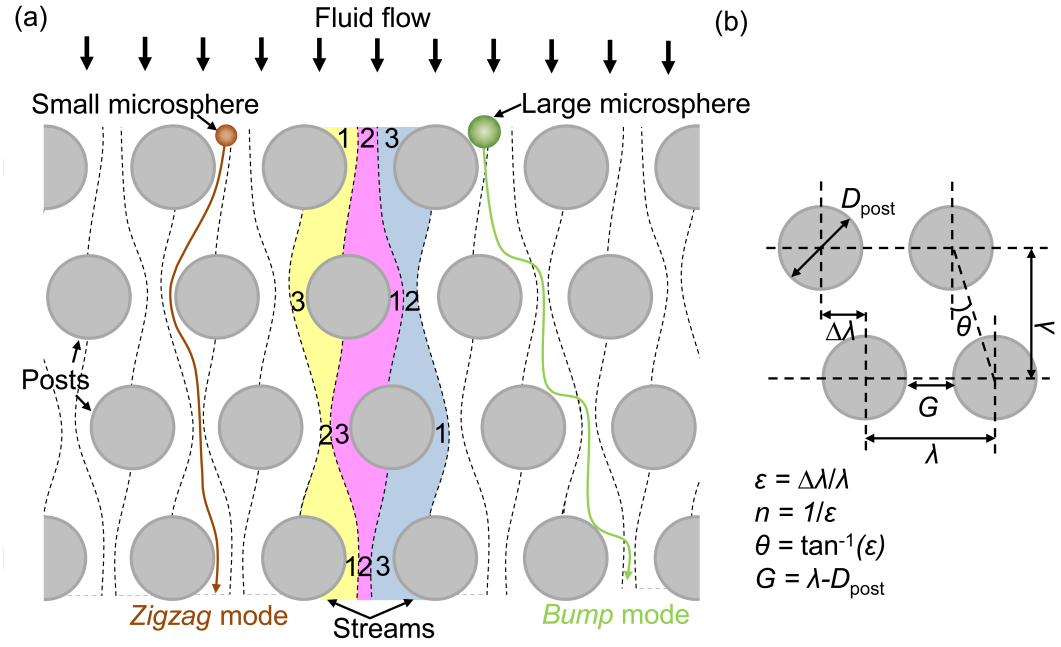

Figure 6.1: Schematic diagram of spatially separating different-sized microspheres by using a deterministic lateral displacement (DLD) micro-post array. (a) The post array is asymmetric. Each subsequent downstream row offsets horizontally with respect to the previous row by $\Delta\lambda$, that is one third of the post-to-post spacing λ, resulting the offset fraction $\varepsilon = 1/3$. The array divides the flow into $n = 1/\varepsilon = 3$ equivalent streams in each gap between the posts. The streams are numbered from 1 to 3, represented by different colors, and are bounded by dashed streamlines. The streams cyclically permute from row to row, and return to the same positions after three rows. Microspheres (green) with radius smaller than the width of the first stream follow the streamlines and weave periodically through the post array in *zigzag* mode. Microspheres (orange) with radius greater than the width of the first stream bump at a post in each subsequent row and are displaced laterally. They follow a deterministic path through the array in *bump* mode. (b) DLD device geometry. The *bump* mode direction is at an angle $\theta = tan^{-1}(\varepsilon)$ to the flow.

The DLD theory works by utilizing the bifurcation mechanism of laminar flow past a periodic array of micro-posts. Figure 6.1 presents a schematic diagram of a DLD micro-post array. The array is asymmetric. Each subsequent downstream row offsets horizontally with respect to the previous row by $\Delta\lambda$, with λ as the distance between the centers of two posts in the

same row and $\varepsilon = \Delta\lambda/\lambda$ as the offset fraction. Then the post array divides the flow into $n = 1/\varepsilon$ different streams in each gap between the posts. For simplicity, we show three streams ($n = 3$) in Fig. 6.1. Each stream carries equal fluid flux and shifts its position cyclically. After n rows each stream returns to its initial position within the gap. In Fig. 6.1(a), the first stream moves to position 3 in the second row, position 2 in the third row after next, and back to position 1 in the fourth row. The first and second streams always bifurcate by a post in the subsequent row. Because the Reynolds number is very low ($\approx 10^{-3}$) in microfluidic devices, there is very little diffusion and mixing between streams. The DLD geometry is denoted in Fig. 6.1(b).

A microsphere in the fluid flow has two possible modes of travel (*zigzag* and *bump*) (Fig. 6.1(a)). If a microsphere's radius is smaller than the width of the first stream, it will follow the streamlines and weave periodically through the post array in *zigzag* mode. If the microsphere's radius is larger than the width of the first stream, the microsphere will be forced to remain in the second or higher numbered streams in every row. It will be bumped at a post in each subsequent row and displaced laterally. Thus it follows a deterministic path through the array in *bump* mode.

A single section of DLD post array achieves bimodal separation of microspheres. That is, microspheres traveling in the array region follow either the *zigzag* mode or the *bump* mode. To separate a range of different-sized microspheres, we will place a number of post array sections after one another, with increasing critical microsphere diameter D_c (D_c is the dividing value between the two travel modes). Therefore, the first post array section separates the smallest microspheres from the other larger ones, the second post array section separates the second smallest ones, and so on. After the DLD arrays, the separated different-sized microspheres are immobilized by their corresponding trap arrays. Figure 6.2 provides a schematic diagram of the integrated DLD and microsphere-trap array device for multiplex biomolecule target detection.

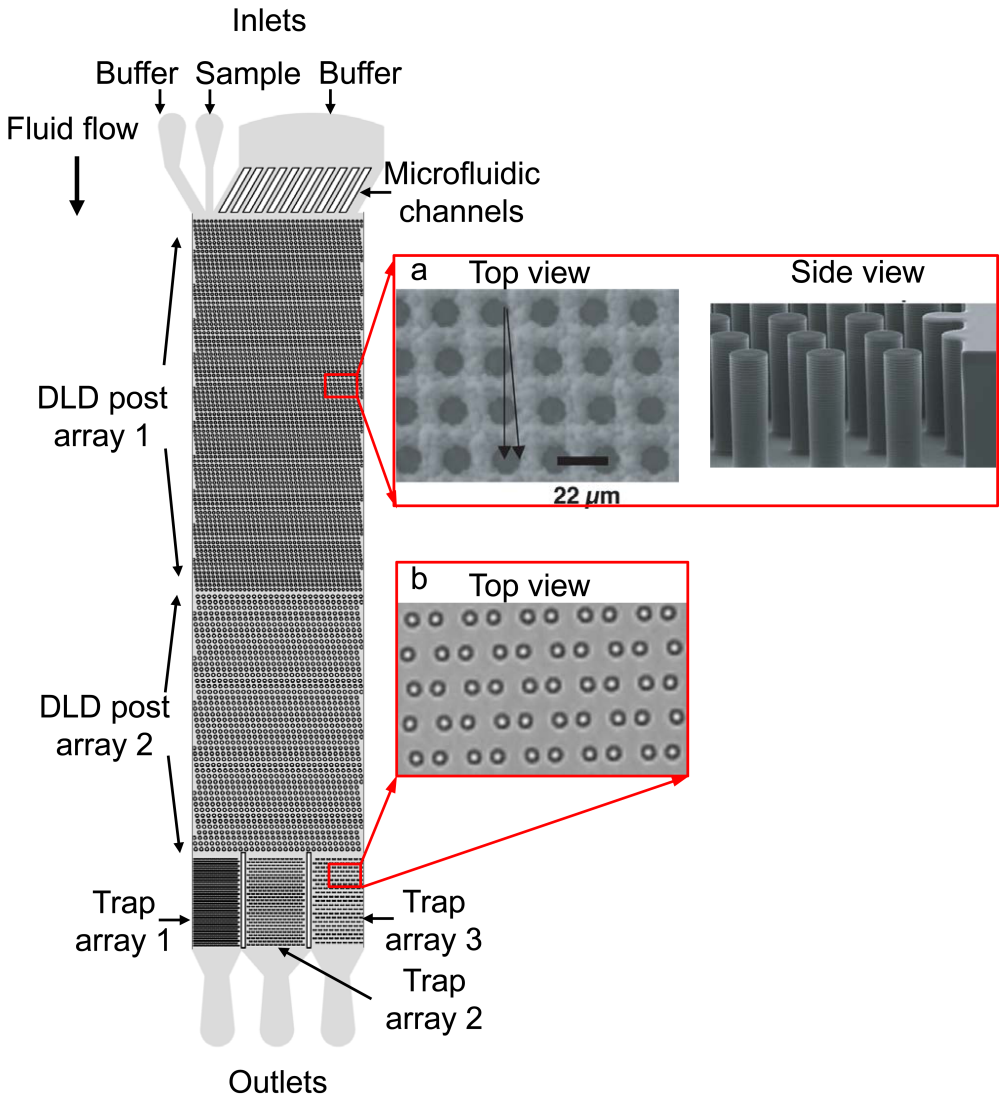

Figure 6.2: Schematic diagram of the integrated deterministic lateral displacement (DLD) and microsphere-trap array device for multiplex biomolecule target detection. The device is designed to separate and trap 10 μm, 15 μm, and 20 μm microspheres. The mixed microsphere sample and buffer are supplied at the inlets. The section of the DLD post array 1 separates the 10 μm microspheres in the *zigzag* mode and the 15 μm and 20 μm microspheres in the *bump* mode. The array 2 further separates the 15 μm microspheres in the *zigzag* mode and the 20 μm microspheres in the *bump* mode. The separated 10 μm, 15 μm, and 20 μm microspheres are immobilized by their corresponding traps at the trap array region 1, 2, and 3, respectively. Inset a shows the top and side views of the DLD post array, with the arrows indicating the vertical and bump directions. Inset b shows the top view of the trap array.

6.2.2 Integrating Finite Element Simulation with Multi-objective Optimization

Multi-objective optimization: In our optimization framework for the microsphere-trap arrays (Chapters 3 and 5), we only considered one optimization objective as maximizing the microspheres' packing density. Typically, a good design involves multiple objectives such as capital cost, operating cost and time, detection quality and recovery of bimolecular targets, efficiency, etc. Therefore, the device design should be measured with respect to multiple objectives. For the integrated device with DLD and hydrodynamic trapping, we will have multiple objectives to be optimized simultaneously, such as:

• maximizing DLD dynamic range, i.e., maximizing number of different-sized microspheres that can be separated. This is essentially the same as maximizing the separation resolution.

• maximizing DLD posts' packing density;

• minimizing the whole DLD structure area;

• minimizing fluidic errors in DLD, such as channel clogging and microspheres in wrong travel modes;

• maximizing trap arrays' packing density;

• maximizing trapping efficiency (the ratio of trapped microspheres over total number of microspheres. This is especially important for the applications of detecting/enumerating tumor or rare cells);

• maximizing *single* and minimizing fluidic errors such as *clogging*, *empty*, and *multiple* that were defined in our previous framework.

These objectives are affected by the device geometric parameters. In mathematical terms, a vector-valued multi-objective optimization problem can be formulated as

$$\min(f_1(\boldsymbol{x}), f_2(\boldsymbol{x}), ..., f_k(\boldsymbol{x})), \quad \text{s.t. } \boldsymbol{x} \in \boldsymbol{X}, \tag{6.1}$$

where $f_j(\boldsymbol{x})$ with $j = 1, ..., k$ (the integer k is the number of objectives) is the objective function, and $\boldsymbol{x}$ is the vector of the geometric parameters. The set $\boldsymbol{X}$ is the feasible set of the geometric vectors, which is typically defined by some constraints like $\mathcal{C}_1 - \mathcal{C}_6$ in our previous optimization in Chapter 3. Note that if an objective function is to be maximized, it is equivalent to minimize its negative.

We denote $\boldsymbol{x}^*$ as a feasible solution to the optimization and $\boldsymbol{z}^* := (f_1(\boldsymbol{x}^*), f_2(\boldsymbol{x}^*), ..., f_k(\boldsymbol{x}^*))$ as an objective vector. In multi-objective optimization, there does not typically exist a single feasible solution that minimizes simultaneously all objective functions. In this case, the objective functions are conflicting, i.e., achieving the optimum value for one objective requires some trade-off on one or more of other objectives. Therefore, there exists Pareto optimal solutions [109]. A solution is called Pareto optimal if none of the objective functions can be improved in value without degrading some of the other objective values. Without additional preference information, all Pareto optimal solutions are considered equally good. The set of Pareto optimal solutions is called the Pareto front. The upper bound of Pareto front is called the nadir objective vector $\boldsymbol{z}_j^{\text{nad}}$ and the lower bound of Pareto front is called the ideal objective vector $\boldsymbol{z}_j^{\text{ideal}}$:

$$\boldsymbol{z}_j^{\text{nad}} := \sup_{\boldsymbol{x}\in\boldsymbol{X} \text{ is Pareto optimal}} f_j(\boldsymbol{x}), \quad \boldsymbol{z}_j^{\text{ideal}} := \inf_{\boldsymbol{x}\in\boldsymbol{X}} f_j(\boldsymbol{x}) \text{ for all } j = 1, ..., k. \tag{6.2}$$

When decision making is emphasized, the objective of solving a multi-objective optimization problem is referred to supporting a decision maker (DM) in finding the most preferred Pareto optimal solution according to his/her preferences [109], [110]. There are different ways to utilize the DM to find the most preferred solution. We will use the interactive methods [110]. In interactive methods, the DM is allowed to iteratively search for the most preferred solution. In each iteration of the interactive method, the DM is shown Pareto optimal solution(s) and describes how the solution(s) could be improved. The information given by the DM is then taken into account while generating new Pareto optimal solution(s) for the DM to study in the next iteration. In this way, the DM learns about the feasibility of his/her wishes and can concentrate on solutions that are interesting to him/her. The DM may stop the search whenever he/she wants to.

Finite element simulation: A major challenge in the multi-objective optimization of the device's microfluidic geometry is the difficulty of finding analytical solutions to the Navier-Stokes equations. Thus conventional optimization methodologies using analytical expressions are difficult to apply. We will integrate FEM simulation as an inherent part of the optimization process to develop a generally applicable microfluidic geometry optimization methodology. To our knowledge, this will be the first attempt to develop and verify such a general optimization methodology which can be applied to any microfluidic systems.

Integrating finite element simulation with multi-objective optimization: To integrate FEM simulation with multi-objective optimization, we will designate the FEM as the DM in the interactive multi-objective optimization method. As the DM, the FEM simulation continuously interacts with iterative analytical solution process to search for the most preferred solution. In other words, at each iteration, the FEM tests what kind of Pareto optimal solutions are attainable for both the analytical objectives and non-analytical objectives, and expresses preferences for these solutions. The detailed steps are:

1. Initialize: calculate ideal and approximated nadir objective vectors and provide them to the FEM simulation.
2. Generate a Pareto optimal starting point by using the global criterion no-preference method of the form [111]:

$$\min \|(f_1(\boldsymbol{x}), f_2(\boldsymbol{x}), ..., f_k(\boldsymbol{x}))^T - \boldsymbol{z}^{\text{ideal}}\| \quad \text{s.t. } \boldsymbol{x} \in \boldsymbol{X}, \tag{6.3}$$

   where $\|\cdot\|$ can be L_1 or L_2 norm [109].
3. Obtain preference information from the FEM simulation, for example, desirable objective function values or number of new solutions to be generated.
4. Generate new Pareto optimal solution(s) according to the preferences and provide it/them and possibly other information about the problem to the FEM simulation.
5. If several solutions were generated, use the FEM to select the best solution so far.
6. Stop, if we want to based on the results of the simulation; otherwise, go to step 3.

We will combine MATLAB's open-ended technical scripting environment and COMSOL's multiphysics modeling platform to implement the interactive FEM-based multi-objective optimization.

6.2.3 Integrated Lab-on-a-chip System

To further reduce the size of the instrument and make it useful, we plan to build on-chip microlenses for the illumination and imaging purposes. We will place the device on top of a

cell phone camera and use an inexpensive blue LED, to excite the fluorescence. This is in contrast to the use of an external microscope and imaging sensors we discussed in Chapter 1. Moreover, we will use the cell phone to verify the test result by sending the microsphere array images to a centralized facility. The whole system should fit within a hand's palm and will be battery powered. The cost of the test should be lower than in existing ones due to inexpensive fabrication, low reagent cost, and testing multiple patients using a single chip. We will finally integrate optical sensing, imaging, and spectroscopic functionalities onto the same microsphere tray array substrate to build a complete lab-on-a-chip system.

6.2.4 Biomedical Experiments and Applications

We will apply our device for more experiments in both fundamental biomedical research and medical diagnostics. We will use the device to perform simultaneous screening and correlation of the expression levels of target DNAs, mRNAs, and proteins in normal and diseased tissues. We will use it to identify specific cells that produce target biomarkers in heterogeneous cell populations in tissue sections. With the potential of being integrated as a hand-held and battery-powered lab-on-a-chip system, we will also use our device to realize a highly sensitive, rapid, and inexpensive disease diagnostic tool for malaria, tuberculosis, etc. We envision other applications such as environmental monitoring, bio-terrorism detection, and self-health testing.

References

[1] R. E. Oosterbroek and A. van den Berg, *Lab-on-a-chip: miniaturized systems for (bio)chemical analysis and synthesis*. Amsterdam: Elsevier B.V., 2003.

[2] V. Srinivasan, V. K. Pamula, and R. B. Fair, "An integrated digital microfluidic lab-on-a-chip for clinical diagnostics on human physiological fluids," *Lab Chip*, vol. 4, pp. 310–315, May 2004.

[3] I.-F. Cheng, H.-C. Chang, D. Hou, and H.-C. Chang, "An integrated dielectrophoretic chip for continuous bioparticle filtering, focusing, sorting, trapping, and detecting," *Biomicrofluidics*, vol. 1, p. 021503, May 2007.

[4] M. Schena, D. Shalon, R. W. Davis, and P. O. Brown, "Quantitative monitoring of gene expression patterns with a complementary DNA microarray," *Science*, vol. 270, pp. 467–470, Oct. 1995.

[5] P. O. Brown and D. Botstein, "Exploring the new world of the genome with dna microarrays," *Nat. Genet.*, vol. 21, pp. 33–27, Jan. 1999.

[6] S. Senapati, A. R. Mahon, J. Gordon, C. Nowak, S. Sengupta, T. H. Powell, J. Feder, D. M. Lodge, and H.-C. Chang, "Rapid on-chip genetic detection microfluidic platform for real world applications," *Biomicrofluidics*, vol. 3, p. 022407, May 2009.

[7] K. O'Donnell, B. A. J. Sarver, M. Brandt, D. C. Chang, J. N. Wang, B. J. Park, D. A. Sutton, L. Benjamin, M. Lindsley, A. Padhye, D. M. Geiser, and T. J. Ward, "Phylogenetic diversity and microsphere array-based genotyping of human pathogenic Fusaria, including isolates from the multistate contact lens-associated U.S. keratitis outbreaks of 2005 and 2006," *J. Clin. Microbiol.*, vol. 45, pp. 2235–2248, Jul. 2007.

[8] M. B. Meza, "Bead-based HTS applications in drug discovery," *Drug Discov. Today*, vol. 1, pp. 38–41, Jun. 2000.

[9] N. Bontoux, L. Dauphinot, T. Vitalis, V. Studer, Y. Chen, J. Rossier, and M.-C. Potier, "Integrating whole transcriptome assays on a lab-on-a-chip for single cell gene profiling," *Lab Chip*, vol. 8, pp. 443–450, Jan. 2008.

[10] D. R. Walt, "Bead-based fiber-optic arrays," *Science*, vol. 287, pp. 451–452, Jan. 2000.

[11] A. Mathur, "Image analysis of ultra-high density, multiplexed, microsphere-based assays," Ph.D. dissertation, Northwestern Univ., Chicago, Sep. 2006.

[12] P. Sarder and A. Nehorai, "Statistical design of position-encoded microsphere arrays," *IEEE Trans. Nanobiosci.*, vol. 10, pp. 16–29, Mar. 2011.

[13] X. Xu, P. Sarder, and A. Nehorai, "Statistical design of position-encoded microsphere arrays at low target concentrations," in *Proc. 45 Asilomar Conf. Signals, Syst. Comput.*, Pacific Grove, CA, USA, Nov. 2011, pp. 1694–1698.

[14] J. G. McNally, T. Karpova, J. Cooper, and J. A. Conchello, "Three-dimensional imaging by deconvolution microscopy," *Methods*, vol. 19, pp. 373–385, May 1999.

[15] H. T. M. van der Voort and K. C. Strasters, "Restoration of confocal images for quantitative image analysis," *J. Microsc.*, vol. 178, pp. 165–181, May 1995.

[16] K. L. Gunderson, S. Kruglyak, M. S. Graige, E. Wickham, J. Bierle, D. Doucet, M. Milewski, R. Yang, C. Siegmund, J. Haas, L. Zhou, and M. S. Chee, "Decoding randomly ordered DNA arrays," *Genome Res.*, vol. 14, pp. 870–877, Apr. 2004.

[17] P. Sarder and A. Nehorai, "Estimating locations of quantum-dot encoded microparticles from ultra-high density 3D microarrays," *IEEE Trans. Nanobiosci.*, vol. 7, pp. 284–297, Jan. 2008.

[18] K. D. Bake and D. R. Walt, "Multiplexed spectroscopic detections," *Annu. Rev. Anal. Chem.*, vol. 1, pp. 15–47, Jul. 2008.

[19] X. Xu, P. Sarder, N. Kotagiri, S. Achilefu, and A. Nehorai, "Performance analysis and design of position-encoded microsphere arrays using the Ziv-Zakai bound," *IEEE Trans. Nanobiosci.*, vol. 12, pp. 29–40, Mar. 2013.

[20] H. Lyng, A. Badiee, E. Hovig, O. Myklebost, and T. Stokke, "Profound influence of microarray scanner characteristics on gene expression ratios: analysis and procedure for correction," *BMC Genomics*, vol. 3, pp. 5–10, Feb. 2004.

[21] S. P. A. Fodor, J. L. Read, M. C. Pirrung, L. Stryer, A. T. Lu, and S. Dennis, "Light-directed, spatially addressable parallel chemical synthesis," *Science*, vol. 251, pp. 767–773, Feb. 1991.

[22] A. Oliphant, D. L. Barker, J. R. Stuelpnagel, and M. S. Chee, "Beadarray technology: enabling an accurate, cost-effective approach to high-throughput genotyping," *Biotechniques*, vol. 32, pp. 56–58, Jun. 2002.

[23] C. Situma, M. Hashimoto, and S. A. Soper, "Merging microfluidics with microarray-based bioassays," *Biomol. Eng.*, vol. 23, p. 213231, Oct. 2006.

[24] W. H. Tan and S. Takeuchi, "A trap-and-release integrated microfluidic system for dynamic microarray applications," *Proc. Natl. Acad. Sci. U.S.A.*, vol. 104, pp. 1146–1151, Jan. 2007.

[25] W. Xu, K. Sur, H. Zeng, A. Feinerman, D. Kelso, and J. B. Ketterson, "A microfluidic approach to assembling ordered microsphere arrays," *J. Micromech. Microeng.*, vol. 18, p. 075027, Jun. 2008.

[26] R. H. Liu, K. Dill, H. S. Fuji, and A. McShea, "Integrated microfluidic biochips for DNA microarray analysis," *Expert Rev. Mol. Diagn.*, vol. 6, pp. 253–261, Mar. 2006.

[27] A. Karimi, S. Yazdi, and A. M. Ardekani, "Hydrodynamic mechanisms of cell and particle trapping in microfluidics," *Biomicrofluidics*, vol. 7, p. 021501, Apr. 2013.

[28] D. Erickson, "Towards numerical prototyping of labs-on-chip: modeling for integrated microfluidic devices," *Microfluid. Nanofluid.*, vol. 1, pp. 301–318, Oct. 2005.

[29] P. Roy, N. K. Anand, and D. Banerjee, "Numerical simulation of flow and heat transfer in radially rotating microchannels," *Microfluid. Nanofluid.*, vol. 15, pp. 397–413, Sep. 2013.

[30] W. H. Grover, R. H. Ivester, E. C. Jensen, and R. A. Mathies, "Development and multiplexed control of latching pneumatic valves using microfluidic logical structures," *Lab Chip*, vol. 6, pp. 623–631, May 2006.

[31] M. A. Unger, H. P. Chou, T. Thorsen, A. Scherer, and S. R. Quake, "Monolithic microfabricated valves and pumps by multilayer soft lithography," *Science*, vol. 288, pp. 113–116, Apr. 2000.

[32] S. Bohm, G. J. Burger, M. T. Korthorst, and F. Roseboom, "A micromachined silicon valve driven by a miniature bi-stable electro-magnetic actuator," *Sensor Actuat. A-Phys.*, vol. 80, pp. 77–83, Mar. 2000.

[33] M. Capanu, J. G. Boyd, and P. J. Hesketh, "Design, fabrication, and testing of a bistable electromagnetically actuated microvalve," *J. Microelectromech. Syst.*, vol. 9, pp. 181–189, Jun. 2000.

[34] R. Pal, M. Yang, B. N. Johnson, D. T. Burke, and M. A. Burns, "Phase change microvalve for integrated devices," *Anal. Chem.*, vol. 76, pp. 3740–3748, Jun. 2004.

[35] Z. Li and D. Psaltis, "Optofluidic distributed feedback dye lasers," *IEEE J. Sel. Topics Quantum Electron.*, vol. 13, pp. 185 – 193, Apr. 2007.

[36] R. Klemm, N. Hlawatsch, T. E. Hansen-Hagge, H. Becker, and C. Gartner, "Magnetic particle-based sample-prep and valveing in microfluidics," in *Proc. of SPIE 8251*, San Francisco, CA, USA, Mar. 2012, p. 825108.

[37] H. L. van Trees, *Detection, estimation and modulation theory.* New York: John Wiley, 1968.

[38] J. A. Ferguson, F. J. Steemers, and D. R. Walt, "High-density fiber-optic DNA random microsphere array," *Anal. Chem.*, vol. 72, pp. 5618–5624, Nov. 2000.

[39] S. C. White and N. C. Beaulieu, "On the application of the Cramér-Rao and detection theory bounds to mean square error of symbol timing recovery," *IEEE Trans. Commun.*, vol. 40, pp. 1635–1643, Oct. 1992.

[40] K. L. Bell, Y. Steinberg, Y. Ephraim, and H. L. van Trees, "Extended Ziv-Zakai lower bound for vector parameter estimation," *IEEE Trans. Inf. Theory*, vol. 43, pp. 624–637, Mar. 1997.

[41] S. F. Gibson and F. Lanni, "Experimental test of an analytical model of aberration in an oil-immersion objective lens used in three-dimensional light microscopy," *J. Opt. Soc. Am. A*, vol. 8, pp. 1601–1613, Oct. 1999.

[42] B. Zhang, J. Zerubia, and J. Olivo-Marin, "Gaussian approximations of fluorescence microscope point-spread function models," *Appl. Opt.*, vol. 46, pp. 1819–1829, Mar. 2007.

[43] P. Sarder and A. Nehorai, "Deconvolution methods for 3-D fluorescence microscopy images," *IEEE Signal Process. Mag.*, vol. 23, pp. 32–45, Nov. 2006.

[44] T. J. Fellers and M. W. Davidson, "CCD noise sources and signal-to-noise ratio," http://learn.hamamatsu.com/articles/ccdsnr.html, 2008.

[45] V. Gruev, Z. Yang, and J. V. der Spiegel, "Current mode image sensor with two transistors per pixel," *IEEE Trans. Circuits Syst. I*, vol. 57, pp. 1154–1165, Jun. 2010.

[46] T. M. Jovin and D. J. Arndt-Jovin, "Luminescence digital imaging microscopy," *Annu. Rev. Biophys. Biophys. Chem.*, vol. 18, pp. 271–308, Sep. 1989.

[47] J. Ohta, *Smart CMOS image sensors and applications.* Boca Raton: CRC Press, 2007.

[48] M. Christenson, "The application of scientific grade CCD cameras to biological imaging," *Imaging Neurons: A Laboratory Manual*, pp. 23–32, 2000.

[49] B. Huang, M. Bates, and X. Zhuang, "Super-resolution fluorescence microscopy," *Annu. Rev. Biochem.*, vol. 78, pp. 993–1016, Apr. 2009.

[50] H. M. Wyss, D. L. Blair, J. F. Morris, H. A. Stone, and D. A. Weitz, "Mechanism for clogging of microchannels," *Phys. Rev. E*, vol. 74, p. 061402, Dec. 2006.

[51] B. J. Kirby, *Micro- and nanoscale fluid mechanics: transport in microfluidic devices*. Cambridge: Cambridge University Press, 2010.

[52] H. Bruus, *Theoretical Microfluidics*. Oxford: Oxford University Press, 2008.

[53] J. C. McDonald and G. M. Whitesides, "Poly(dimethylsiloxane) as a material for fabricating microfluidic devices," *Acc. Chem. Res.*, vol. 35, p. 491499, Apr. 2002.

[54] F. M. White, *Fluid mechanics*. New York: McGraw-Hill, 2002.

[55] F. S. Manning and R. E. Thompson, *Natural gas*. Tulsa: PennWell Books, 1991.

[56] S. A. Campbell, *The science and engineering of microelectronic fabrication*. Oxford: Oxford University Press, 2001.

[57] G. B. Dantzig and M. N. Thapa, *Linear programming 2: theory and extensions*. New York: Springer-Verlag, 2003.

[58] T. G. Kolda, R. M. Lewis, and T. Virginia, "Optimization by direct search: new perspectives on some classical and modern methods," *SIAM Rev.*, vol. 45, pp. 1–98, Aug. 2003.

[59] COMSOL, "See the link for the software description and application," http://www.comsol.com/, 2008.

[60] X. Xu, P. Sarder, Z. Li, and A. Nehorai, "Follow the link to see the illustrative videos showing how the microspheres are being trapped," http://www.ese.wustl.edu/~nehorai/research/molec_imaging/optimization.html, 2013.

[61] T. Thorsen, S. J. Maerkl, and S. R. Quake, "Microfluidic large-scale integration," *Science*, vol. 298, pp. 580–584, Oct. 2002.

[62] H. W. Hou, H. Y. Gan, A. A. S. Bhagat, L. D. Li, C. T. Lim, and J. Han, "A microfluidics approach towards high-throughput pathogen removal from blood using margination," *Biomicrofluidics*, vol. 6, p. 024115, May 2012.

[63] C. Wang, S. V. Jalikop, and S. Hilgenfeldt, "Efficient manipulation of microparticles in bubble streaming flows," *Biomicrofluidics*, vol. 6, p. 012801, Mar. 2012.

[64] R. J. Yang, H. H. Hou, Y. N. Wang, C. H. Lin, and L. M. Fu, "A hydrodynamic focusing microchannel based on micro-weir shear lift force," *Biomicrofluidics*, vol. 6, p. 034110, Aug. 2012.

[65] G. K. Kurup and A. S. Basu, "Field-free particle focusing in microfluidic plugs," *Biomicrofluidics*, vol. 6, p. 022008, Apr. 2012.

[66] G. M. Whitesides, "The origins and the future of microfluidics," *Nature*, vol. 442, pp. 368–373, Jul. 2006.

[67] D. Janasek, J. Franzke, and A. Manz, "Scaling and the design of miniaturized chemical-analysis systems," *Nature*, vol. 442, pp. 374–380, Jul. 2006.

[68] P. Yager, T. Edwards, E. Fu, K. Helton, K. Nelson, M. R. Tam, and B. H. Weigl, "Microfluidic diagnostic technologies for global public health," *Nature*, vol. 442, pp. 412–418, Jul. 2006.

[69] J. M. Schwenk and P. Nilsson, "Antibody suspension bead arrays," *Methods Mol. Biol.*, vol. 723, pp. 29–36, Jan. 2011.

[70] S. Sugiura, T. Oda, Y. Izumida, Y. Aoyagi, M. Satake, A. Ochiai, N. Ohkohchi, and M. Nakajima, "Size control of calcium alginate beads containing living cells using micro-nozzle array," *Biomaterials*, vol. 26, p. 33273331, Jun. 2005.

[71] Q. Guo, S. J. Reiling, P. Rohrbach, and H. Ma, "Microfluidic biomechanical assay for red blood cells parasitized by Plasmodium falciparum," *Lab Chip*, vol. 12, pp. 1143–1150, Feb. 2012.

[72] J. W. Choi, K. W. Oh, J. H. Thomas, W. R. Heineman, H. B. Halsall, J. H. Nevin, A. J. Helmicki, H. T. Henderson, and C. H. Ahn, "An integrated microfluidic biochemical detection system for protein analysis with magnetic bead-based sampling capabilities," *Lab Chip*, vol. 2, pp. 27–30, Dec. 2002.

[73] M. Grumann, A. Geipel, L. Riegger, R. Zengerle, and J. Ducree, "Batch-mode mixing on centrifugal microfluidic platforms," *Lab Chip*, vol. 5, pp. 560–565, Apr. 2005.

[74] P. Roos and C. D. Skinner, "A two bead immunoassay in a micro fluidic device using a flat laser intensity profile for illumination," *Analyst*, vol. 128, pp. 527–531, Apr. 2003.

[75] T. Kulrattanarak, R. G. M. Sman, C. G. P. H. Schroen, and R. M. Boom, "Analysis of mixed motion in deterministic ratchets via experiment and particle simulation," *Microfluid. Nanofluid.*, vol. 10, pp. 843–853, Apr. 2011.

[76] P. S. Dittrich and P. Schwille, "An integrated microfluidic system for reaction, high-sensitivity detection, and sorting of fluorescent cells and particles," *Anal. Chem.*, vol. 75, p. 57675774, Sep. 2003.

[77] P. T. Lv, Z. W. Tang, X. J. Liang, M. Z. Guo, and R. P. S. Han, "Spatially gradated segregation and recovery of circulating tumor cells from peripheral blood of cancer patients," *Biomicrofluidics*, vol. 7, p. 034109, Jun. 2013.

[78] H. S. Moon, K. Kwon, K. A. Hyun, T. S. Sim, J. C. Park, J. G. Lee, and H. I. Jung, "Continual collection and re-separation of circulating tumor cells from blood using multi-stage multi-orifice flow fractionation," *Biomicrofluidics*, vol. 7, p. 014105, Jan. 2013.

[79] I. Cima, C. W. Yee, F. S. Iliescu, W. M. Phyo, K. H. Lim, C. Iliescu, and M. H. Tan, "Label-free isolation of circulating tumor cells in microfluidic devices: current research and perspectives," *Biomicrofluidics*, vol. 7, p. 011810, Jan. 2013.

[80] X. Xu, P. Sarder, Z. Li, and A. Nehorai, "Optimization of microfluidic microsphere-trap arrays," *Biomicrofluidics*, vol. 7, p. 014112, Feb. 2013.

[81] D. D. W. Pepper and J. C. Heinrich, *The finite element method: basic concepts and applications*. Florence: Hemisphere Publishing Corporation, 1992.

[82] X. Xu, Z. Li, and A. Nehorai, "Follow the link to download the finite elemtn fluid dynamics simulation model," http://www.ese.wustl.edu/~nehorai/research/molec_imaging/COMSOL_simulation_model_of_a_microfluidic_system.mph, 2013.

[83] A. F. Bower, *Applied mechanics of solid*. Florence: Taylor and Francis, 2011.

[84] M. Souli and D. J. Benson, *Arbitrary lagrangian eulerian and fluid-structure interaction: numerical simulation*. Hoboken: Wiley, 2013.

[85] X. Xu, Z. Li, N. Kotagiri, P. Sarder, S. Achilefu, and A. Nehorai, "Microfluidic microsphere-trap arrays for simultaneous detection of multiple targets," in *Proc. of SPIE 8615*, San Francisco, CA, USA, Mar. 2013, p. 861533.

[86] S. V. Patankar, *Numerical heat transfer and fluid flow*. Bristol: Hemisphere Pub. Corp., 1980.

[87] P. M. Knupp, "Winslow smoothing on two-dimensional unstructured meshes," in *Proc. of the Seventh International Meshing Roundtable*, Park City, UT, USA, Mar. 1998, pp. 449–457.

[88] N. Triantafyllidis and E. C. Aifantis, "A gradient approach to localization of deformation. i. hyperelastic materials," *J. Elasticity*, vol. 16, pp. 225–237, Sep. 1986.

[89] E. R. D. Oliveira, "On the accuracy of finite difference solutions to elliptic partial differential equations," *Int. J. Numer. Methods Eng.*, vol. 21, p. 229238, Feb. 1985.

[90] C. K. W. Tam and K. A. Kurbatskii, "Multi-size-mesh multi-time-step dispersion-relation-preserving scheme for multiple-scales aeroacoustics problems," *Int. J. Comput. Fluid Dyn.*, vol. 17, pp. 119–132, Sep. 2003.

[91] J. N. Shadid, R. S. Tuminaro, and H. F. Walker, "An inexact Newton method for fully coupled solution of the NavierStokes equations with heat and mass transport," *J. Comput. Phys.*, vol. 137, p. 155185, Oct. 1997.

[92] X. Xu, Z. Li, and A. Nehorai, "Follow the link to see the videos showing one of the experiment and one of the simulation of the one-microsphere trapping process," http://www.ese.wustl.edu/~nehorai/research/molec_imaging/FEM.html, 2013.

[93] F. A. Leckie and D. J. D. Bello, *Strength and stiffness of engineering systems.* Limited: Springer London, 2009.

[94] C. D. Eggleton and A. S. Popel, "Large deformation of red blood cell ghosts in a simple shear flow," *Phys. Fluids*, vol. 10, p. 18341846, Apr. 1998.

[95] J. H. Jeong, Y. Sugii, M. Minamiyama, and K. Okamoto, "Measurement of RBC deformation and velocity in capillaries in vivo," *Microvasc. Res.*, vol. 71, p. 212217, May 2006.

[96] J. R. Epstein, A. P. Leung, K. H. Lee, and D. R. Walt, "High-density, microsphere-based fiber optic DNA microarrays," *Biosens. Bioelectron.*, vol. 18, p. 541546, May 2003.

[97] R. M. Dorazio and J. A. Royle, "Mixture models for estimating the size of a closed population when capture rates vary among individuals," *Biometrics*, vol. 59, pp. 351–364, Jun. 2006.

[98] S. Rodiger, P. Schierack, A. Bohm, J. Nitschke, I. Berger, U. Frommel, C. Schmidt, M. Ruhland, I. Schimke, D. Roggenbuck, W. Lehmann, and C. Schroder, "A highly versatile microscope imaging technology platform for the multiplex real-time detection of biomolecules and autoimmune antibodies," *Adv. Biochem. Eng. Biotechnol.*, vol. 133, pp. 35–74, Oct. 2013.

[99] W. J. Rhee and G. Bao, "Simultaneous detection of mRNA and protein stem cell markers in live cells," *BMC Biotechnol.*, vol. 9, pp. 30–39, Apr. 2009.

[100] S. J. Tan, L. Yobas, G. Y. Lee, C. N. Ong, and C. T. Lim, "Microdevice for the isolation and enumeration of cancer cells from blood," *Biomed. Microdevices.*, vol. 11, pp. 883–892, Aug. 2009.

[101] J. D. Chen, D. Chen, T. Yuan, Y. Xie, and X. Chen, "A microfluidic chip for direct and rapid trapping of white blood cells from whole blood," *Biomicrofluidics*, vol. 7, p. 034106, Jun. 2013.

[102] A. Shapiro and A. Philpott. (2007, Mar.) A tutorial on stochastic programming. TutorialSP.pdf. [Online]. Available: http://www2.isye.gatech.edu/people/faculty/Alex_Shapiro/

[103] J. Rice, *Mathematical statistics and data analysis.* Farmington Hills: Duxbury Press, 1995.

[104] X. Xu, Z. Li, and A. Nehorai, "Finite element simulations of hydrodynamic trapping in microfluidic particle-trap array systems," *Biomicrofluidics*, vol. 7, p. 054108, Sep. 2013.

[105] X. Xu, Z. Li, P. Sarder, N. Kotagiri, and A. Nehorai, "Follow the link to see the videos showing the trapping processes of the small microspheres into the small trap region and the large microspheres into the large trap regions," http://www.ese.wustl.edu/~nehorai/research/molec_imaging/twosize.html, 2014.

[106] L. R. Huang, E. C. Cox, R. H. Austin, and J. C. Sturm, "Continuous particle separation through deterministic lateral displacement," *Science*, vol. 304, pp. 987–990, May 2004.

[107] K. J. Morton, K. Loutherback, D. W. Inglis, O. K. Tsui, J. C. Sturm, S. Y. Chou, and R. H. Austin, "Hydrodynamic metamaterials: Microfabricated arrays to steer, refract, and focus streams of biomaterials," *Proc. Natl. Acad. Sci. U. S. A.*, vol. 105, pp. 7434–7438, May 2008.

[108] R. I. Nicholson, J. M. Gee, and M. E. Harper, "EGFR and cancer prognosis," *Eur. J. Cancer*, vol. 37, pp. Suppl 4:S9–15, Sep. 2001.

[109] K. Miettinen, *Nonlinear multiobjective optimization.* Boston: Kluwer Academic Publishers, 1999.

[110] J. Branke, K. Deb, K. Miettinen, and R. Slowinski, "Interactive and evolutionary approaches," in *Multiobjective Optimization.* New York: Springer-Verlag Berlin Heidelberg, 2008.

[111] C. L. Hwang and A. S. M. Masud, *Multiple objective decision making, methods and applications: a state-of-the-art survey.* New York: Springer-Verlag Berlin Heidelberg, 1979.

Appendix A

Estimation of Microscope Gaussian PSF Variances σ_1^2 and σ_2^2

The parameters σ_1^2 and σ_2^2 in the Gaussian microscope PSF model $h(x, y, z)$ (2.4) can be obtained by the least-square estimates of Gibson and Lanni's PSF.

Gibson and Lanni's PSF model is given by

$$\tilde{h}(x, y, z; \boldsymbol{\psi}) = \left| \int_0^1 J_0 \left(\frac{K \mathrm{NA} \rho \sqrt{x^2 + y^2}}{M_{\mathrm{obj}}} \right) \exp \{ jK\phi(z, \boldsymbol{\psi}) \} \rho \mathrm{d}\rho \right|^2, \tag{A-1}$$

where J_0 is a Bessel function of the first kind, K is the wavenumber of the emission wavelength λ_{em}, NA the numerical aperture of the microscope, M_{obj} is the magnification of the lens, j is the square root of -1, and $\phi(\cdot)$ is the phase aberration. ρ denotes the normalized radius in the back focal plane, and z is the distance from the in-focus plane to the point of evaluation. The vector $\boldsymbol{\psi}$ denotes the experimental parameters, i.e., the refractive index of the immersion medium (n_{m}), of the coverslip (n_{c}), and of the specimen (n_{s}), and the thicknesses of the immersion medium (t_{m}), of the coverslip (t_{c}), of the specimen (t_{s}). Other parameters include the optical tube length (OTL), the microscope pinhole size, the excitation wavelength λ_{ex}, the xyz dimensions, the image resolution Δx, Δy, and the image spacing Δz. The values of the experimental parameters in the PSF estimation are summarized in Table 2.2, and are the same as in the imaging experiment (Section 2.5).

To estimate σ_1^2 and σ_2^2, Gibson and Lani's PSF is first generated by the COSMOS software package [A1], with known experimental parameters (Table 2.2). The generated PSF

is applied to distort a spherical illuminating source $\boldsymbol{s}$, and COSMOS outputs the distorted measurements $\boldsymbol{g}$. The spherical source $\boldsymbol{s}$ is of diameter $D = 4\Delta x$ and has a uniform intensity level $\theta = 1$. We define the vector form of $h(x, y, z)$ as $\boldsymbol{h}$, and we have $\boldsymbol{g} = \boldsymbol{s} \otimes \boldsymbol{h}$; the PSF variances σ_1^2 and σ_2^2 are obtained by least-square estimation.

References

[A1] E. Valdimarsson and C. Preza, "Computational optical sectioning microscopy open source (COSMOS) software package," `http://cirl.memphis.edu/cosmos`, 2011.

Appendix B

Estimation of B_1 and B_2

The parameters B_1 and B_2 can be estimated from the imaging experiment. Recall that B_1 and B_2 relate to the noise levels $\sigma_{\mathrm{d}}^2(T)$ and $\sigma_{\mathrm{t}}^2(T)$ of the dark noise w_{d} and the thermal noise w_{t} (2.7). w_{d} and w_{t} together contribute to the background noise. We first estimate the total background noise level σ_{b}^2. Namely, we select several noise-only sections of the z-stack images in the imaging experiment (e.g., the dashed rectangle sections in Fig. 2.8), and compute the variance of the intensities in these sections. We denote the variance as the background noise level $\hat{\sigma}_{\mathrm{b}}^2$. Then the dark and thermal noises are $\hat{\sigma}_{\mathrm{d}}^2(T) = c\hat{\sigma}_{\mathrm{b}}^2$ and $\hat{\sigma}_{\mathrm{t}}^2(T) = (1-c)\hat{\sigma}_{\mathrm{b}}^2$, with $c \in [0, 1]$ denoting the proportion of dark noise in the background noise. The value of c is assumed to be 0.5 at $T_0 = 25$ °C [44]. Having $\hat{\sigma}_{\mathrm{d}}^2(T_0)$ and $\hat{\sigma}_{\mathrm{t}}^2(T_0)$, $\hat{B}_1$ and $\hat{B}_2$ are computed subsequently:

$$\hat{B}_1 = \frac{\hat{\sigma}_{\mathrm{d}}^2(T)}{\exp(-E_g/2k_{\mathrm{B}}T_0)}, \quad \hat{B}_2 = \frac{\hat{\sigma}_{\mathrm{t}}^2(T)}{k_{\mathrm{B}}T_0}. \tag{B-1}$$

Fitting $\hat{B}_1$ and $\hat{B}_2$ into (2.7), we can study the effect of T on the device's performance.

Appendix C

Derivation of $P_{\min}(\boldsymbol{\eta}, \boldsymbol{\eta}+\boldsymbol{e})$

In the numerical computation of the ZZB (2.12), we derive $P_{\min}(\boldsymbol{\eta}, \boldsymbol{\eta}+\boldsymbol{e})$ for the log-likelihood ratio (LLR) test in (2.13) and (2.16) as follows.

First, for the i-th element $g(i)$ in the $KLM \times 1$-dimensional vector measurement $\boldsymbol{g}$ (2.10), we rewrite $\tilde{s}(i)$ as $\boldsymbol{s}'(i)\boldsymbol{\theta}$, where $\boldsymbol{\theta} = [\theta_1, \theta_2]^T$, and $\boldsymbol{s}'(i) = [s'_1(i), s'_2(i)]$ with $s'_1(i) = \partial\tilde{\boldsymbol{s}}(i)/\partial\theta_1$ and $s'_2(i) = \partial\tilde{\boldsymbol{s}}(i)/\partial\theta_2$. Moreover, for convenience, we let $\sigma_{\mathrm{b}}^2 = \sigma_{\mathrm{d}}^2 + \sigma_{\mathrm{t}}^2$. The distribution of the element $g(i)$ then becomes

$$g(i) \sim \mathcal{N}(\boldsymbol{s}'(i)\boldsymbol{\theta}, \frac{\boldsymbol{s}'(i)\boldsymbol{\theta}}{\beta} + \sigma_{\mathrm{b}}^2). \tag{C-1}$$

The distribution of $\boldsymbol{g}$ is

$$\boldsymbol{g} \sim \mathcal{N}(\boldsymbol{S}'\boldsymbol{\theta}, \frac{\mathrm{diag}(\boldsymbol{S}'\boldsymbol{\theta})}{\beta} + \sigma_{\mathrm{b}}^2\boldsymbol{I}). \tag{C-2}$$

From the hypothesis test (2.13), $\boldsymbol{\theta} = \boldsymbol{\eta}$ for $\mathcal{H}_0$ and $\boldsymbol{\theta} = \boldsymbol{\eta} + \boldsymbol{e}$ for $\mathcal{H}_1$, so the distributions of $\boldsymbol{g}$ under $\mathcal{H}_0$ and $\mathcal{H}_1$ are

$$\begin{aligned} p_{\boldsymbol{g}|\boldsymbol{\theta}}(\boldsymbol{g}|\mathcal{H}_0) &= \frac{1}{(2\pi)^{\frac{KLM}{2}}|\Sigma_{\boldsymbol{g}|\mathcal{H}_0}|^{\frac{1}{2}}} \cdot \exp\{-\frac{1}{2}(\boldsymbol{g} - \boldsymbol{S}'\boldsymbol{\eta})^T\Sigma_{\boldsymbol{g}|\mathcal{H}_0}^{-1}(\boldsymbol{g} - \boldsymbol{S}'\boldsymbol{\eta})\}, \\ p_{\boldsymbol{g}|\boldsymbol{\theta}}(\boldsymbol{g}|\mathcal{H}_1) &= \frac{1}{(2\pi)^{\frac{KLM}{2}}|\Sigma_{\boldsymbol{g}|\mathcal{H}_1}|^{\frac{1}{2}}} \cdot \exp\{-\frac{1}{2}(\boldsymbol{g} - \boldsymbol{S}'(\boldsymbol{\eta}+\boldsymbol{e}))^T\Sigma_{\boldsymbol{g}|\mathcal{H}_1}^{-1}(\boldsymbol{g} - \boldsymbol{S}'(\boldsymbol{\eta}+\boldsymbol{e}))\}, \end{aligned} \tag{C-3}$$

where

$$\Sigma_{\boldsymbol{g}|\mathcal{H}_0} = \frac{\mathrm{diag}(\boldsymbol{S}'\boldsymbol{\eta})}{\beta} + \sigma_{\mathrm{b}}^2\boldsymbol{I}, \quad \Sigma_{\boldsymbol{g}|\mathcal{H}_1} = \frac{\mathrm{diag}(\boldsymbol{S}'(\boldsymbol{\eta}+\boldsymbol{e}))}{\beta} + \sigma_{\mathrm{b}}^2\boldsymbol{I}. \tag{C-4}$$

The LLR is expressed as

$$\begin{aligned}\Lambda(\boldsymbol{g},\boldsymbol{\theta}) &= \log\left(p_{\boldsymbol{g}|\boldsymbol{\theta}}(\boldsymbol{g}|\mathcal{H}_1)/p_{\boldsymbol{g}|\boldsymbol{\theta}}(\boldsymbol{g}|\mathcal{H}_0)\right) \\ &= \log\left(\frac{|\Sigma_{\boldsymbol{g}|\mathcal{H}_0}|^{\frac{1}{2}}}{|\Sigma_{\boldsymbol{g}|\mathcal{H}_1}|^{\frac{1}{2}}}\right) - \frac{1}{2}\big((\boldsymbol{g}-\boldsymbol{S}'(\boldsymbol{\eta}+\boldsymbol{e}))^T\Sigma^{-1}_{\boldsymbol{g}|\mathcal{H}_1}(\boldsymbol{g}-\boldsymbol{S}'(\boldsymbol{\eta}+\boldsymbol{e})) \\ &\quad -(\boldsymbol{g}-\boldsymbol{S}'\boldsymbol{\eta})^T\Sigma^{-1}_{\boldsymbol{g}|\mathcal{H}_0}(\boldsymbol{g}-\boldsymbol{S}'\boldsymbol{\eta})\big).\end{aligned} \tag{C-5}$$

We expand the expression of the LLR as

$$\Lambda(\boldsymbol{g},\boldsymbol{\theta}) = \sum_{i=1}^{KLM}\left[\frac{1}{2}\frac{\frac{\boldsymbol{s}'(i)\boldsymbol{e}}{\beta}(g(i)+\beta\sigma_{\mathrm{b}}^2)^2}{(\frac{\boldsymbol{s}'(i)\boldsymbol{\eta}}{\beta}+\sigma_{\mathrm{b}}^2)(\frac{\boldsymbol{s}'(i)(\boldsymbol{\eta}+\boldsymbol{e})}{\beta}+\sigma_{\mathrm{b}}^2)} + \frac{1}{2}\log\left(\frac{\frac{\boldsymbol{s}'(i)\boldsymbol{\eta}}{\beta}+\sigma_{\mathrm{b}}^2}{\frac{\boldsymbol{s}'(i)(\boldsymbol{\eta}+\boldsymbol{e})}{\beta}+\sigma_{\mathrm{b}}^2}\right) - \frac{\beta\boldsymbol{s}'(i)\boldsymbol{e}}{2}\right]. \tag{C-6}$$

We further define

$$\begin{aligned}&\alpha(i) = \frac{1}{2}\frac{\frac{\boldsymbol{s}'(i)\boldsymbol{e}}{\beta}}{(\frac{\boldsymbol{s}'(i)\boldsymbol{\eta}}{\beta}+\sigma_{\mathrm{b}}^2)(\frac{\boldsymbol{s}'(i)(\boldsymbol{\eta}+\boldsymbol{e})}{\beta}+\sigma_{\mathrm{b}}^2)}, \gamma(i) = \frac{1}{2}\log\left(\frac{\frac{\boldsymbol{s}'(i)\boldsymbol{\eta}}{\beta}+\sigma_{\mathrm{d}}^2+\sigma_{\mathrm{t}}^2}{\frac{\boldsymbol{s}'(i)(\boldsymbol{\eta}+\boldsymbol{e})}{\beta}+\sigma_{\mathrm{b}}^2}\right) - \frac{\beta\boldsymbol{s}'(i)\boldsymbol{e}}{2}, \\ &x(i) = g(i)+\beta\sigma_{\mathrm{b}}^2, \quad \mathrm{Q} = \sum_{\mathrm{i=1}}^{\mathrm{KLM}}\alpha(\mathrm{i})\mathrm{x}(\mathrm{i})^2, \quad \tilde{\mathrm{Q}} = \sum_{\mathrm{i=1}}^{\mathrm{KLM}}\gamma(\mathrm{i}),\end{aligned} \tag{C-7}$$

and the LLR reduces to $\Lambda(\boldsymbol{g},\boldsymbol{\theta}) = \mathrm{Q}+\tilde{\mathrm{Q}}$. So the LLR test is

$$\begin{aligned}&\text{Decide } \mathcal{H}_0 : \Lambda(\boldsymbol{g},\boldsymbol{\theta}) < 0 \text{ (i.e., } \mathrm{Q} < -\tilde{\mathrm{Q}}), \\ &\text{Decide } \mathcal{H}_1 : \Lambda(\boldsymbol{g},\boldsymbol{\theta}) > 0 \text{ (i.e., } \mathrm{Q} > -\tilde{\mathrm{Q}}),\end{aligned} \tag{C-8}$$

and $P_{\min}(\boldsymbol{\eta},\boldsymbol{\eta}+\boldsymbol{e})$ (2.16) becomes

$$\begin{aligned}P_{\min}(\boldsymbol{\eta},\boldsymbol{\eta}+\boldsymbol{e}) &= \frac{1}{2}\big[\Pr(\mathrm{Q} < -\tilde{\mathrm{Q}}|\boldsymbol{\theta}=\boldsymbol{\eta}) + \Pr(\mathrm{Q} > -\tilde{\mathrm{Q}}|\boldsymbol{\theta}=\boldsymbol{\eta}+\boldsymbol{e})\big] \\ &= \frac{1}{2}\big[1-\Pr(\mathrm{Q} > \tilde{\mathrm{Q}}|\boldsymbol{\theta}=\boldsymbol{\eta}) + \Pr(\mathrm{Q} > -\tilde{\mathrm{Q}}|\boldsymbol{\theta}=\boldsymbol{\eta}+\boldsymbol{e})\big].\end{aligned} \tag{C-9}$$

From (C-1), we know $x(i) = g(i)+\beta\sigma_{\mathrm{b}}^2$ is also normally distributed with mean $\mu(i)$ and variance $\sigma^2(i)$ as

$$\mu(i) = \boldsymbol{s}(i)'\boldsymbol{\theta}+\beta\sigma_{\mathrm{b}}^2, \quad \sigma^2(i) = \frac{\boldsymbol{s}'(i)\boldsymbol{\theta}}{\beta}+\sigma_{\mathrm{b}}^2. \tag{C-10}$$

Therefore, Q is a non-negative definite quadratic form in non-central normal variables, which can be expressed as a weighted sum of chi-square variables [C1]:

$$\mathrm{Q} = \sum_{\mathrm{i}=1}^{\mathrm{KLM}} \alpha(\mathrm{i})\sigma^2(\mathrm{i})\chi_1^2\left(\frac{\mu^2(\mathrm{i})}{\sigma^2(\mathrm{i})}\right), \tag{C-11}$$

where $\chi_1^2(\mu^2(i)/\sigma^2(i))$ is a one degree of freedom noncentral chi-square variable, with non-central parameter $\mu^2(i)/\sigma^2(i)$. The mean μ_{Q} and standard deviation σ_{Q} of Q are

$$\mu_{\mathrm{Q}} = c_1, \quad \sigma_{\mathrm{Q}} = \sqrt{2c_2}, \quad c_k = \sum_{i=1}^{KLM}(\alpha(i)\sigma^2(i))^k + k\sum_{i=1}^{KLM}(\alpha(i)\sigma^2(i))^k\left(\frac{\mu^2(i)}{\sigma^2(i)}\right). \tag{C-12}$$

From [C1],[C2], the distribution of Q can be approximated by a non-central $\chi_l^2(\delta)$ distribution as follows:

$$\begin{aligned}\Pr(\mathrm{Q} > \mathrm{t}) \quad &= \Pr(\frac{\mathrm{Q}-\mu_{\mathrm{Q}}}{\sigma_{\mathrm{Q}}} > \frac{\mathrm{t}-\mu_{\mathrm{Q}}}{\sigma_{\mathrm{Q}}}) \approx \Pr(\frac{\chi_{\mathrm{l}}^2(\delta)-\mu_\chi}{\sigma_\chi} > \frac{\mathrm{t}-\mu_{\mathrm{Q}}}{\sigma_{\mathrm{Q}}}) \\ &= \Pr(\chi_{\mathrm{l}}^2(\delta) > \frac{\mathrm{t}-\mu_{\mathrm{Q}}}{\sigma_{\mathrm{Q}}}\sigma_\chi + \mu_\chi),\end{aligned} \tag{C-13}$$

where l denotes the degrees of freedom, and δ is the non-central parameter. $\mu_\chi = \mathrm{E}(\chi_{\mathrm{l}}^2(\delta)) = \mathrm{l}+\delta$, $\sigma_\chi = \sqrt{\mathrm{var}(\chi_{\mathrm{l}}^2(\delta))} = \sqrt{2}a$, and $a = \sqrt{l+2\delta}$. The parameters l and δ are determined so that the skewnesses of Q and $\chi_l^2(\delta)$ are equal and the difference between their kurtosis is minimized. From [C1], we have $l = c_2^3/c_3^2$ and $\delta = c_3/c_2^{3/2}a^3 - a^2$.

Combining (C-7)-(C-12), we obtain l, δ, σ_χ, and μ_χ in our problem, and $P_{\min}(\boldsymbol{\eta}, \boldsymbol{\eta}+\boldsymbol{e})$ of (C-9) is

$$\begin{aligned}P_{\min}(\boldsymbol{\eta}, \boldsymbol{\eta}+\boldsymbol{e}) = \frac{1}{2}\big[1 - \Pr(\chi_{\mathrm{l}}^2(\delta) > \frac{\tilde{\mathrm{Q}}-\mu_{\mathrm{Q}}}{\sigma_{\mathrm{Q}}}\sigma_\chi + \mu_\chi | \boldsymbol{\theta} = \boldsymbol{\eta}) \\ + \Pr(\chi_{\mathrm{l}}^2(\delta) > \frac{\tilde{\mathrm{Q}}-\mu_{\mathrm{Q}}}{\sigma_{\mathrm{Q}}}\sigma_\chi + \mu_\chi | \boldsymbol{\theta} = \boldsymbol{\eta}+\boldsymbol{e})\big].\end{aligned} \tag{C-14}$$

References

[C1] H. Liu, Y. Tang, and H. H. Zhang,"A new chi-square approximation to the distribution of non-negative definite quadratic forms in non-central normal variables," *Comput. Stat. Data. An.*, vol. 53, pp. 853856, Feb. 2009.

[C2] J. P. Imhof, "Computing the distribution of quadratic forms in normal variables," *Biometrika*, vol. 48, pp. 419426, Feb. 1961.

Appendix D

Snapshots of the Time-Resolved Progress of the Trapping Experiment on the Optimized and the Un-optimized devices

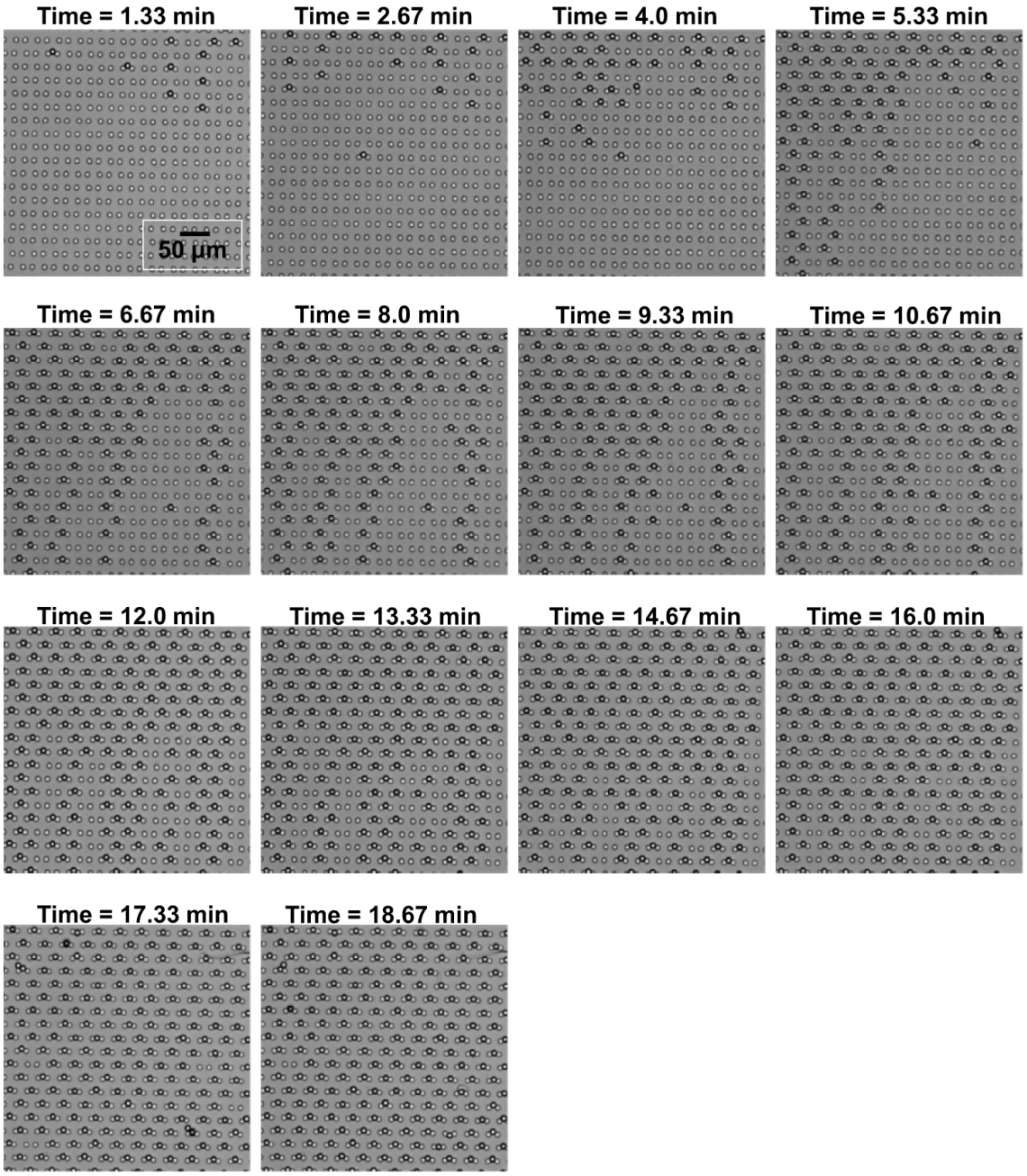

Figure D.1: Time-lapse high-speed camera snapshots of the microsphere-trapping experiment of the optimized device, from 1.33 min to 18.67 min.

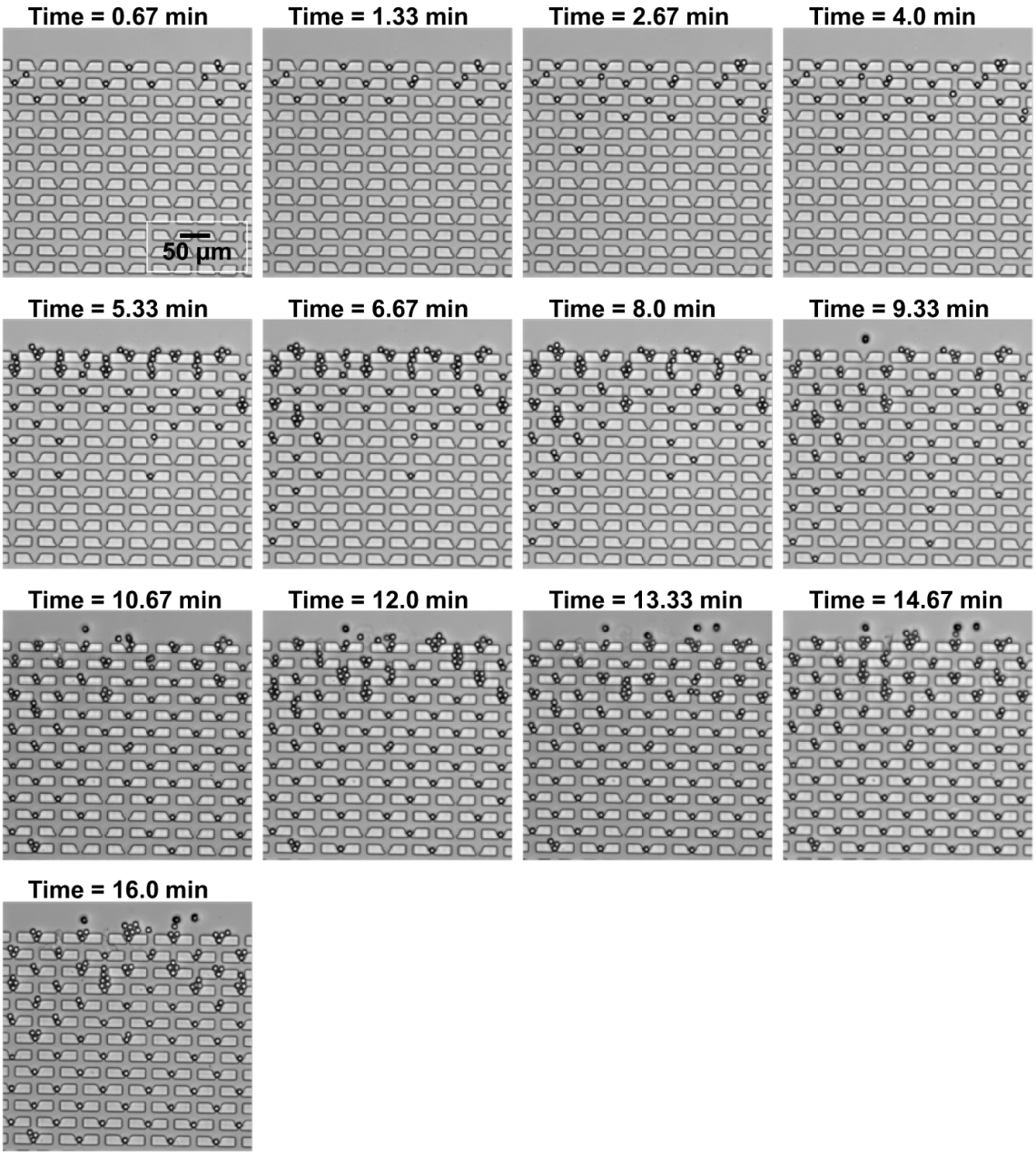

Figure D.2: Time-lapse high-speed camera snapshots of the microsphere-trapping experiment of the un-optimized device, from 0.67 min to 16.0 min.

Appendix E

Trapping Results for Ten Optimized and Ten Un-optimized Devices

Table E.1: Trapping results for the ten optimized and ten un-optimized microfluidic microsphere-trap arrays at the end of the experiments

Optimized Device (%) | Un-optimized Device (%)

Device No.	*single*	*multiple*	*empty*	*clogged*
1	99.052 | 55.844	0.474 | 44.156	0.474 | 0.000	0.000 | 6.494
2	99.052 | 59.740	0.948 | 40.260	0.000 | 0.000	0.000 | 6.494
3	99.052 | 57.143	0.474 | 42.857	0.474 | 0.000	0.000 | 5.195
4	98.580 | 61.039	0.474 | 38.961	0.948 | 0.000	0.000 | 9.091
5	99.530 | 58.442	0.000 | 41.558	0.474 | 0.000	0.000 | 7.792
6	99.530 | 61.039	0.000 | 38.961	0.474 | 0.000	0.000 | 7.792
7	100.00 | 59.740	0.000 | 40.260	0.000 | 0.000	0.000 | 6.494
8	99.530 | 57.143	0.000 | 42.857	0.474 | 1.299	0.000 | 7.792
9	99.530 | 61.039	0.474 | 38.961	0.000 | 0.000	0.000 | 5.195
10	99.052 | 54.545	0.948 | 45.455	0.000 | 1.299	0.000 | 7.792
Mean	99.291 | 58.571	0.379 | 41.429	0.332 | 0.260	0.000 | 6.927
STD	0.3828 | 2.2079	0.355 | 2.2078	0.304 | 0.520	0.000 | 1.190

Vita

Xiaoxiao Xu

Degrees

Ph.D., Electrical Engineering, Washington University in St. Louis, MO, USA, May 2014
M.S., Electrical Engineering, Washington University in St. Louis, MO, USA, Aug. 2011
B.S., Optical Science & Engineering, Fudan University, Shanghai, China, Jul. 2009

Professional Societies

Institute of Electrical and Electronics Engineers (IEEE)
IEEE Signal Processing Society and Communications Society
Society of Photo-Optical Instrumentation Engineers (SPIE)

Awards

National Science Foundation Student Travel Award at the *IEEE International Workshop on Genomic Signal Processing and Statistics (GENSIPS)*, Dec. 2012.

Publications

Journal Papers:

1. **X. Xu**, Z. Li, P. Sarder, N. Kotagiri, and A. Nehorai, "Simultaneous detection of multiple biological targets using optimized microfluidic microsphere-trap arrays," *Journal of Micro/Nanolithography, MEMS, and MOEMS*, vol. 13, 013017, Mar. 2014.

2. **X. Xu**, A. Wells, D. O'Brien, A. Nehorai, and J. D. Dougherty, "Cell-type specific expression analysis to identify putative cellular mechanisms for neurogenetic disorders," *The Journal of Neuroscience*, vol. 34, pp. 1420-1431, Jan. 2014.

3. **X. Xu**, G. Shi, and A. Nehorai, "Meta-regression of gene-environment interaction in genome-wide association studies," *IEEE Trans. on NanoBioscience*, vol. 12, pp. 354-362, Dec. 2013.

4. **X. Xu**, Z. Li, and A. Nehorai, "Finite element simulations of hydrodynamic trapping in microfluidic particle-trap array systems," *Biomicrofluidics*, vol. 7, pp. 014305, Sep. 2013.

5. **X. Xu**, A. Nehorai, and J. D. Dougherty, "Cell-type specific analysis of human transcriptome data to predict changes in cellular compositions," *Systems Biomedicine*, vol. 1, pp. 1-16, Jul. 2013.

6. **X. Xu**, P. Sarder, Z. Li, and A. Nehorai, "Optimization of microfluidic microsphere-trap arrays," *Biomicrofluidics*, vol. 7, pp. 014112, Feb. 2013 (**Selected among the 10 best "Editors' Pick" articles in 2012-13**).

7. **X. Xu**, P. Sarder, N. Kotagiri, S. Achilefu, and A. Nehorai, "Performance analysis and design of position-encoded microsphere arrays using the Ziv-Zakai bound," *IEEE Trans. on NanoBioscience*, vol. 12, pp. 29-40, Dec. 2012.

8. N. Kotagiri, Z. Li, **X. Xu**, S. Mondal, A. Nehorai, and S. Achilefu, "Antibody quantum dot conjugates developed via copper-free click chemistry for rapid analysis of biological samples using a microfluidic microsphere array system," submitted to *Bioconjugate Chemistry*.

9. A. Wells, N. Kopp, **X. Xu**, D. O'Brien, A. Nehorai, and J. D. Dougherty, "Tissue specific expression analysis of trait associated genes," submitted to *Nature Genetics*.

Conference Papers:

1. **X. Xu**, A. Nehorai, and J. D. Dougherty, "Cell-type enrichment analysis to identify cellular targets for autism spectrum disorder," *International Meeting for Autism Research (IMFAR)*, May 2013, San Sebastian, Spain.

2. **X. Xu**, Z. Li, N. Kotagiri, P. Sarder, S. Achilefu, and A. Nehorai, "Microfluidic microsphere-trap arrays for simultaneous detection of multiple targets," *Proc. SPIE 8615*, pp. 861552, Feb. 2013, San Francisco, USA.

3. **X. Xu**, P. Sarder, Z. Li, and A. Nehorai, "Optimization of microfluidic trap-based microsphere arrays," *Proc. SPIE 8615*, pp. 861533, Feb. 2013, San Francisco, USA.

4. **X. Xu**, A. Nehorai, and J. D. Dougherty, "Cell type specific analysis of human transcriptome data," *IEEE International Workshop on Genomic Signal Processing and Statistics (GENSIPS)*, pp. 99-100, Dec. 2012, Washington D.C., USA.

5. **X. Xu**, G. Shi, and A. Nehorai, "Genome-wide meta-regression of gene-environment interaction," *IEEE International Workshop on Genomic Signal Processing and Statistics (GENSIPS)*, pp. 62-65, Dec. 2012, Washington D.C., USA.

6. **X. Xu**, M. Kulkarni, A. Nehorai, and V. Gruev, "A correlation-based interpolation algorithm for division-of-focal-plane polarization sensors," *Proc. SPIE 8364*, pp. 83640L, Apr. 2012, Baltimore, USA.

7. **X. Xu**, P. Sarder, and A. Nehorai, "Statistical design of position-encoded microsphere arrays at low target concentrations," *Proc. 45th Asilomar Conf. Signals, Syst. Comput.*, pp. 1694-1698, Nov. 2011, Pacific Grove, USA.

May 2014